NATIONAL TECHNICAL UNIVERSITY OF ATHENS
SCHOOL OF APPLIED MATHEMATICAL AND PHYSICAL SCIENCES

CERN
EUROPEAN ORGANIZATION OF NUCLEAR RESEARCH

Optics optimization of tertiary particle beamlines and efficiency measurement of prototype scintillating fiber detectors

DIPLOMA THESIS

of

Chatzidaki Panagiota

CERN-THESIS-2018-373
02/10/2018

RESEARCH ADVISORS
Charitonidis Nikolaos,
Researcher, CERN
Karyotakis Yannis,
Researcher, LAPP

ACADEMIC ADVISOR
Tsipolitis Georgios,
Professor NTUA

Athens, NTUA, October 2018

NATIONAL TECHNICAL UNIVERSITY OF ATHENS
SCHOOL OF APPLIED MATHEMATICAL AND PHYSICAL SCIENCES

CERN
EUROPEAN ORGANIZATION OF NUCLEAR RESEARCH

Optics optimization of tertiary particle beamlines and efficiency measurement of prototype scintillating fiber detectors

DIPLOMA THESIS

of

Chatzidaki Panagiota

RESEARCH ADVISORS
Charitonidis Nikolaos,
Researcher, CERN
Karyotakis Yannis,
Researcher, LAPP

ACADEMIC ADVISOR
Tsipolitis Georgios,
Professor NTUA

Accepted by the committee

.....	.....	.....
Tsipolitis Georgios	Charitonidis Nikolaos	Kousouris Konstantinos
Professor, NTUA	Researcher, CERN	Assistant Professor, NTUA

Acknowledgments

This thesis was carried out during my work at CERN as a Research Assistant in the EN-EA Group, in the final year of my undergraduate studies. The completion of this thesis also signals my graduation from the National Technical University of Athens, and the beginning of a new chapter in my scientific career. There are a few people who have helped me, and to whom I'd like to express my gratitude.

Firstly, I would like to thank my supervisor at CERN, Dr. Nikolaos Charitonidis, who helped me take my first steps into the scientific world. With his knowledge and persistence, he showed me what kind of scientist I would like to become. With his continuous support and commitment during my stay at CERN, and his guidance in the writing of this thesis after I left, he made this a work I am really proud of.

Sincere gratitude goes to my second advisor, Dr. Yannis Karyotakis, who, despite my lack of experience, was very patient with me in the control room of T10. I thank him for trusting me with the data analysis, for having great expectations about my work, and treating me as his equal.

I would also like to thank my professor at the National Technical University of Athens, Dr. Yorgos Tsipolitis, who was the first to believe in me, and without him I would have never applied for the position at CERN.

I am truly grateful to my colleague at CERN, Dr. Marcel Rosenthal, for his enlightening insights and helpful remarks. I thank him for taking the time to provide me with the G4BeamLine simulations whenever I asked, without which my work could not stand by itself.

To my section leader, Dr. Lau Gatignon, and my Group Leader, Dr. Marcus Brugger, as well as the rest of my colleagues in the building 530 for helping me integrate in my first work environment so quickly, and for making me feel very welcome right away.

I would like to thank my friends, for the good times we've spent together during these five years at the University, and for their unfailing support and encouragement even during my stay at CERN.

Finally, I would like to thank my family, for encouraging me to pursue my dream, even if this meant us being apart.

Abstract

Two new beamlines, constituting extensions of the already existing H2 and H4 secondary beamlines of the North Area Complex of SPS at CERN, have been designed and installed in the framework of the CERN Neutrino Platform Project. These new extensions, designated H2-VLE and H4-VLE (**V**ery **L**ow **E**nergy), will select and transport low energy (0.4 - 12 GeV/c) particles to the experiments NP-02 and NP-04 respectively. The particles, either mixed hadrons or pure electrons, are generated by the interaction of the H2 and H4 beams with a target at the end of each secondary beamline.

In the first part of the present Diploma thesis, new optics configurations of the beamline magnetic elements have been developed. The new optics maximize the acceptance of the two lines and simultaneously minimize the spot size at the experiment, leading to the new baseline for these transport lines. In addition, the effects of possible spatial and rotational misalignments of the magnetic elements are studied and discussed.

In the second part, an efficiency/multiplicity measurement of two novel types of scintillating fiber detectors is described. The feasibility of these new detector modules, one providing fast trigger signals, while the other particle-by-particle transverse position measurements, is demonstrated for the first time with in-beam test in CERN's PS-T10 line. The performance of the two detectors is crucial for the beamline commissioning during fall 2018.

Contents

CHAPTER 1

Introduction

This chapter serves as a brief introduction to the North Area Facility of CERN, focusing in the beamlines of interest, namely H2 and H4. The need for extensions in order to facilitate the two novel detectors of the Neutrino Platform Project is explained.

1.1 The CERN injector complex

The accelerator complex of CERN, including its most important facilities, is shown in Fig. 1.1.

Protons, stripped off from hydrogen atoms and gradually accelerated through various rings, are injected to the 100m radius Proton Synchrotron (PS), increasing their energy to a maximum of 26 GeV/c. The PS injects protons to the Super Proton Synchrotron (SPS) and extracts them to the East Area Experiments and the IRRAD/CHARM Facilities. Through acceleration in the SPS, the proton beam reaches a maximum energy of 400 GeV/c and is mainly injected to LHC and secondarily extracted to other, fixed target experiments, including the North Area beamlines.

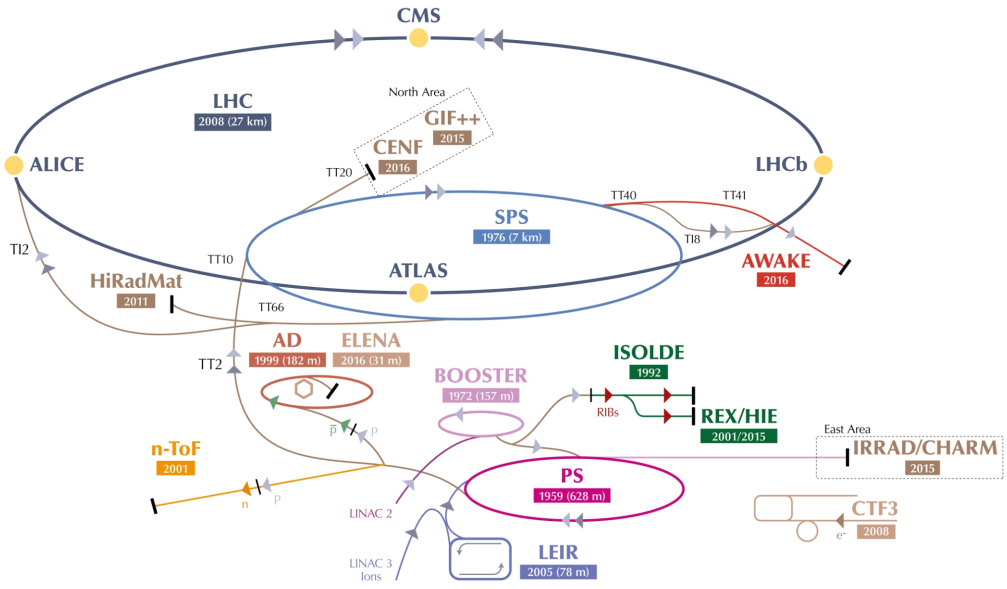

Figure 1.1: *The accelerator complex of CERN, including its most important facilities. [1]*

1.2 The North Area Facility of CERN/SPS

CERN's North Area Experimental Halls (EHN1, EHN2 and ECN3), shown schematically in Fig. 1.2, are facilities constructed during the 70's, hosting multi-purpose transfer lines designed to select and deliver a spectrum of secondary and tertiary particles of varying composition and momentum (10-400 GeV/c). The transported particles are produced by the interaction of the primary 400 GeV/c proton beam of SPS with three thin beryllium targets designated T2, T4 and T6. These primary targets are hosted in an underground cavern, designated "TCC2", ∼350 m upstream of the EHN1 experimental hall and ∼15 m underground. The beam is slowly extracted towards the North Area targets every ∼30 s.

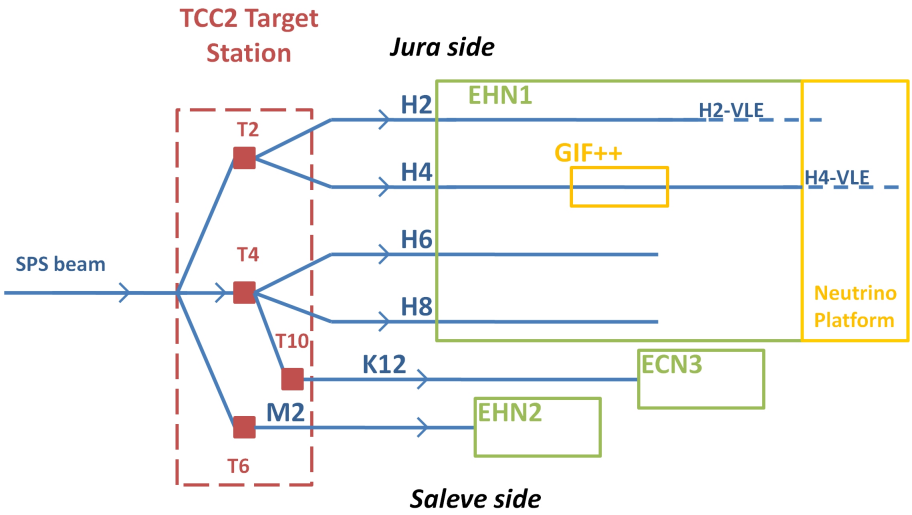

Figure 1.2: *North Area schematic layout. The GIF ++ (Gamma Irradiation Facility) is visible inside the EHN1 Hall. The Neutrino Platform Facility, constituting an extension of the EHN1 hall, will be discussed in 1.4.*

1.3 The EHN1 Experimental Hall

The EHN1 hall of CERN's North Area Facility, described in [2] and shown in Fig. 1.3, hosts four secondary beamlines. H2 and H4 (emerging from T2), of interest here, provide mixed hadron beams or electron beams of varying purity, with a maximum $\Delta p/p$ acceptance ∼2% and with an intensity normally in the range of $10^3 - 10^7$ particles per spill, the upper limit mainly set by radiation protection regulations in the hall. The overall beamline length is ∼600 m, while only the last ∼250 m are inside the EHN1 hall.

Numerous fixed target experiments placed one after the other in the experimental zones, as shown in Fig. 1.3, can calibrate their detectors, as well as test their performance in the presence of magnetic fields or to radiation exposure. Currently, the zones host test beams and quasi-permanent SPS experiments.

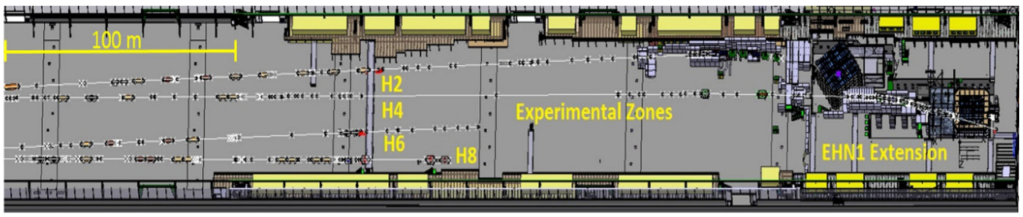

Figure 1.3: *EHN1 hall, from upstream (left) to downstream (right). The last ∼70 m, designated "EHN1 extension", are part of the Neutrino Platform Facility that will be discussed in 1.4 [10]*

1.4 The Neutrino Platform Project and the need for extensions

The Deep Underground Neutrino Experiment (DUNE) is a worldwide collaboration aiming to address fundamental questions currently open in the physics community, by the detailed investigation of the neutrino behaviors[3].

The neutrino behaviors are observed via a recently developed detector type, namely a Liquid Argon Time Projection Chamber (LArTPC), providing highly efficient calorimetry and tracking measurements. Interactions of transversing particles with the fluid volume will produce ionization electrons that drift under the influence of a high-voltage electric field towards the wire planes, and scintillation light, guided and detected by photo-detector modules. This technology was pioneered and successfully tested from 2006 to 2012 in the context of the ICARUS project [5], where the constructed detector, ICARUS T600, consisted of two identical 3.6x3.9x19.6 m^3 modules.

The next step in the neutrino investigation, significantly augmenting the detector's active volume, is "The Far Detector", a project conceptualized by DUNE. The Far Detector, estimated to commence data taking in 2026, is a 40 kiloton fiducial mass LArTPC, $\sim$1.5 km underground at SURF (Sanford Underground Research Facility) in Lead, South Dakota, that will be irradiated by the LBNF beamline, 1300 km away. The detector is composed of four 10kt LArTPC modules, allowing for the possibility to implement a different technology in each of them in the future.

To address the size extrapolation compared to the previous tested module, DUNE is developing two detector options that will be calibrated and tested at the CERN Neutrino Platform Facility (CENF). The "Single Phase" design, a newly constructed evolution of the successful ICARUS T600, uses a readout where the charge generation, drift and collection occur in the liquid argon. In the "Dual Phase" design, innovated by the WA105 experiment, the ionized electrons are extracted, amplified and detected in a layer of gaseous argon (GAr) above the liquid surface. Both detectors consist of a number of full-scale components of the Far Detector, and are 11x11x11 m^3 in size. A photograph of the NP-04 detector, already installed in the EHN1 hall, is shown in Fig. 1.4.

It is crucial that the test beam conditions be as similar to the ones expected in the DUNE Far Detector as possible. These requirements, described in the scientific proposals ([8], [9]), are summarized in Table 1.1.

The beam parameters proposed by the two experiments cannot be met by the al-

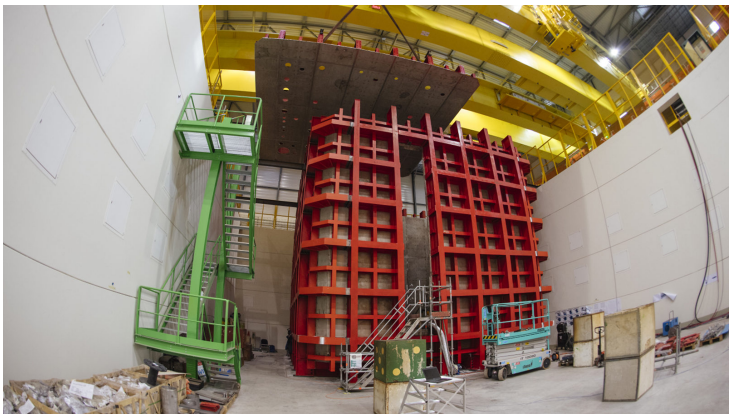

Figure 1.4: *NP-04 detector, installed in the Neutrino Platform Facility of EHN1. Photograph: Max Brice/CERN*

ready existing H2 and H4 beamlines. Specifically, taking into account the quite low desired momentum regime, the large beamline length of 600 m makes the transport of the already limited number of K and π generated at T2 impossible due to decays, as can be seen in Fig. 1.5 and 1.6.

Parameter	**"Double-Phase" (NP-02)**	**"Single-Phase" (NP-04)**
Particle type	$\pi^{+-}, \mu^{+-}, e^{+-}, K, p$	
Momentum	< 12 GeV/c	< 7 GeV/c
$\Delta p/p$ RMS	$< 5\%$	
Beam size RMS	$\sim$10 cm at the entrance of the cryostats	
Maximum rate	100 Hz	

Table 1.1: *Required beam parameters of NP-02 and NP-04. [10]*

At the same time, at the relatively low currents required to bend particles below $\sim$10 GeV/c, the power supply instabilities ($\sigma_I \simeq 0.3$ A) become significant. For example, by applying the current required to bend particles with 10 GeV/c nominal momentum, and by assuming that each bending magnet is being applied with a current 0.3 A above the reference value, the nominal momentum uncertainty is $\sim$15%.

To deliver kaons and pions in this low energy regime, significantly shorter transfer lines needed to be designed. Therefore, to overcome this difficulty, the two beamlines have been extended in tertiary mode, and the particles delivered at the prototypes will be produced by the interaction of the H2 and H4 beams with a secondary target at the end of each beamline.

In order to install the beamline extensions and to host the two 11x11x11 m^3 cryostats, the EHN1 hall has been extended downstream $\sim$70 m (as shown in Fig. 1.3). The layout and optics of the two VLE (**V**ery **L**ow **E**nergy) beamlines, that began being designed in 2014 and are expected to begin commissioning at the Fall of 2018, will be described in

depth in Chapter 4.

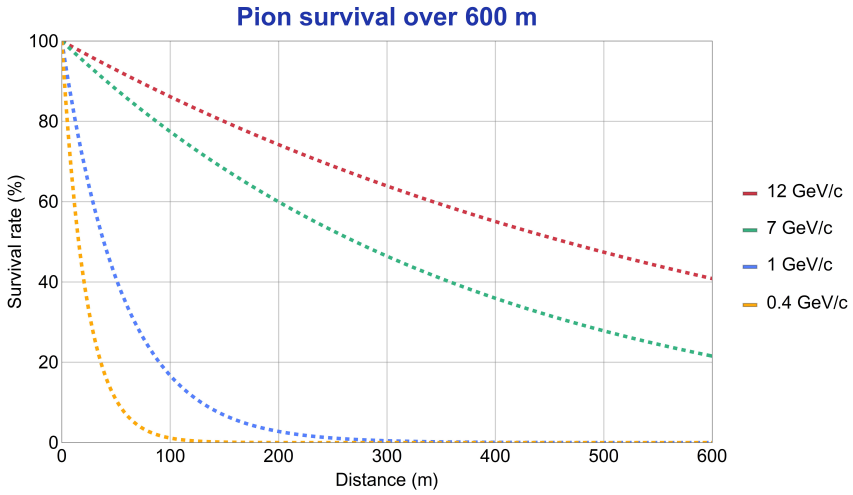

Figure 1.5: *Survival rate of low momenta pions with respect to the travel distance, a 600 m distance corresponding to the H2 and H4 beamline length.*

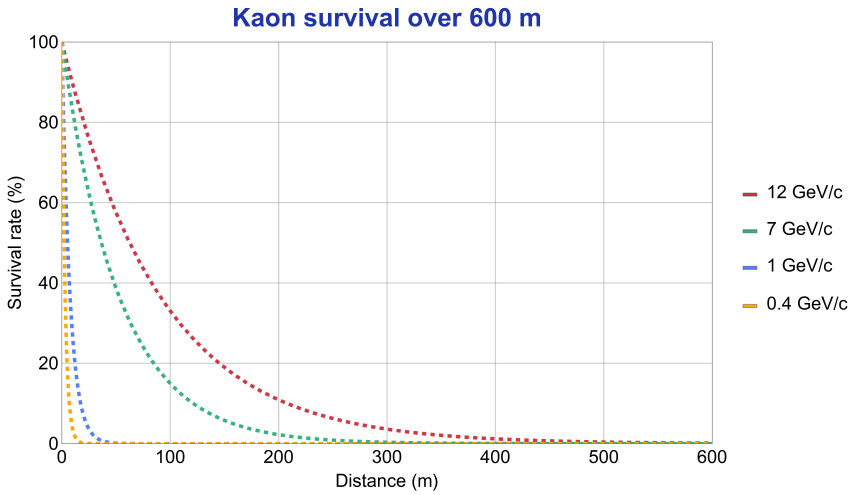

Figure 1.6: *Survival rate of low momenta kaons with respect to the travel distance, a 600 m distance corresponding to the H2 and H4 beamline length.*

Part I

Optics optimization and misalignment studies of H2-VLE and H4-VLE

CHAPTER 2

Transverse Beam Dynamics

In the presence of electromagnetic fields, a particle of one unit charge will undergo the Lorentz force given by:

$$\vec{F}_L = e \cdot (\vec{E} + \vec{u} \times \vec{B}) \tag{2.1}$$

The motion of charged particles in a transfer line is determined by the effect of static magnetic fields, that provide the beam guidance and focus. The use of magnetic instead of electric fields is necessitated by the technical difficulty to establish the static electric field magnitudes needed to steer relativistic particles. Particularly, to generate the force provided by a magnetic field of 1 T, an electric field of 300 MV/m would be required, which is extremely challenging to generate due to field breakdown and electrical discharges. Assuming that the beam particles interact only with magnetic fields generated by the beamline elements and not by their neighboring particles, the magnetic field $\vec{B}$ denotes the external magnetic field, applied by dipole and quadrupole magnets in the case of the present diploma thesis.

To describe the motion of charged particles, we use the Frenet-Serret local coordinate system, shown in Fig 2.1 which follows the reference orbit.

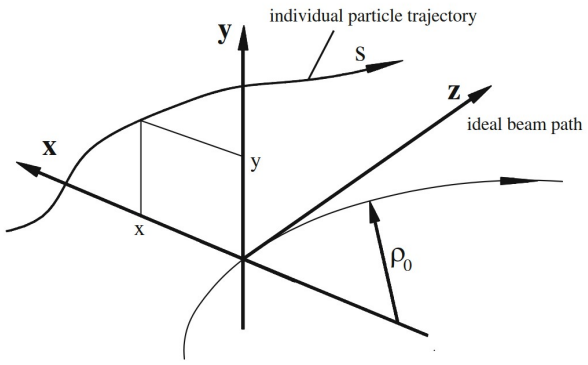

Figure 2.1: *Frenet-Serret local reference system, following the reference orbit. [13]*

The "reference orbit" (or "reference trajectory") is the path followed by a charged particle emitted from the production point with the desired, nominal set of initial parameters. The reference trajectory is determined by bending magnets only, while drift spaces and quadrupoles (and other higher order magnets) will not affect it, but serve to

keep all other particles in the vicinity of it.

Usually z is used in describing the ideal orbit, and s the arbitrary one (see Fig. 2.1), while the reference orbit's curvature is denoted as ρ_0. The axis $\hat{z}$ always remains parallel to the reference particle velocity, while $\hat{x}$ is always perpendicular to it. To form a right-handed orthogonal reference system, $\hat{y}$ is binormal to these two.

2.1 Hill's Equation

The differential equation of motion of a charged particle under the influence of a magnetic field can be derived by Eq. (2.1) along with Newton's 2^{nd} law of motion:

$$m\frac{d^2\vec{r}}{dt^2} = e\vec{u} \times \vec{B} \tag{2.2}$$

which in general cannot be solved analytically for an arbitrary magnetic field.

Under certain assumptions, however, the above formula can be simplified significantly, and we can arrive to a much simpler equation, namely "Hill's Equation", the derivation of which can be found in Appendix A. The applicability of Hill's Equation rests on the following approximations: first of all, it is assumed that the velocity of each particle is constant along the beamline, which is the case for static magnetic fields. Additionally, particles with small transverse velocity components, compared to the total velocity ($u_x, u_y << u_z \approx u$) are considered, an assumption realistic for relativistic beams. To solve the equation of motion, we must neglect any coupling terms between the two planes, and limit ourselves to terms linearly dependent on x (or y). Therefore in the Taylor expansion of the magnetic field,

$$B_y(x) \approx B_{0y} + x \cdot \left.\frac{\partial B_y(x)}{\partial x}\right|_{x=0} \tag{2.3}$$

As will be discussed in sections 2.4 and 2.5, the constant term describes the field generated by an ideal dipole magnet, while the linearly dependent term that of an ideal quadrupole magnet.

Under the aforementioned assumptions, the equation of motion can be solved, and we can derive Hill's Equation:

$$u''(s) + K(s)\,u(s) = 0 \tag{2.4}$$

where

-u stands either for x or y,

-the derivative is with respect to the orbit coordinate s ($u'' \equiv d^2u/ds^2$), and

- $K = k + 1/\rho_0^2$, where k is the normalized quadrupole coefficient, defined in 2.5.

In the case of a perfect dipole, the quadratic term k is zero, while for an ideal quadrupole $\rho_0 = \infty$, therefore $1/\rho_0^2 = 0$.

2.2 Matrix formalism

At any position z along the beamline, an arbitrary particle can generally be represented by a six-dimensional vector Ψ,

$$\Psi = \begin{bmatrix} x \\ x' \\ y \\ y' \\ l \\ \delta p/p_0 \end{bmatrix} \tag{2.5}$$

where

-x and y are the horizontal and vertical displacements of the particle with respect to the reference trajectory,

-$x' \equiv dx/ds$ and $y' \equiv dy/ds$ (which correspond in first order to the angle that its velocity forms with the $y-s$ and $x-s$ planes),

-l is the path length difference, and

-$\delta p/p_0$ is the fractional momentum offset of the arbitrary particle with respect to the design momentum.

In first order, one can represent the effect of drift spaces, dipoles and quadrupoles in the position and angle of a particle as matrices acting upon the particle vector described by Eq. (2.5) [14]. The assumption of independent motion in the two transverse planes allows to represent the six-dimensional vector Ψ as two separate, three dimensional vectors in x and y:

$$X = \begin{bmatrix} x \\ x' \\ \delta p/p_0 \end{bmatrix} \qquad Y = \begin{bmatrix} y \\ y' \\ \delta p/p_0 \end{bmatrix} \tag{2.6}$$

At a certain position z along the reference trajectory, the total effect of the beam elements can be represented, in the case of static magnetic fields, by a 3x3 matrix for each plane (which is the product of the individual matrices up to this position),

$$R_x = \begin{bmatrix} R_{11} & R_{12} & R_{16} \\ R_{21} & R_{22} & R_{26} \\ R_{61} & R_{62} & R_{66} \end{bmatrix} \qquad R_y = \begin{bmatrix} R_{33} & R_{34} & R_{36} \\ R_{43} & R_{44} & R_{46} \\ R_{63} & R_{64} & R_{66} \end{bmatrix} \tag{2.7}$$

This matrix formulation reflects the fact that, to first order, the coordinates x and x' at any position, can be expressed as the linear combination of the initial coordinates x_0, x_0' and $\delta p/p_0$ at the production point. Since the total momentum is assumed to be constant throughout the transfer line, the terms R_{61} and R_{62} (and the corresponding ones in the vertical plane) will always be zero, while R_{66} should always equal unity.

More specifically, the R_{11} term in the horizontal plane (and R_{33} in the vertical plane), or "magnification term", depicts the expected in first order displacement with respect to the reference trajectory (in mm) of a particle having a horizontal (or vertical) displacement of 1 mm at the target. The R_{12} term in the horizontal plane (R_{34} in the vertical

plane) indicates the displacement of a particle produced at the target with an initial angle of 1 mrad with respect to the horizontal (or vertical) plane. The R_{16} term in the horizontal plane (R_{36} in the vertical plane), or "dispersive term" depicts a particle with a 1% momentum offset, but zero initial spatial and angular displacements.

It can be shown that, as a consequence of Liouville's Theorem, the determinant of the 2x2 matrix for each plane must remain constant and equal to unity throughout the beamline.

We next examine the effect of drifts, bending magnets and quadrupole magnets upon these particle vectors. It is reminded that the matrix formalism is accurate to first order, therefore, to include perturbative higher order terms appearing in the derivation of Hill's Equation in Appendix A, a different formulation has to be used, that will be described in 2.7. Nevertheless, the first order approach remains a good approximation in most of the cases, and is intuitively clear.

2.3 Drift space

A drift space is a field-free region, where the particle transverses without any force being exerted upon it. Integrating Hill's Equation for a drift space of length L in the horizontal plane yields:

$$\begin{aligned} x &= x_0 + x_0' \cdot L \\ x' &= x_0' \end{aligned} \tag{2.8}$$

which can be expressed by the drift matrix, identical for both planes,

$$D = \begin{bmatrix} 1 & L & 0 \\ 0 & 1 & 0 \\ 0 & 0 & 1 \end{bmatrix} \tag{2.9}$$

2.4 Dipole magnet

An ideal dipole magnet has an homogeneous and constant field, here assumed along the y-axis, $\vec{B} = B\hat{y}$. From the equilibrium of the centrifugal force and the Lorentz force, $euB = mu^2/\rho$, one obtains:

$$B\rho = p/e \tag{2.10}$$

where $p = mu$ is the relativistic momentum, and the product $B\rho$ is termed the "magnetic rigidity". A particle inside a magnet will follow a circular trajectory on the $x - s$ plane (perpendicular to the magnetic field), with the total deflection angle given by:

$$\theta = \frac{l}{\rho} \tag{2.11}$$

where $l = \int dz$ is the arc (or effective) length.

Substituting Eq. (2.11) to (2.10) yields the formula

$$\theta[\text{rad}] \approx \frac{0.3B[\text{T}] \cdot l[\text{m}]}{p[\text{ GeV/c}]} \tag{2.12}$$

Setting the quadratic term equal to zero in Eq. (2.4), one obtains an equation identical to that of an harmonic oscillator, illustrating focusing properties:

$$x'' + \kappa_0^2 x = 0 \tag{2.13}$$

The most "natural" bending magnet is the sector magnet, where the reference particle enters and exits the magnet perpendicular to its pole faces, and by integrating Eq. (2.13) over the arc length l, its 2x2 matrix representation is derived, which demonstrates purely geometrical focusing properties in the bending plane.

To arrive to the 3x3 matrix representation, we need to include the dispersive perturbative terms in the right-hand side of (A.6) of Appendix A, and specifically the equation of motion takes the form, in first order:

$$x'' + \kappa_{0x}^2 x = \kappa_{0x}\delta \tag{2.14}$$

the solution of which is thoroughly discussed in several accelerator physics textbooks (see, for example, [13]). By pole-face rotating the sector magnet, we obtain the matrix of a rectangular magnet, which is easier to construct and laminate, and therefore widely used at CERN. The matrix of a rectangular magnet in the bending plane is:

$$M_x = \begin{bmatrix} 1 & \rho_0 sin\theta & \rho_0(1-cos\theta) \\ 0 & 1 & 2tan(\theta/2) \\ 0 & 0 & 1 \end{bmatrix} \tag{2.15}$$

where ρ_0 and θ are the bending radius and angle of the nominal trajectory respectively. The geometrical focusing effect has now disappeared ($R_{21} = 0$), and a rectangular magnet behaves like a drift in the bending plane, as long as focusing properties are considered. A momentum-dependence is introduced by the non-zero R_{16} and R_{26} terms. In Fig 2.2 the path followed by the reference particle, as well as that of an arbitrary particle entering parallel to the reference particle are shown.

A bending magnet of a given magnetic field B will deflect particles based on their momentum according to Eq. (2.12), and as indicated by the non-zero R_{26} term of Eq. (2.15). Therefore, particles of lower momenta will be deflected more than particles of higher momenta. The displacement with respect to the reference trajectory of a particle having a momentum offset δ, but zero initial spatial and angular displacements can be calculated in first order via Eq. (2.7) as

$$\Delta x = R_{16} \cdot \delta \tag{2.16}$$

By placing a slit, or "collimator", after the bending magnet, symmetrically in between the reference trajectory, only particles having momenta adjacent to the desired will pass. To select particles of maximum momentum offset δ, the R_{16} term (defined by the magnet strength and the distance of the dipole from the collimator) and the jaw opening Δx need to be balanced in order to satisfy Eq. (2.16).

This dependence of the particle position on the momentum introduced by the bending magnet, or "dispersion", is in most cases undesirable for the experiments since it can cause an enlargement of the beam size, especially if the beam particles have significant deviations from the design momentum. It is therefore customary to "recombine" the dispersion or, mathematically speaking, demand that the R_{16} and R_{26} terms are zero at the position of the experiment.

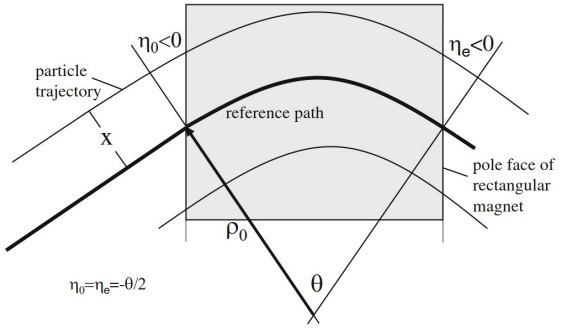

Figure 2.2: *Path followed inside a rectangular magnet [13]*

The hard edge model described above is an idealization, since in real dipole magnets the magnetic field extends outside the magnetic core, and in particular there is a gradual transition of the field from its maximum value at the center to zero, referred to as "fringe field". In a rectangular magnet, this effect introduces a small focusing in the non-bending plane. The effect of the fringe fields can be treated in first order using various models to mathematically describe this transition (see, for example the TRANSPORT manual [16]). Particle tracking codes such as PTC (presented in 3.3), which will be extensively used in the present thesis, treat the fringe fields in higher order.

2.5 Quadrupole magnet

To keep the particles in the vicinity of the reference orbit, quadrupole magnets are installed along the beamline. A quadrupole magnet generates a magnetic field that increases linearly with distance in both x and y:

$$B_x(y) = \frac{\partial B_x}{\partial y} y, \qquad B_y(x) = \frac{\partial B_y}{\partial x} x \tag{2.17}$$

Due to the absence of an electric field, from Maxwell's Equation it can be shown that the field gradients in the two planes are equal, $\frac{\partial B_x}{\partial y} = \frac{\partial B_y}{\partial x} \equiv g$. From Eq. (2.1) this mag-

netic field results in a force that varies linearly with the distance from the quadrupole center in both planes:

$$F_x = -eugx, \qquad F_y = eugy \tag{2.18}$$

One can see that, for $g > 0$ (and a positive particle charge), the force is restoring in x, and therefore the quadrupole will have a focusing effect in the horizontal plane, while in the vertical plane the particles will be defocused. Even though a single quadrupole will necessarily defocus the particles in one plane, a combination of quadrupoles can become a system that is focusing in both planes simultaneously. The magnetic field of a quadrupole magnet is illustrated in Fig. 2.3.

It is common in transverse particle dynamics to use the "normalized quadrupole coefficient" k, instead of the field gradient g:

$$k = \frac{1}{p/e}g, \qquad [k] = m^{-2} \tag{2.19}$$

For the horizontal (focusing) plane and the vertical (defocusing) plane, from Eq. (2.2), one obtains:

$$\frac{d^2x}{ds^2} = -kx, \quad \frac{d^2y}{ds^2} = +ky, \tag{2.20}$$

By integrating over the quadrupole length l, the solutions can be expressed via the focusing (f) and defocusing (d) quadrupole matrices:

$$Q_f = \begin{bmatrix} cos(\sqrt{k}l) & sin(\sqrt{k}l)/\sqrt{k} & 0 \\ -\sqrt{k} \cdot sin(\sqrt{k}l) & cos(\sqrt{k}l) & 0 \\ 0 & 0 & 1 \end{bmatrix} \tag{2.21}$$

$$Q_d = \begin{bmatrix} cosh(\sqrt{k}l) & sinh(\sqrt{k}l)/\sqrt{k} & 0 \\ +\sqrt{k} \cdot sinh(\sqrt{k}l) & cosh(\sqrt{k}l) & 0 \\ 0 & 0 & 1 \end{bmatrix} \tag{2.22}$$

In the case where $\sqrt{k} \cdot l << 1$, the above matrices reduce to

$$Q = \begin{bmatrix} 1 & 0 & 0 \\ \pm 1/f & 1 & 0 \\ 0 & 0 & 1 \end{bmatrix} \tag{2.23}$$

which is identical to a focusing (-) or a defocusing (+) optical lens of focal length $f = 1/kl$.

It should be mentioned that the matrices described by Eq. (2.21) and (2.22) do not account for possible momentum offsets. The quadrupole coefficient in these equations is exact only for the design momentum, while in general $k = k(p)$. This momentum dependence of the focusing strength gives rise to chromatic aberrations that describe imaging errors due to momentum deviations and, since they are second order effects, are ignored in the 1^{st} order matrix formalism developed.

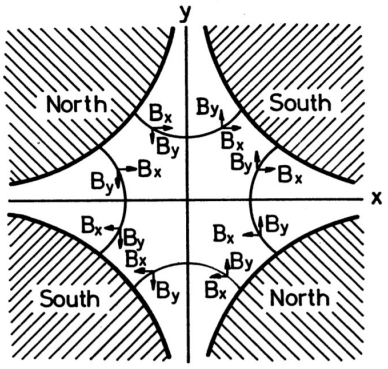

Figure 2.3: *Magnetic field lines of an ideal quadrupole in the plane transverse to the beam direction. [15]*

2.6 Twiss Parameters

In accelerator physics, it is often more convenient to represent the beam as a whole, rather than tracing each one of its particles. The particles comprising the beam define a region in the $x - x'$ and $y - y'$ phase spaces, the area of which is referred to as horizontal and vertical "beam emittance" respectively. While the phase space will transform in shape and orientation along the transfer line, according to Liouville's Theorem, the area of this phase space must remain constant. In the case of circular machines, where Hill's Equation will be solved with periodic conditions, according to Floquet's Theorem the solution can take the form:

$$x(s) = \sqrt{\epsilon}\sqrt{\beta(s)}cos(\psi(s) + \phi) \tag{2.24}$$

It can be proven (see [20]) that in this case, the phase space is an ellipse of area $A = \pi\epsilon$ in both planes described by:

$$\epsilon = \gamma(s)x^2(s) + 2\alpha(s)x(s)x'(s) + \beta(s)x'^2(s) \tag{2.25}$$

where

$$\alpha(s) = -\frac{1}{2}\frac{d\beta(s)}{ds}, \qquad \gamma(s) = \frac{1 + \alpha^2(s)}{\beta(s)} \tag{2.26}$$

The parameters α, β and γ are functions of the independent variable s, and are called the "Twiss Parameters", defining the shape and orientation of the phase space ellipse at every position of the beamline, as can be seen in Fig. 2.4. Instead of using a matrix formulation describing the transformation of the individual particle coordinates throughout the line as analyzed in Section 2.2, similar matrices can be derived that transform the Twiss Parameters through various elements.

This ellipse contains one sigma of all the beam particles of the phase space. In a specific position s, the maximum deviation of a particle of the ellipse in the horizontal plane, or the one sigma, as described by (2.24), is $\sigma_x(s) = \sqrt{\epsilon_x}\sqrt{\beta(s)}$.

While the Twiss formalism is quite popular in optimizing and describing the optics

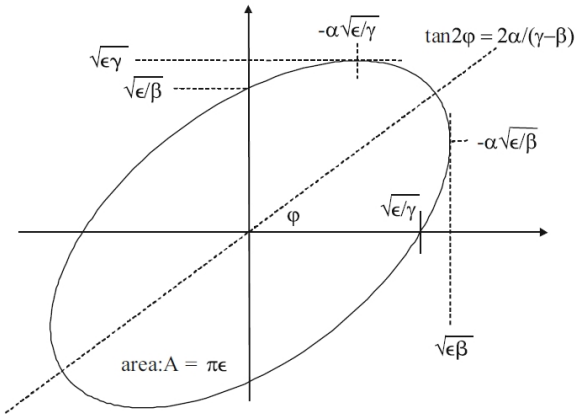

Figure 2.4: *Phase space ellipse described by Eq. (2.25) [13].*

of beamlines, in the optimization process followed in the present thesis, the formalism described in Section 2.2 will be used. The reason for this choice is the lack of periodicity in transfer lines, and therefore the assumption of a constant phase space ellipse breaks down. By collimating the beam, 'cuts' are created to the edges of the phase space ellipse, which no longer retains its constant area. The system is not closed, and Liouville's Theorem for the emittance preservation is no longer valid.

2.7 Particle motion using the Hamiltonian formalism

Newton's equation of motion is not reference system-invariant. We can express the equations of motion in an equivalent but reference system-invariant way using the Hamiltonian formalism, which is a derived via the Lagrangian and is a function of the spatial coordinates and the momenta, (q_i, p_i):

$$H(q_i, p_i) = \sum \dot{q}_i p_i - L \tag{2.27}$$

where the dot denotes differentiation with respect to the time t. Equivalently to the Euler-Lagrange equations, the Hamiltonian equations are

$$\frac{\partial H}{\partial q_i} = -\dot{p}_i, \qquad \frac{\partial H}{\partial p_i} = +\dot{q}_i \tag{2.28}$$

which are a set of $2N$, first order differential equations. Further details about the Lagrangian and the Hamiltonian can be found in classical mechanics textbooks, such as [17].

It is more useful in beam dynamics to substitute the independent variable t with the independent variable s. Then the set of equations (2.28) can be written as

$$p_i' = -\frac{\partial \mathcal{H}}{\partial q_i}, \qquad q_i' = \frac{\partial \mathcal{H}}{\partial p_i} \tag{2.29}$$

where $\mathcal{H}$ denotes the s-dependent Hamiltonian, and the prime denotes differentiation with respect to s.

Instead of using a Cartesian reference system, it is more convenient to use the Frenet-Serret reference system as defined in the beginning of Chapter 2. For a relativistic particle in the presence of electromagnetic fields, the s-dependent Hamiltonian can be derived [18] by (2.27):

$$\mathcal{H} = p_\sigma - (1+\kappa_x x)\left(\sqrt{(1+\delta)^2 - (p_x-\alpha_x)^2 - (p_y-\alpha_y)^2} + \alpha_s\right) \tag{2.30}$$

where

-$p_\sigma = \frac{1}{\beta_0}\frac{E-E_0}{p_0 c}$ is a measure of the energy deviation of the arbitrary particle with respect to the reference one with momentum p_0,

-δ is its momentum deviation,

-κ_x is the inverse bending radius, and

- $\alpha_i = \frac{q}{p_0}A_i$ are the normalized elements of the magnetic vector potential.

Eq. (2.30) is referred to as the "Exact Hamiltonian". It is completely general, if one neglects synchrotron radiation and collective effects.

Very commonly, the transverse momenta are very small compared to the total momentum. In these cases, one may expand the square root in (2.30) as

$$(1+\delta)\sqrt{1-\frac{(p_x-\alpha_x)^2+(p_y-\alpha_y)^2}{(1+\delta^2)}} \approx (1+\delta)\left(1-\frac{1}{2}\frac{(p_x-\alpha_x)^2+(p_y-\alpha_y)^2}{(1+\delta^2)}\right)$$

which simplifies significantly the derivation of the equations of motion. By substituting the above expression to (2.30) yields the "Expanded Hamiltonian".

2.7.1 Canonical transformation

A canonical transformation (or a "map") is a transformation from a set of canonical coordinates (q_i, p_i) to a new set of coordinates (Q_i, P_i). This transformation also involves a transformation of the old Hamiltonian H, to the new one, K, and the new set of canonical coordinates and Hamiltonian must again satisfy Eq. (2.28).

By defining the column matrix of canonical variables $\vec{x}$,

$$\vec{x} = \begin{bmatrix} q_1 \\ p_1 \\ q_2 \\ p_2 \\ \vdots \\ q_N \\ p_N \end{bmatrix} \tag{2.31}$$

it is possible to write the Hamiltonian equations of motion in a single matrix equa-

tion, using the "rearranging matrix" $\vec{S}$,

$$\vec{S} = \begin{bmatrix} \vec{s} & \vec{0} & \cdots & \vec{0} \\ \vec{0} & \vec{s} & \cdots & \vec{0} \\ \cdots & \cdots & \cdots & \cdots \\ \vec{0} & \cdots & \cdots & \vec{s} \end{bmatrix} \tag{2.32}$$

where $\vec{s}$ is an antisymmetric 2x2 matrix,

$$\vec{s} = \begin{bmatrix} 0 & 1 \\ -1 & 0 \end{bmatrix} \tag{2.33}$$

and, with tis notation, the Hamiltonian equations can be expressed in the compact form

$$\vec{x'} = \vec{S}\frac{\partial \mathcal{H}}{\partial \vec{x}}, \tag{2.34}$$

where

$$\left(\frac{\partial \mathcal{H}}{\partial \vec{x}}\right)_i = \frac{\partial \mathcal{H}}{\partial x_i}$$

A transformation is a canonical one, if and only if it satisfies the "symplectic condition", which can be stated as

$$\vec{M}^T \vec{S} \vec{M} = \vec{S} \tag{2.35}$$

where $\vec{M}$ is the Jacobian matrix (the matrix of derivatives of the new coordinates with respect to the old ones).

Usually, to apply a canonical transformation, one uses one of the four "generating functions" that can be found for example in [18]. These canonical transformations form a group.

2.7.2 Symplectic integration

It is often impossible (or extremely time-consuming) to solve the equations of motion in an accelerator analytically, and therefore we are most of the time forced to use numerical integration. A numerical integration generally introduces errors in each step, but, by using symplectic integrations, we can eliminate a class of errors, namely the"asymplectic errors". Symplectic integrators (integration methods) are integrators where an integration step can be thought as a mapping from an initial coordinate set to a new one. This type of integration is used in the PTC ("Polymorphic Tracking Code") that we will extensively use in our analysis.

For further reading on symplectic integration, one can consult [18].

CHAPTER 3

Optics and particle tracking codes

A transfer line is initially designed in first order. Once the basic layout has been determined, the various design requirements are translated in the matrix formalism as constraints of the R-matrix elements at specific positions, and, by varying the degrees of freedom available, a matching is attempted. Since there are many degrees of freedom (and simultaneously many constraints) it is practically impossible to perform the optimization analytically (meaning that, one computes the R-matrix at each position, leaving the available degrees of freedom as parameters, and then solves, analytically, the constraint equations). This is why optics codes are used, which attempt, in a numerical way, to match the given constraints.

In cases where the transverse particle coordinates are quite large, or when significant momentum offsets are introduced, the first order approach does not suffice. Higher order particle tracking codes are then necessary.

This chapter describes the basic characteristics and differences of the various optics and tracking tools used, demonstrating the insufficiency of the first order approach in the present optics study.

3.1 TRANSPORT and TURTLE

TRANSPORT is a 1^{st} (and 2^{nd}) order optics program that computes, through matrix multiplications, the matrix elements along a transfer line. It has been available in various releases since 1963 and is a well-benchmarked code, used to design most of CERN's beamlines. After defining the beamline sequence in a simple input file, the user can specify which parameters may vary through the matching process and the constraints that should be imposed on the matrix elements at certain positions. TRANSPORT then attempts, via a series of iterations, to minimize the chi-square by correcting the varied parameters, using a matrix inversion procedure.

With a few changes in the TRANSPORT input file, the tracking code TURTLE can be used. TURTLE is not a pure integrator, in the sense that, rather than integrating the equations of motion for a single particle, it calculates the (up to 3^{rd} order) matrix elements throughout the line, and then applies the transformations to each particle. A 'default' distribution is generated, the maximum spatial, angular and momentum spread of which are defined by the user. By setting the aperture of the magnetic elements, one can observe, using histograms, the particle distribution along the beamline and track

the losses.

The major drawback of TURTLE is that it is not possible to track a user-defined particle distribution. This is quite important when a realistic tracking is attempted. As will be discussed in Chapter 5, the particle distributions generated at the secondary targets of the VLE beamlines are very different from the ones in TURTLE by having a correlation between the various coordinates.

Moreover, it is not possible to observe throughout the line the coordinates of a single particle, but only the mean value and spread of the entire distribution. The former, while it may seem redundant, is vital when a deep understanding of the optics is attempted.

3.2 MAD-X

MAD-X [19] is a very well documented, and with an increasing user community modern tool for beam optics design, and is a successor of MAD-8, firstly released in 2002. It is the tool used for the design of the LHC.

After defining the beamline sequence in MAD-X similarly to TRANSPORT, the user can perform several tasks via various modules. These modules may communicate with each other, and transfer values from the one to the other.

The most basic module of MAD-X is the "TWISS" module, which can calculate the first order matrices in the same manner as TRANSPORT. "TWISS" may calculate and print for a single particle, given its initial coordinates, the coordinates along the beamline. These calculations, however, do not result from first order multiplications, but are higher order.

MAD-X's "MATCH" module can be used to optimize the beamline characteristics. The MATCH module internally invokes the "TWISS" module, and the latter transmits attributes to the former during the matching procedure. Since it's a contemporary code, it has incorporated a number of matching algorithms. For the optimization process of the present thesis, where the degrees of freedom were very commonly less than the number of constraints imposed, the Jacobian method was used. An additional feature of the "MATCH" module of MAD-X, compared to TRANSPORT, is that the user can specify lower and upper limits for the varied parameters. This has been particularly useful in the optimization process, since the power supplies imposed strict limitations on the quadrupole currents.

The "EALIGN" module of MAD-X is the misalignment module. It allows to misplace each magnet around its ideal position, with a total of six degrees of freedom (spatially and angularly). These misalignments are then saved in a file, and invoked by the various modules (for example, the "TWISS" module, or the "PTC" module discussed in 3.3)

MAD-X has a symplectic tracking module, "TRACK". After having converted the elements into thin (zero length) slices, the style and number of which is defined by the user (by the use of the "MAKETHIN" command), symplectic integration is performed. Apertures of the elements, defined in the sequence, will trigger particle loss.

Many factors indicated the use of MAD-X over TRANSPORT in the optimization procedure of the present thesis, and specifically MAD-X's powerful and numerous matching algorithms, as well as the ability to impose constraints on the range of the varied parameters were among them. The ease with which the input and output of MAD-X can be linked with codes such as Wolfram Mathematica ®, and the ability to have an all-in-one tool, optimizing the optics and running a realistic tracking simultaneously, prevailed.

3.3 PTC

PTC ("Polymorphic Tracking Code") is a widely used, thick-lens symplectic tracking code. It exists independently of MAD-X, but has been implemented in its environment as a separate library. The beamline sequence as well as the applied misalignments, defined in MAD-X, can be transmitted to PTC.

One cannot define 'orders' in PTC, in the sense that it does not use a Taylor expansion of the equation of motion. PTC allows the user to define the degree of exactness of integration, by using either the exact or the expanded Hamiltonian, discussed in Section 2.7. The precision can be determined via the integration scheme and the number of integration steps in each element [26].

PTC is currently considered the most accurate tool in simulating particle trajectories. Due to the nature of integration, PTC is exact even for large spatial, angular and momentum offsets, in contrast to tracking codes as "TWISS" or "TRACK", and therefore has been used in the subsequent analysis.

3.4 Comparison of the optics and tracking codes

The first part of the current thesis consisted of a detailed study of the various optics and tracking codes available, in order to understand their limitations, applicability, differences in element and variable definitions and pitfalls.

As a first step, the R-matrices provided by TRANSPORT and MAD-X were compared with each other, as well as with analytical multiplications, using the described in Chapter 2 matrices obtained via Wolfram Mathematica®. MAD-X uses double precision variables, therefore there is absolute agreement with the analytical computations. TRANSPORT, being an older program, uses single precision variables and therefore cumulative multiplications can lead to differences in the 4^{th} decimal point at the end of the beam line. However, these are considered insignificant, since usually a matching to the 3^{rd} decimal point is considered sufficient.

3.4.1 Demonstration of the limit of first order calculations

In the limit of small spatial, angular and momentum offsets from the reference trajectory, the first order calculations and the results provided by the various tracking modules available coincide. As these initial offsets increase, higher order terms are introduced, and the results obtained in the various tracking codes gradually deviate.

The applicability of the first order approach is determined by the particle "accep-

tance". The particle acceptance is defined as the distribution of particles at the production point that will be transmitted through the beamline without being absorbed by its apertures (and therefore is a subset of the emittance). Since the particle acceptance is determined by the magnet placement and apertures, as well as the dipole and quadrupole currents, it is not clear when designing a beamline if the first order approach will suffice. A posteriori, for H2-VLE the spatial acceptance is $\sigma_{x,y}\sim 3-4\,\text{mm}$, the angular $\sigma_{x',y'}\sim 5-7\,\text{mrad}$, while the momentum acceptance reaches $\sigma_\delta\sim 5\%$. The acceptance for H4-VLE is similar as well.

In Fig. 3.1, particles with initial spatial and angular offsets in the horizontal plane have been tracked along the H2-VLE beamline that will be described in Chapter 4, starting from the T22 secondary target (S=0 m), until the end of the NP-02 detector ($S\simeq$ 60 m) and specifically, the cases (a) $x_0 = 10\,\text{mm}$, $x_0' = 10\text{mrad}$ and (b) $x_0' = 20\,\text{mrad}$ have been investigated. The particles have been tracked either using the 1^{st} order approach, or the "PTC_TRACK" module, described in 3.3. On the left side, the particle trajectory is shown for both the first order approach and via PTC, while on the right side the relative difference of the two methods is plotted along the line.

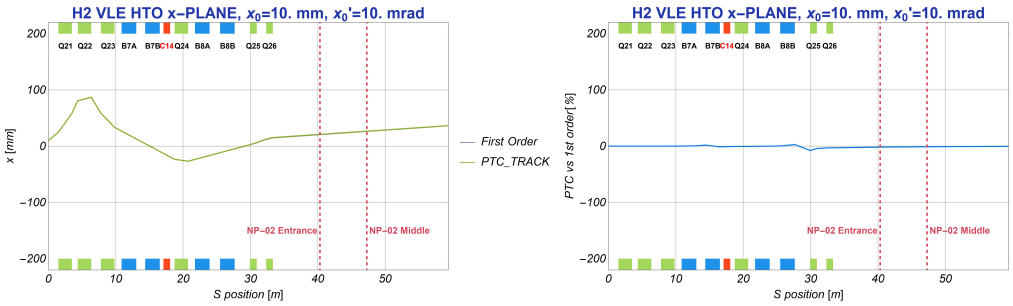

(a) $x = 10\,mm$, $x' = 10\,mrad$

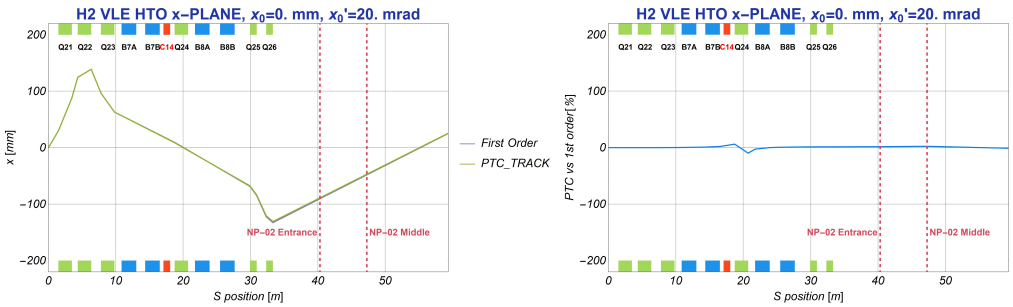

(b) $x' = 20\,mrad$

Figure 3.1: *Comparison between 1^{st} order and the PTC module for various initial particle coordinates in the horizontal plane. On the left side, the particle trajectory is shown for both the first order approach and via PTC, while on the right side the relative difference of the two methods is plotted along the beamline. Even for large spatial and angular initial offsets, the difference between 1^{st} order and the exact solution is negligible.*

The apertures drawn illustrate the elements of the beamline. The green boxes denote the beamline's quadrupoles, while the blue ones correspond to its dipoles. The red box, designated 'C14' denotes the collimator, while the entrance and middle of the cryostat

has been marked with a dashed line. It is reminded that, a particle generated with zero initial spatial, angular and momentum offsets defines the curvilinear coordinate system and therefore, by definition, will retain its zero coordinates throughout the beamline.

The particles have been chosen to be either in the limits of the beamline acceptance (case (a)) or off it (case (b)), to ensure that the results will be applicable in the actual particles emitted from the secondary target. The observed relative difference between the first order approach and PTC is maximized in case (b), where, at the exit of Q24, it reaches $\sim$9 % (since both coordinates are very small), but generally is kept below $\sim$1%. The above demonstrates that the first order approach is sufficient and stable, for all particles within or out of the beamline spatial and angular acceptance, but having the reference momentum.

The situation changes once momentum offsets are introduced. Fig. 3.2 shows the results obtained for different momentum offsets, $\delta = 5\%$ and $\delta = 10\%$. With the momentum acceptance of the beamline being $\sigma_\delta \sim 5\%$, tracking particles with a 10% or even 15% momentum offset is quite realistic. For large momentum offsets, terms on the right-hand side of (A.4) such as chromatic effects in quadrupoles (term $kx\delta$) or higher order corrections in the trajectory of off-momentum particles in a dipole magnet (term $\kappa_{0x}\delta$) can become quite significant. The effects are cumulative, and result in a particle trajectory that does not resemble at all the expected in first order. To conclude, the 1^{st} order approach is not adequate in the VLE beamline tracking.

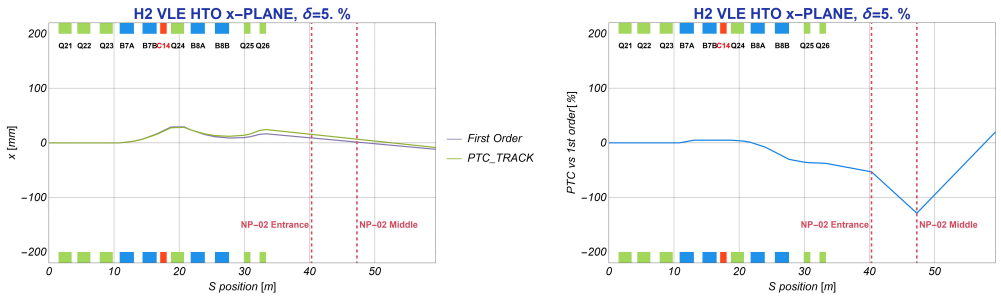

(a) $\delta = 5\%$

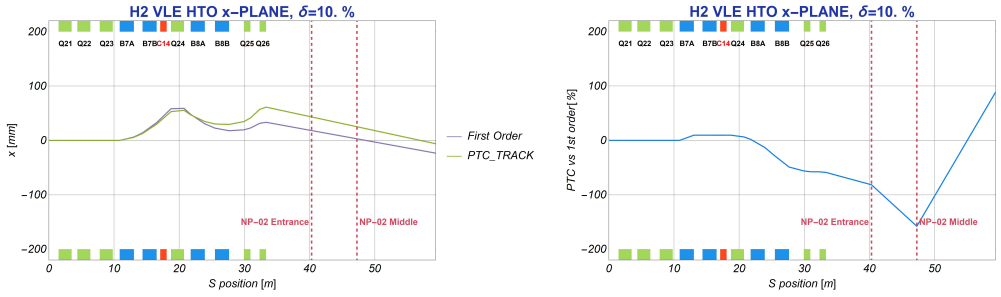

(b) $\delta = 10\%$

Figure 3.2: *Comparison between 1^{st} order and the PTC module for various momentum offsets. On the left side, the particle trajectory is shown for both the first order approach and via PTC, while on the right side the relative difference of the two methods is plotted along the beamline. The two approaches begin to diverge once significant momentum offsets are introduced.*

CHAPTER 4

H2-VLE and H4-VLE extensions

As discussed in Section 1.4, the existing H2 and H4 beamlines cannot meet the requirements of the NP-02 and NP-04 experiments, necessitating the design of two beamline extensions. This chapter describes the design considerations and the final layout of the VLE (**V**ery **L**ow **E**nergy) beamlines, as well as their initial optics configurations.

4.1 VLE beamline requirements and implementation

The need to provide the new experiments with low energy pions and kaons supported the use of a secondary target towards the end of the existing H2 and H4 beamlines, thus regenerating unstable particles closer to the experiments. A conceptual layout for either H2-VLE or H4-VLE from the primary T2 target up to the NP-02 or NP-04 cryostat respectively is shown in Fig. 4.1. The extension length of about $\sim$40 m was the result of a compromise between the requirement to fit the necessary magnetic elements and the desire to be kept as short as possible, thus increasing the percentage of pions and kaons reaching the detectors (see Fig. 4.2).

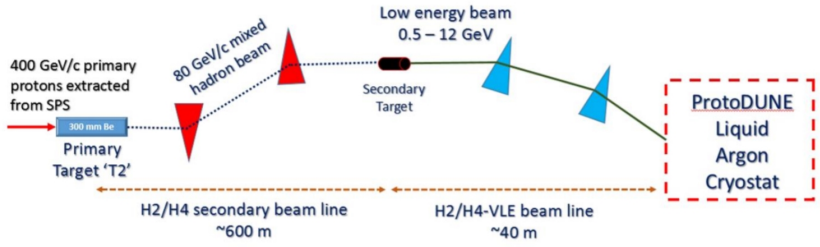

Figure 4.1: *Conceptual layout of the H2 (H4) beam line, along with the H2 (H4)-VLE extension, leading to the NP-02 (NP-04) detector. [10]*

Due to the quite low maximum data acquisition rate of the detectors ($\sim$100 Hz [11]), the main design consideration for the two extensions was the minimization of the exposure of the two cryostats to the muon halo generated by the interaction of the hadron beam with the secondary targets, primarily towards the forward direction. The above has been achieved by installing each cryostat inside a pit partially below the floor, thus reducing the background considerably. In order for the beam to reach the cryostat entrance, a configuration of dipole magnets has been designed, providing a total deflection angle of 231.6 mrad in H2-VLE and 240.06 mrad in H4-VLE. By placing the magnets by

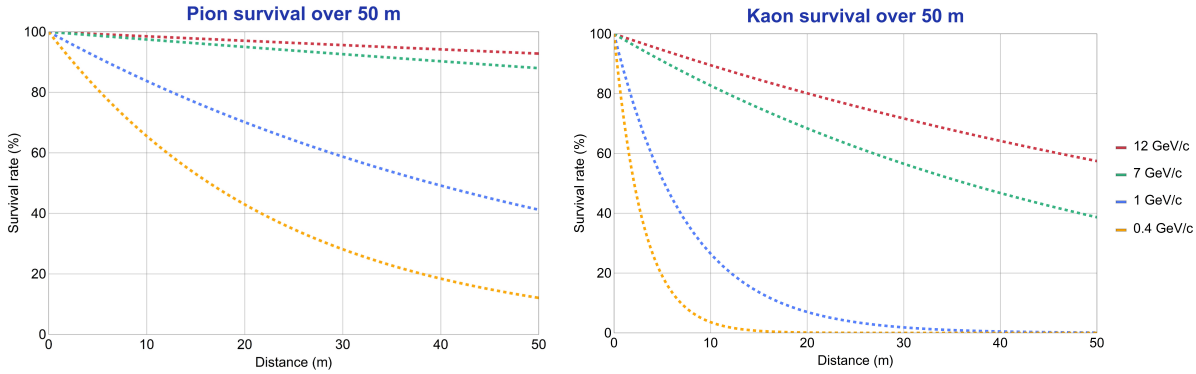

(a) **(b)**

Figure 4.2: *Survival rate of π and K. Even for a short beamline of 40 m, the surviving K below 1 GeV/c are quite limited.*

34.3° in H2-VLE and 56.75° in H4-VLE with respect to the floor, the beam is steered away from the direction of the muon halo simultaneously downwards and to the right, as shown in Fig. 4.3. As will become clear, the dipole configuration at the same time constitutes the momentum selection station of the beamlines.

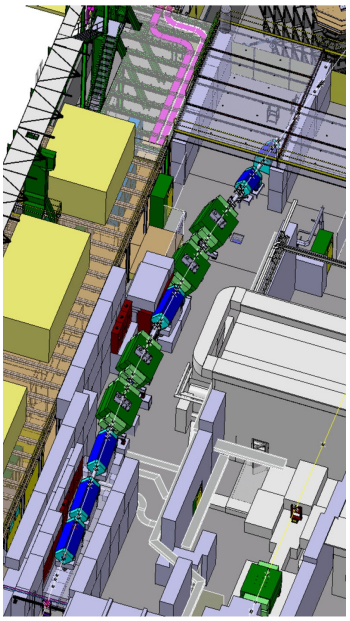

(a) *H2-VLE 3-D layout*

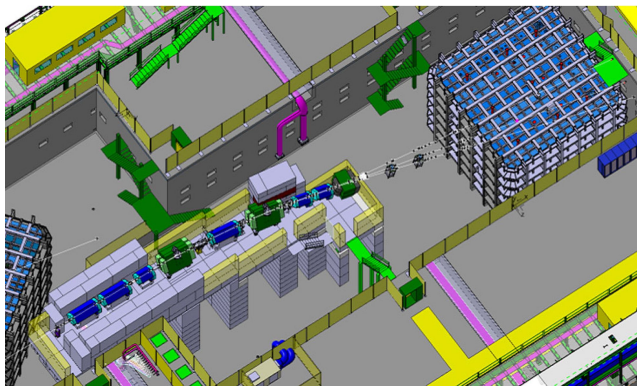

(b) *H4-VLE 3-D layout*

Figure 4.3: *Detailed 3D-view of (a) H2-VLE and (b) H4-VLE. The tilted placement of the elements is evident. The three deflection configurations of H4-VLE, leading to the different entrance points of NP-04 are discernible.*

4.2 Conceptual low energy beamline design

The desire to keep the beamline length as short as possible, and the requirement for large total deflection angles indicated the integration of a two bend achromat with field lens configuration for both VLE beamlines.

A typical configuration is shown in Fig. 4.4. Two dipole magnets, designated *BM1* and *BM2*, each providing an equal deflection angle θ, will result in a total deflection angle 2θ for the reference trajectory. Since the bending angle defines the beamline geometry, depending on the requested nominal momentum, the magnetic field of the dipole magnets is adjusted accordingly. As illustrated by the solid line, the nominal momentum beam should be brought at a focus at the collimator, the beam size at this position being mainly defined by the momentum spread. The focusing in the collimator is achieved via a quadrupole doublet in the particular example, but, as will be explained later, in the VLE beamlines a quadrupole triplet was preferred. Due to the increasing R_{16} term introduced by the first dipole of the beamline, particles having a large momentum offset (indicated by the dashed line) will be absorbed by the collimator jaws, the aperture of which determines the $\delta p/p$ acceptance (according to Eq. 2.16). A focusing quadrupole (or "field lens", designated Q_3 in the figure) placed symmetrically in between the two bending magnets allows for momentum recombination and dispersion control (nullification of the R_{16} and R_{26} terms after the second dipole).

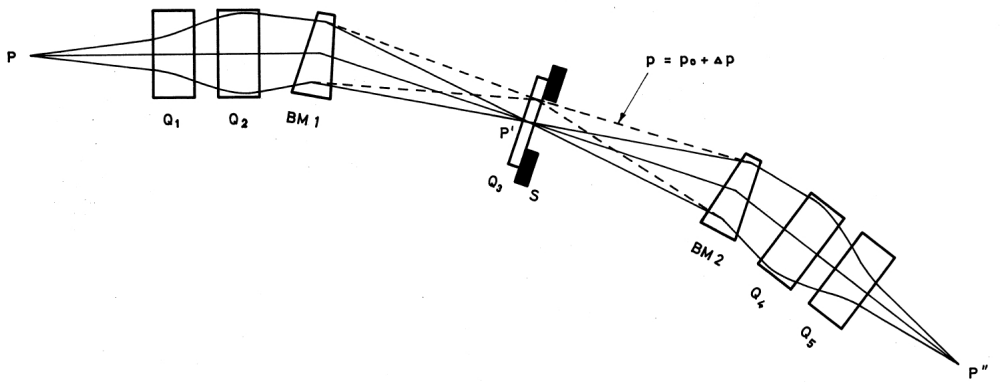

Figure 4.4: *Typical two bend achromat with field lens configuration. [15]*

This configuration has been implemented in both VLE beamlines, although in H2-VLE two bends, instead of one, are used for the momentum analysis and two additional for the momentum recombination. To satisfy the maximum momentum acceptance, $\sim$5% in RMS, in both beamlines, a collimator of a maximum jaw opening of 45 mm half gap has been used. By reducing the collimator gap, the momentum bite can be further minimized.

Space limitations between the magnetic elements due to the positioning of the vacuum flanges forced the spectrometer magnets of both beamlines to be placed slightly asymmetrically. This results inevitably in a non-zero dispersive derivative, marginally contributing to the beam size at the experiments, as will be shown in the subsequent

studies.

Apart from the momentum selection station described above, consisting of a focusing quadrupole and two bending magnets of equal strength (four, in the case of H2-VLE), the particle acceptance maximization is achieved with the use of an initial quadrupole triplet downstream the secondary target, designed to simultaneously focus the beam at the collimator. A final quadrupole doublet serves to focus the beam at the experiment.

The described layout is shown schematically in Fig. 4.5, including the instrumentation of the two lines, that will be explained in Section 8.1.

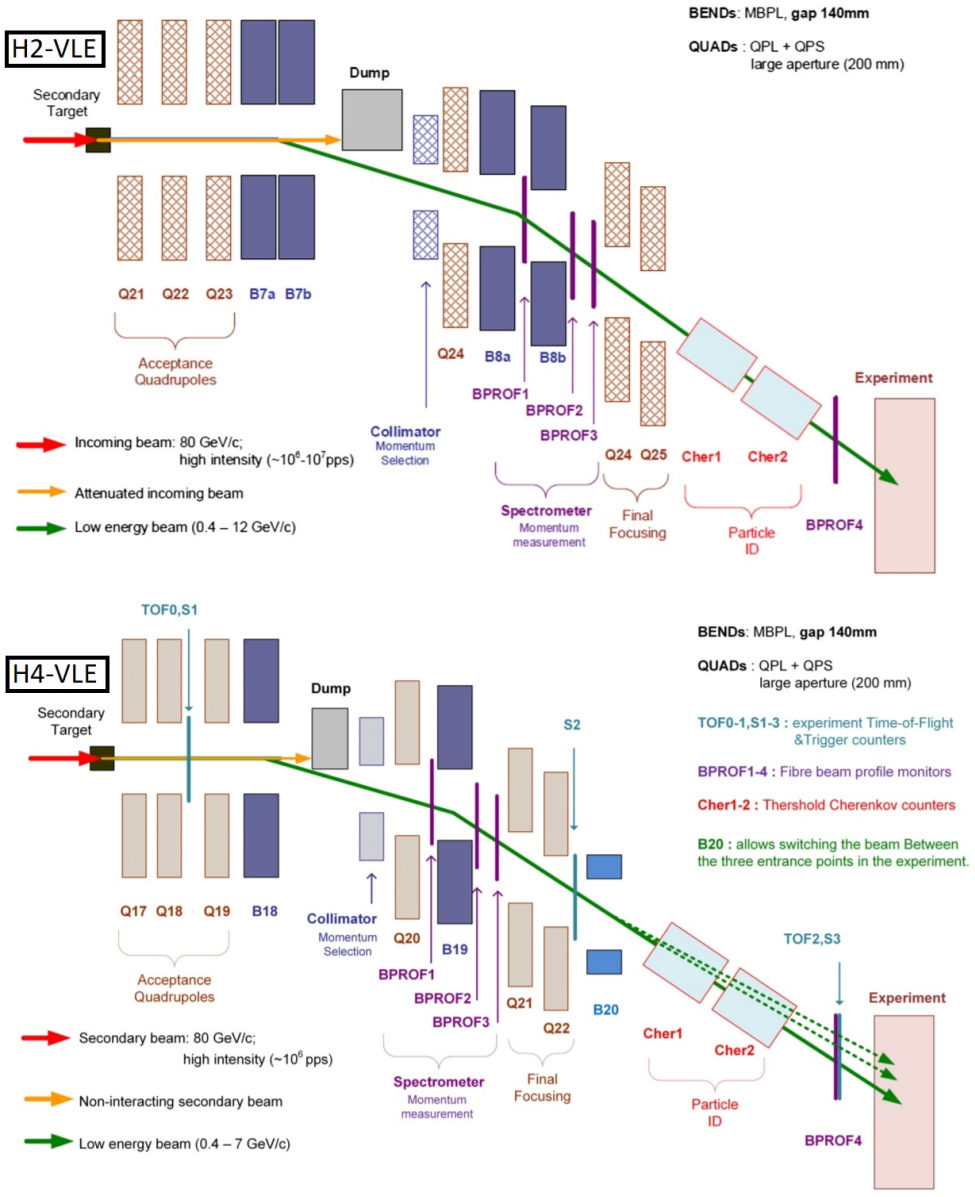

Figure 4.5: *Schematic layout of H2-VLE and H4-VLE [10].*

4.3 Other characteristics

Specifically for the NP-04 detector, various beam entrance points have been explored, aiming to limit the hadronic showers to one its two drift volumes [7]. For this purpose, a final horizontal dipole will deflect the beam accordingly to reach the three designed points of the NP-04 cryostat, as shown in Fig. 4.5.

The quadrupole magnets, either "QPL" (2 m long) or "QPS" (1m long) type, are designated Q21-Q26 in H2-VLE, and Q17-Q22 in H4-VLE. In H2-VLE the dipole magnets are designated B7a, B7b, and B8a, B8b, to denote their powering schema configuration. In H4-VLE the magnetic spectrometer dipoles are designated B18 and B19, while the final steering dipole B20. All dipoles are "MBPL" (2 m long) type, apart from B20 which is an "MBPS" (1 m long). The magnets specifications (excitation curves, maximum currents, dimensions, etc.) can be found in [12]. The collimator of each beamline, notated as "C14" in H2-VLE and "C12" in H4-VLE, is placed with its jaws parallel to the bending plane.

In order to keep the budget at reasonable levels, the use of already existing magnets and power supplies was preferred, imposing constraints to the maximum current of the quadrupoles. Appropriate shielding has been installed around the secondary targets, thus protecting the surrounding control rooms. To absorb the particles that have not interacted with the target, a beam dump has been placed before the collimator of each beamline. Both extensions are in vacuum from the secondary target to the entrance of the cryostats.

4.4 Initial optics design and optimization motivation

The final placement of the magnets and the design of the initial optics was the result of an optimization process realized via the optics code TRANSPORT, presented in [10]. The initial optics design, shown in Fig. 4.6 for the horizontal and the vertical plane, attempted to achieve a first compromise among the experimental requirements, as well as space and budget constraints.

In Fig. 4.6, the green boxes illustrate the quadrupoles of the beamlines, while the blue ones illustrate the dipoles. The red box corresponds to the collimator of each beamline. The entrance of each cryostat is marked in the figures with a dashed vertical line.

It should be noted that, since all the magnets, apart from B20, are placed with the same tilt angle in each beamline and the production at the secondary targets is isotropic, rather than using a reference system with respect to the EHN1 floor ($x - y$ reference system), it is wiser to use a new reference system for each beamline, rotated along s (the beam axis) by the tilt angles $\theta_{t,1} = 34.3°$ for H2-VLE and $\theta_{t,2} = 56.75°$ for H4-VLE respectively ($x' - y'$ reference system). In the analysis below, whenever 'horizontal' (or 'bending') and 'vertical' (or 'non-bending') plane is mentioned, the x' and y' planes are to be understood respectively, unless stated otherwise. In this way, the dipole field of the spectrometer magnets is parallel to the y' axis of each beamline. Therefore with this convention, for H2-VLE there exists a dispersive term only in the bending plane, while for H4-VLE, a dispersive term in the non-bending plane is introduced only after the

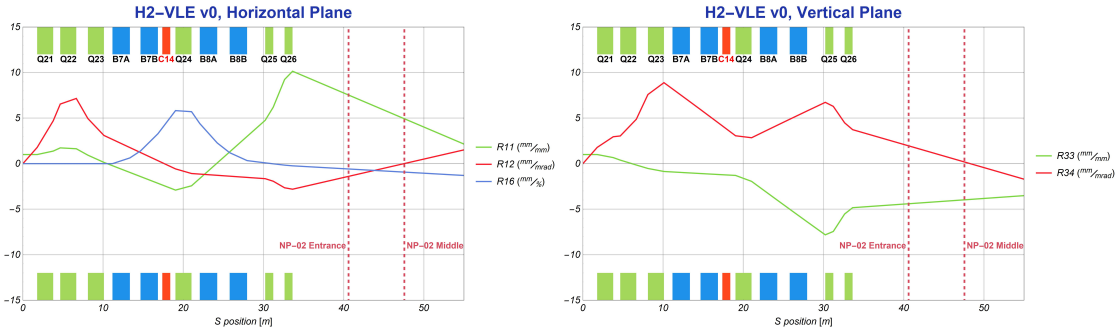

(a) *H2-VLE initial optics configuration*

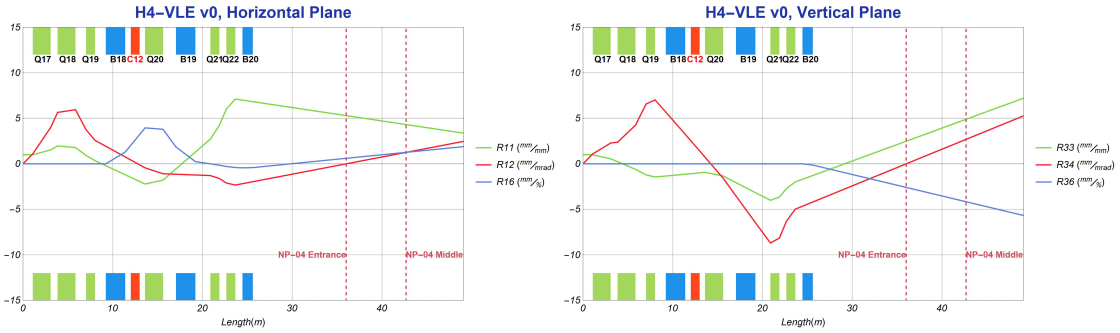

(b) *H4-VLE initial optics configuration*

Figure 4.6: *Original optics design for (a) H2-VLE (b) H4-VLE, optimized via the optics code TRANSPORT.*

final dipole magnet (B20), which is placed with respect to the floor. The diverging R_{16} term after the momentum selection station is discernible in both beamlines, indicating a non-zero R_{26} term due to the asymmetric positioning of the spectrometer magnets.

The beam focusing requirements analyzed in the previous section are translated into various constraints in the matrix elements at specified positions. To achieve a beam waist (a minimum of the beam size) of a nominal momentum beam, for example in the horizontal plane, the R_{11} and the R_{12} terms must be minimized. Since Liouville's Theorem prohibits the nullification of both terms at a single position (see Section 2.2), a compromise between the two terms is always essential. This compromise is determined by the initial target emittance and specifically, for point-like targets, the angular spread is significantly larger than the spatial, and therefore the spot size at each position is mainly defined by the R_{12} term, the nullification of which leads, in first order, to a beam waist. Alternatively, for an initial emittance being mainly dominated by a spatial spread, the contribution of the R_{11} term is of major importance.

Since, due to time pressure, during the initial optics optimization the target emittance had not yet been simulated, in the original optics version the rate maximization and beam focusing was mainly realized via the control of the R_{12} term. Subsequent tracking studies, analyzed in Section 5.1, implementing the actual emittance from the secondary targets will indicate that, due to the secondary target geometry and the secondary beam properties, in the case of the VLE beamlines, the magnification term affects

significantly the beam size as well.

It became clear, therefore, that new optics could be found, leading to an increase in the particle rate or more focused beams at the experiments. Indeed, in the low energy region (<4 GeV/c) the expected 'useful' rate at the experiment (consisting of p, K and π) is quite below the maximum acquisition rate of the cryostats ($\sim$100 Hz). For example, for a 2 GeV/c beam the pion rate is expected to be below 20 Hz, while for the 1 GeV/c case, this rate drops to $\sim$5 Hz [23]. A particle rate increase is quite crucial for the experiments, since it automatically leads to a proportional beam time decrease. A more focused beam at the cryostats could also be critical, meaning less particles escaping the active volume without being detected.

CHAPTER 5

Optics optimization of H2-VLE and H4-VLE

After the consideration and comparison of the features of the optics and tracking codes available in Chapter 3, and after the outline of the layout and initial optics of H2-VLE and H4-VLE in Chapter 4, the optics optimization procedure of the two beamlines can be described.

To proceed to the optimization, it is necessary at first to examine the two major factors that determined the optics optimization approach, which were, (a), the realistic emittance from the T22 and T24 targets and (b), the magnetic aperture limitations of the beamline elements.

5.1 Target emittance for the design momentum

The optics optimization procedure is inseparable from the initial particle distribution at the secondary target. The "emittance" will define the contribution of the spatial, angular and dispersive terms in the beam size at each position and introduce correlation terms between the various coordinates. To successfully control the beam size throughout the line, the optimization must concentrate on the contributions that mostly determine it at each point along the beamline.

As was already mentioned, due to time pressure the initial optics optimization was performed without knowledge of the specific target emittance. In later studies, after having modeled the detailed upstream H2 and H4 beams in G4BeamLine ([27]), the distribution of tertiary particles produced by 10^7 secondaries of 80 GeV/c impinging on the 'default' secondary target of a copper cylinder for both beamlines, 30 cm long and 3 cm in radius, was simulated (courtesy of Dr. Marcel Rosenthal).

The generated tertiary particles, π, p, K, e and μ of both positive and negative polarities, have a momentum range up to 80 GeV/c. Since the two beamlines will be optimized for their design momenta, which are +12 GeV/c for H2-VLE and +7 GeV/c for H4-VLE, specifically the particle distributions in these momenta range will be examined. In Chapter 6, the corresponding particle distributions for 1 GeV/c nominal momentum will be analyzed, and the overall consistency of the VLE beam characteristics will be demonstrated.

To reduce the computing time, an initial selection of particles based on their mo-

menta was conducted. This selection was based on the expected momentum acceptance of the beamlines, that can be computed in first order via Eq. (2.16), by the R_{16} term at the collimator, as well as the collimator maximum half gap, which is 45 mm. By selecting π^+, p^+, K^+ and e^+ of 12 GeV/c ±15% from the T22 target and 7 GeV/c ±15% for the T24 target over the entire spectrum of production, the study is completely unbiased. Muons have not been taken into account in the optimization analysis since they are not interesting particles for the experiment.

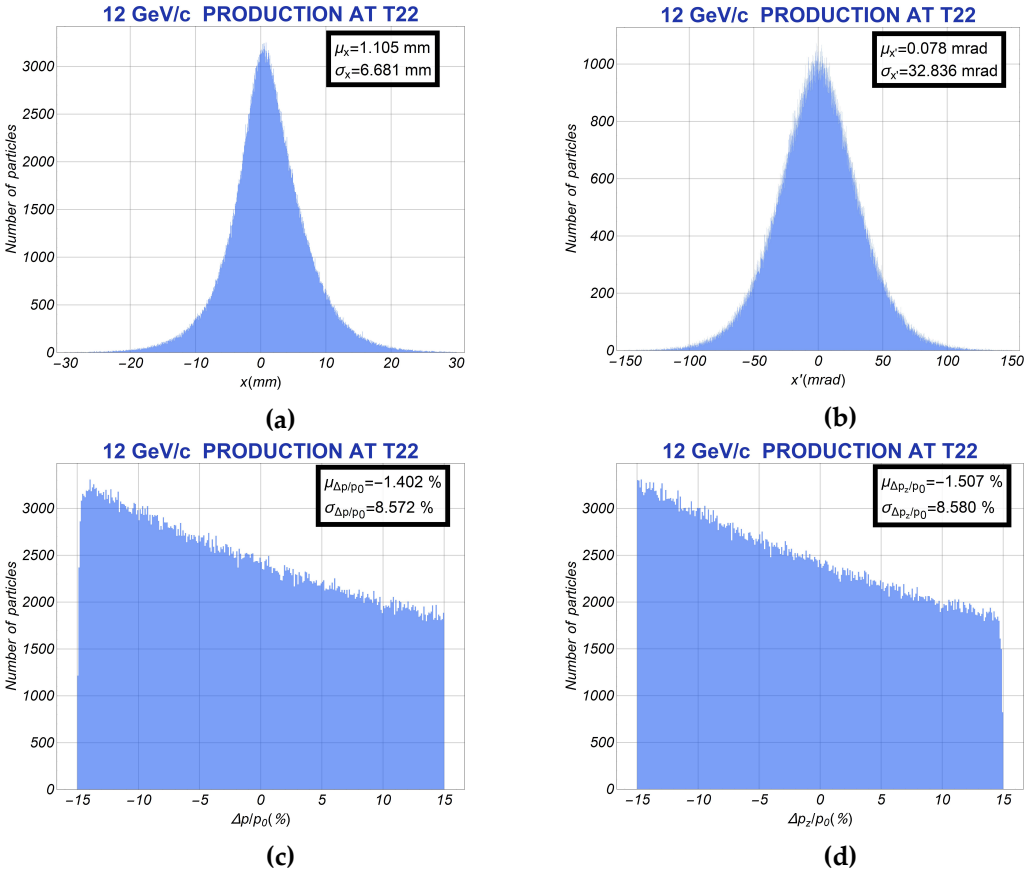

Figure 5.1: *12 GeV/c ±15% π, p, K, e production at T22 for 10^7 secondaries simulated via G4BeamLine, using the 'default' target. Shown is the spatial, angular, momentum and longitudinal momentum distribution right after the secondary target.*

Figs. 5.1 and 5.2 show, for the design momentum of each beamline, the horizontal spatial and angular distributions of particles with respect to the EHN1 hall, as well as the momentum and longitudinal momentum distributions of the T22 and T24 targets respectively. For H2-VLE, a slight offset of ∼1 mm is evident in the horizontal plane, due to a minor asymmetry in the impinging H2 beam on T22. The vertical plane (not shown) does not exhibit an asymmetry, and is almost identical in terms of spread with the horizontal plane. For H4-VLE, a similar asymmetry in the impinging H4 beam introduces an offset of 0.7 mm in the horizontal and -1.4 mm in the vertical emittance.

Both figures illustrate that, for each target, the angular distribution has a ∼4-5 times

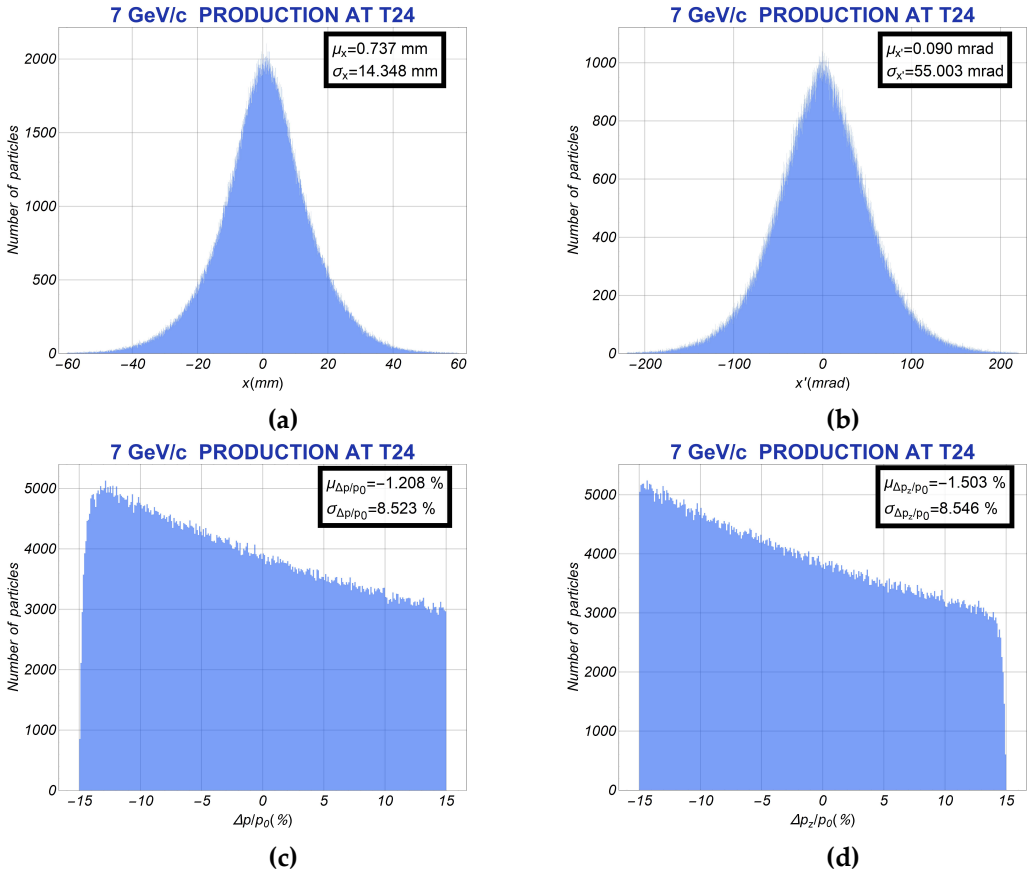

Figure 5.2: *7 GeV/c ±15% π, p, K, e production at T24 for 10^7 secondaries simulated via G4BeamLine, using the 'default' target. The overall shape is similar to the 12 GeV/c ±15% particle production at T22, although more spread out.*

larger RMS than the corresponding spatial distribution. However, if aperture limitations of the two VLE beamlines are taken into account, the acceptance (defined in subsection 3.4.1) will be reshaped. Specifically, as will be shown later, subsequent studies will indicate that for H2-VLE, for either the horizontal or vertical plane, the spatial acceptance RMS is ∼3-4 mm and the angular ∼5-7 mrad, making the contribution of the former quite significant for the beam size as well. Even more striking is the case of H4-VLE, where the spatial acceptance reaches ∼8-10 mm, while the angular is ∼6-8 mrad. For both beamlines, the spatial contribution can therefore by no means be neglected.

Figs. 5.1c and 5.2c illustrate a slight preference for lower momenta, a property amplified tremendously in the 1 GeV/c ±15% case, that will be shown in Chapter 6. Specifically, for 10^7 secondaries of 80 GeV/c impinging on T22, the particles generated with a momentum in the range of [0.85,1.15] GeV/c are two orders of magnitude more than those in the range of [10.2,13.8] GeV/c. The momentum and longitudinal momentum distributions are almost identical for the design momentum of each beamline. However, they will be compared with the 1 GeV/c case, where the two distributions will be completely different.

Fig. 5.3 demonstrates the correlations between the various coordinates of the target +12 GeV/c ±15% production, and specifically the (a) x-x', (b) x'-y', (c) x'-$\Delta p/p$ and (d) $\Delta p_z/p$-$\Delta p/p$ phase spaces are shown.

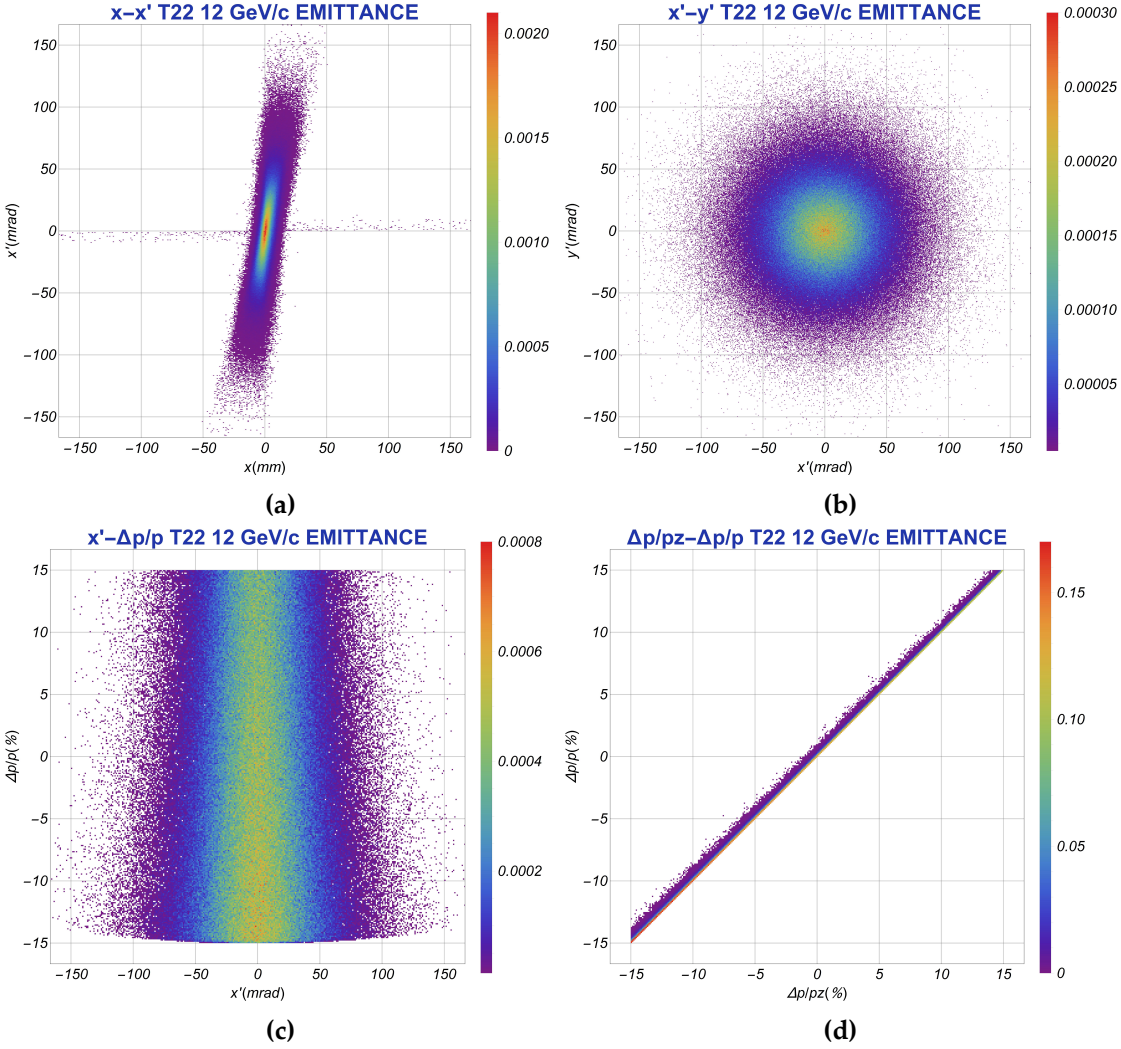

Figure 5.3: *Correlations between (a) x-x', (b) x'-y', (c) x'-$\Delta p/p$ and (d) $\Delta p_z/p$-$\Delta p/p$ coordinates of the 12 GeV/c ±15% emittance at T22.*

It is clear that the x'-y' coordinates (as well as the x-y coordinates, not shown) are uncorrelated, due to the cylindrical symmetry of the configuration. However, a correlation between the x-x' coordinates (and, similarly, the y-y' coordinates) is evident, illustrated by the tilt of the elliptic-like phase space in Fig. 5.3a. The corresponding phase spaces for the T24 7 GeV/c particle distribution demonstrate similar correlations and are not shown.

5.2 Beamline geometry and aperture limitations

The rate increase at the experiment is based in an overall beam size control, resulting in a reduction of the particle losses in the magnetic apertures. Due to the focusing nature of the quadrupoles in one plane and the defocussing nature in the perpendicular plane, there will be positions where the beam is diverging, leading to an increase in the spot size, and positions where the beam is converging, decreasing the spot size. The positions where the beam should be particularly controlled are defined by the magnetic apertures.

Figure 5.4 illustrates the H2-VLE and H4-VLE geometries in the horizontal and vertical plane. As already mentioned in Section 4.4, the reference system for each beamline has been rotated along the s axis by the tilt angles $\theta_{t,1} = 34.3°$ for H2-VLE and $\theta_{t,2} = 56.75°$ for H4-VLE respectively, so that the new vertical axis of each line is now parallel to the magnetic field of the spectrometer magnets. The 'horizontal' and 'vertical' planes used are defined by the new reference systems.

The apertures demonstrate the elements confining the particle transmission the most. In the tracking simulations, all dipole magnets have been modeled as rectangular, having a half aperture of 210 mm in the horizontal plane and 70 mm in the vertical plane. The aperture of the quadrupoles has been modeled as circular, 100 mm in radius.

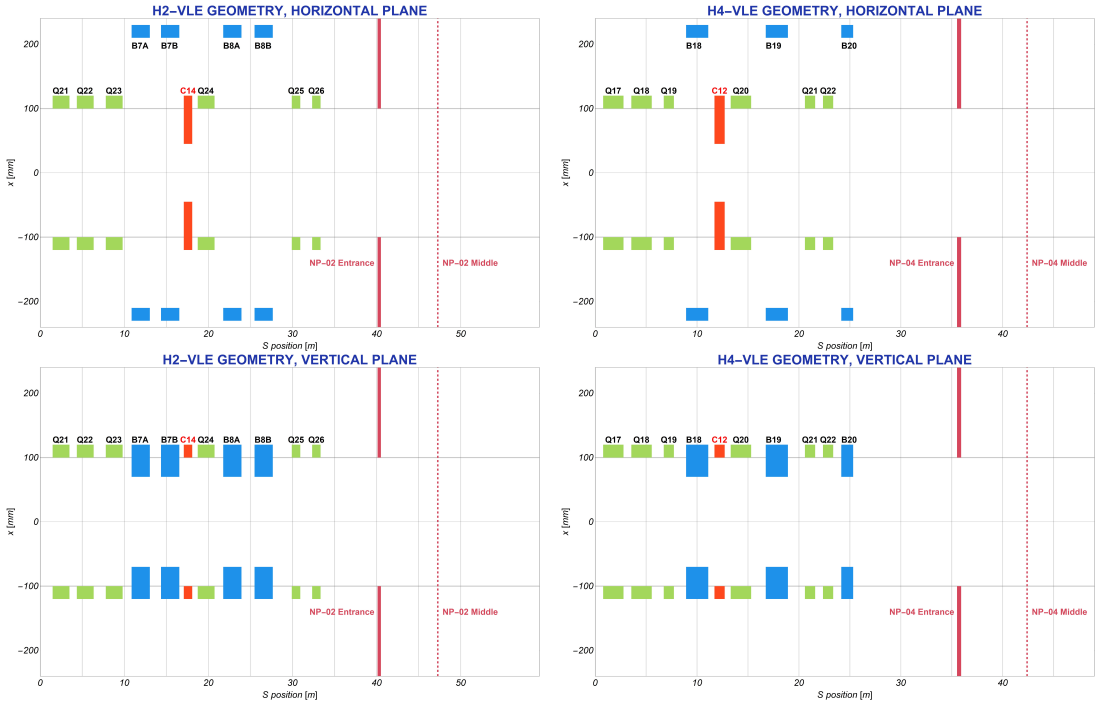

Figure 5.4: *H2-VLE and H4-VLE geometries in the horizontal and the vertical plane. The collimator is at its full opening, 45mm half gap. The "NP-02/NP-04 Entrance" denotes the circular entrance of each detector, 100mm in radius.*

It can be seen that the vertical apertures of the dipoles, having a half gap of only 70 mm, is the most constraining factor. The optimization procedure will therefore focus

in the control of the vertical beam size at the dipole positions, by carefully adjusting the contribution of the R_{33} and R_{34} terms. Additionally, in the case of H4-VLE, the final dipole magnet, designated B20, is placed with respect to the floor (or by $-57°$ with respect to the plotted $x' - y'$ reference system), as shown in the right side of Fig. 5.5. The maximum horizontal and vertical particle coordinates as 'seen' by the $x' - y'$ reference system are no longer independent, but have to lie within the area mainly defined by the two poles of B20 (indicated with green in the right side of Fig. 5.5). It is therefore clear that, at the position of B20, the beam has to be contained simultaneously in the horizontal and the vertical plane. Since the horizontal extent is now more restricted, particular emphasis should be given in the control of the beam in the horizontal plane. The now correlated maximum apertures of B20 cannot be drawn in an S-x and S-y plot, and therefore the initial apertures are kept for consistency, but the reader must remember that they do not correspond to the real geometry.

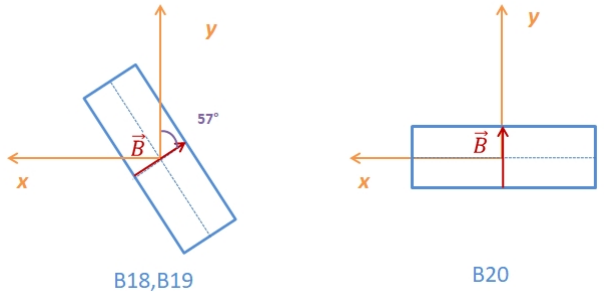

(a) $x - y$ *reference system*

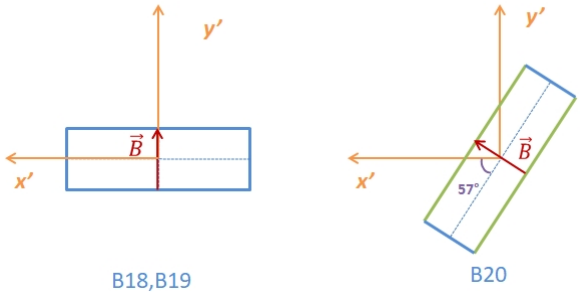

(b) $x' - y'$ *reference system*

Figure 5.5: *Aperture limitations as 'seen' by the two reference systems for B18 or B19 (left) and B20 (right)*

In addition to controlling the beam envelope at the dipole positions, it is equally significant to achieve a focus of the beam at the collimator. Ineffective focusing will result in absorption of particles having initial spatial and angular offsets, rather than off-momentum particles.

5.3 H2-VLE and H4-VLE optimization

For the VLE beamlines optimization, the link between MAD-X and Wolfram Mathematica ® has been exploited in order to automate the procedure. A powerful tool, that will be demonstrated in 5.3.1 has been developed, which is guaranteed to explore the entire phase space of available optics configurations that satisfy the given by the user initial constraints on the matrix elements at specified positions. While the automation of the optimization process is an essential advancement, as will become clear in the subsequent analysis, it does not suffice for the design of a successful optics, but, rather, a deep understanding of the beam optics is always essential.

Since the installation of the magnets of the two VLE beamlines is already finished, the optics optimization is reduced for each beamline to only six degrees of freedom, corresponding to the currents of the six quadrupole magnets. The limited number of degrees of freedom, along with the various constraints (discussed in 4.4) that need to be balanced in the optimization process rendered the development of an 'all in one' optics mode impossible. For this reason, two optics configurations will be proposed for each beamline. The 'High Transmission Optics' will provide better particle transmission, resulting in a rate increase at the two cryostats, and the 'High Resolution Optics' will provide a more focused beam at the experiments and a decrease in the spot size.

Moreover, the aforementioned constraints indicated that the optimization process be scaled down to two separate steps. The first step consists of the optimization of the first quadrupole triplet, aiming to achieve a generally contained beam, and bring the beam in the horizontal plane at a focus in the collimator, allowing for a momentum selection of the particles. In the second step, a momentum recombination and the final focusing at the experiment is attempted.

5.3.1 Step 1: H2-VLE and H4-VLE triplet optimization

The first step in the optimization of H2-VLE and H4-VLE consisted of exploring the entire phase space of solutions for their quadrupole triplets. The degrees of freedom available for each beamline were the three quadrupole coefficients, k_1, k_2, k_3, limited within the power supply range. The constraint imposed in the optimization process was to bring the beam at a focus at the collimator, translated to nullifying the R_{12} and R_{34} terms. While the momentum selection occurs in the horizontal plane, a simultaneous focus of the beam in the vertical plane was initially attempted. However, as will become clear, the focus in the vertical plane had to be abandoned in order to successfully match the entire beamline. Nonetheless, the triplet optimization can be considered as a first "exercise", and can demonstrate the power of the MAD-X / Mathematica cross - talk.

In order to keep a large angular acceptance, an additional constraint was imposed, that the $|R_{12}|$ and $|R_{34}|$ terms are kept below 10 mm/mrad. With the quadrupole apertures being 100mm in radius, this constraint ensures that particles generated at the target with less than 10mrad will be transfered successfully by the first three quadrupoles.

For the matching process, the initial k-values, as well as the initial step size for the varying parameters need to be defined. Since different initial step and k-values result to

different matching results, these have been varied in the Mathematica script, via nested loops. For each iteration, Mathematica generates the necessary input files that MAD-X needs to begin the optimization process and invokes MAD-X. MAD-X then attempts to match, the process being terminated either successfully, or after a certain number of iterations has been completed. The final R-matrix values are printed in an output file via the TWISS module, that is then imported by Mathematica. After checking that, firstly, the R_{12} and R_{34} terms are close to zero in the collimator, within a tolerance of 10^{-3}, and that their absolute values do not exceed 10mm/mrad until the collimator, these k-values are stored in the system, and the next iteration begins. To avoid storing identical solutions, solutions identical within a tolerance factor of 10^{-5} for all three k-values simultaneously were rejected via Mathematica. After the process was finished, the solutions were sorted by decreasing k_1 values.

The results of the aforementioned optimization process for H2-VLE are shown in Figs. 5.6, and 5.7, while similar results were obtained for H4-VLE as well. Plotted in Fig. 5.6 is the phase space of obtainable solutions in terms of the k-values of the three quadrupole magnets. A positive k-value denotes a quadrupole focusing in the horizontal plane. Only two discrete areas in the phase space can be achieved, corresponding to the FDF (Focus-Defocus-Focus) and DFD (Defocus-Focus-Defocus) configurations. All other configurations (FFD, DDF, FDD etc.) cannot meet the imposed constraints. The two areas are completely smooth and have no irregularities.

The optimization problem is completely symmetric for both planes, since the range of the quadrupole coefficients is the same for positive and negative values and the constraints imposed are identical for both planes. This symmetry indicates that the solutions ought to be entirely symmetric as well, as is clear from Fig. 5.6.

The number of solutions found ($\sim$8500) possesses no physical meaning, but it simply is a consequence of the tolerance chosen for 'identical' solutions, and the tolerance in the nullification of the R_{12} and R_{34} terms. If one would decrease the tolerance of the R_{12} and R_{34} terms to, for example, 10^{-2}, then simply, more 'dots' would be added in between the solutions. It is noteworthy that, if one increases the tolerance to, for example, 10^{-5}, then the number of solutions is decreased, but the overall shape and range of the phase space is consistent.

In Fig. 5.7 the R-matrix element values in the middle of collimator C14 are plotted.

To conclude, for both beamlines the k-values phase space where a nullification in the middle of the collimator is achieved both for the R_{12} and R_{34} terms and the overall angular acceptance is kept above 10mrad consists only of two discrete and absolutely symmetric areas, corresponding to the FDF and DFD configurations.

Taking into account that the momentum selection occurs in the horizontal plane, apart from nullifying the R_{12} term, it is important to constrain, as much as possible, the magnification term as well. A large $|R_{11}|$ value would imply that, rather than selecting particles according to the momentum offset, particles with large initial offsets will be absorbed by the collimator. Therefore, the FDF configuration, providing a $|R_{11}|$ term close, or less than unity, seemed the most natural choice.

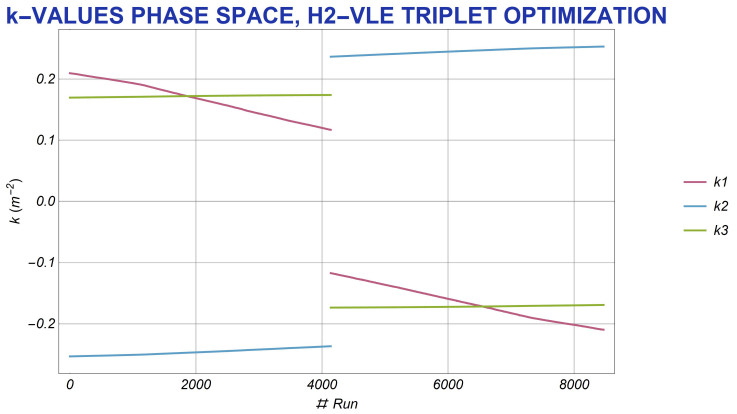

Figure 5.6: *Solution phase space for the H2-VLE triplet optimization sorted by the the k_1 values.*

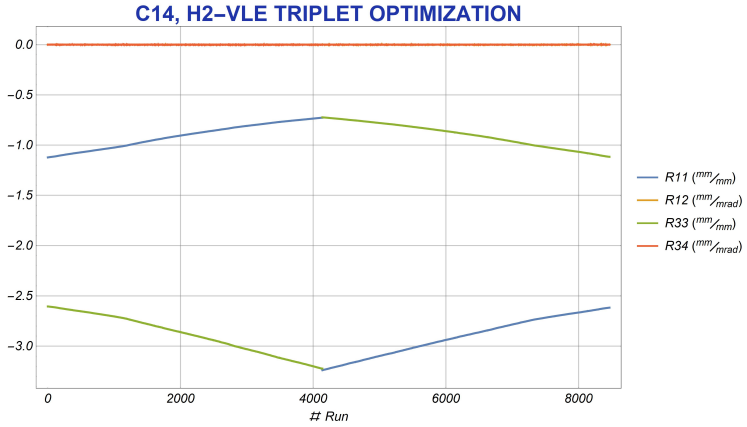

Figure 5.7: *R-matrix values in the middle of the collimator. The R_{12} and R_{34} terms are zero within a tolerance of 10^{-3}.*

5.3.2 Step 2: H2-VLE and H4-VLE optimization

The next step in the optimization procedure is to attempt to match the entire beamline. This is achieved by choosing a set of k-values for the quadrupole triplet, and varying the k-values of the field lens and the focusing doublet.

Initially, a matching was attempted by choosing the triplet k-values to be solutions of the above optimization analysis for both beamlines, and specifically a few of the FDF configurations were selected, better matching the focusing criteria at the collimator. It soon became clear that, by nullifying the R_{34} term at the collimator, it uncontrollably diverges in the next quadrupole (the focusing field lens), with an impact in the overall angular acceptance. Therefore, the nullification of the R_{34} term at the collimator had to be abandoned, and the triplet was re-optimized, this time attempting to obtain a relatively large R_{34} value (∼3-5 mm/mrad), resulting in a better control of the term. This characteristic has been implemented in all optics, both for H2-VLE and H4-VLE.

It must be noted that the developed MAD-X/Mathematica tool, while it can crucially

speed up and ease the procedure, is by no means a "deus ex machina", in the sense that, in order to produce results, it requires constraint impositions. Once constraints are imposed, the tool is guaranteed to identify all mathematically achievable configurations.

Since the beam size cannot be straightforwardly predicted by the R-terms, it is not trivial to impose the appropriate constraints on the matrix elements. Therefore, from this point the optimization has been an iterative process where initiatives had to be taken, driving the optimization towards a specific direction for each optics mode developed. The successful development of the final configurations has been an interplay between the understanding of the beam optics, the use of the developed MAD-X/Mathematica tool and tracking validation of the described in Chapter 5 particle distributions via PTC. For example, while in the beginning of the optimization a focusing in the experiment was attempted by nullifying the R_{12} and R_{34} terms, subsequent tracking simulations indicated that the focusing was insufficient and therefore, a different approach had to be devised. By attempting to minimize the magnification terms, the results improved significantly. Since the proposed optics are different in their execution, the two following subsections are devoted in the presentation of the final optics modes.

5.3.3 Final optics configurations for H2-VLE

Fig. 5.8 demonstrates the final optics configurations for the H2-VLE beamline.

The 'High Resolution Optics' is designed to provide a smaller spot size at the NP-02 middle, where the focus is aimed, and simultaneously a more evident beam waist, by better controlling the matrix elements in terms of their values at the experiment and in terms of their slope. Rather than recombining the momentum directly after B8B, the R_{16} term is nullified in the middle of the cryostat. In this way, the decreasing dispersion derivative contributes to the impression of a beam waist in the horizontal plane, and at the same time, the contribution of the R_{16} term in the beam size is avoided. Additionally, a vertical beam waist closer to the NP-02 middle is achieved by a steeper decrease, compared to v0, of the R_{33} term, with a simultaneous nullification of the R_{34} term. The 'High Resolution Optics' comes at the expense of potentially reducing the transmission; the vertical beam size at B8A and B8B is expected to be quite larger than the v0, due to the significantly enlarged R_{34} term, resulting in particle losses.

The 'High Transmission Optics' is based on a control of the vertical beam envelope at the dipole positions, resulting in a significant rate increase at the experiment. By tuning the quadrupole triplet and the field lens, the R_{34} term is kept significantly smaller at the position of the dipoles and at the same time, a decrease of the R_{33} term is achieved in the dipoles B8A and B8B. Losses are also avoided by keeping the R_{34} term smaller at Q23, compared to the other two optics modes. The R_{34} term is inevitably diverging towards the experiment, however by the simultaneously converging R_{33} term with a slope steeper than the v0 optics, the beam size, as will be verified by tracking simulations will be only slightly enlarged.

The behavior of the dispersive term in the two final optics configurations, apart

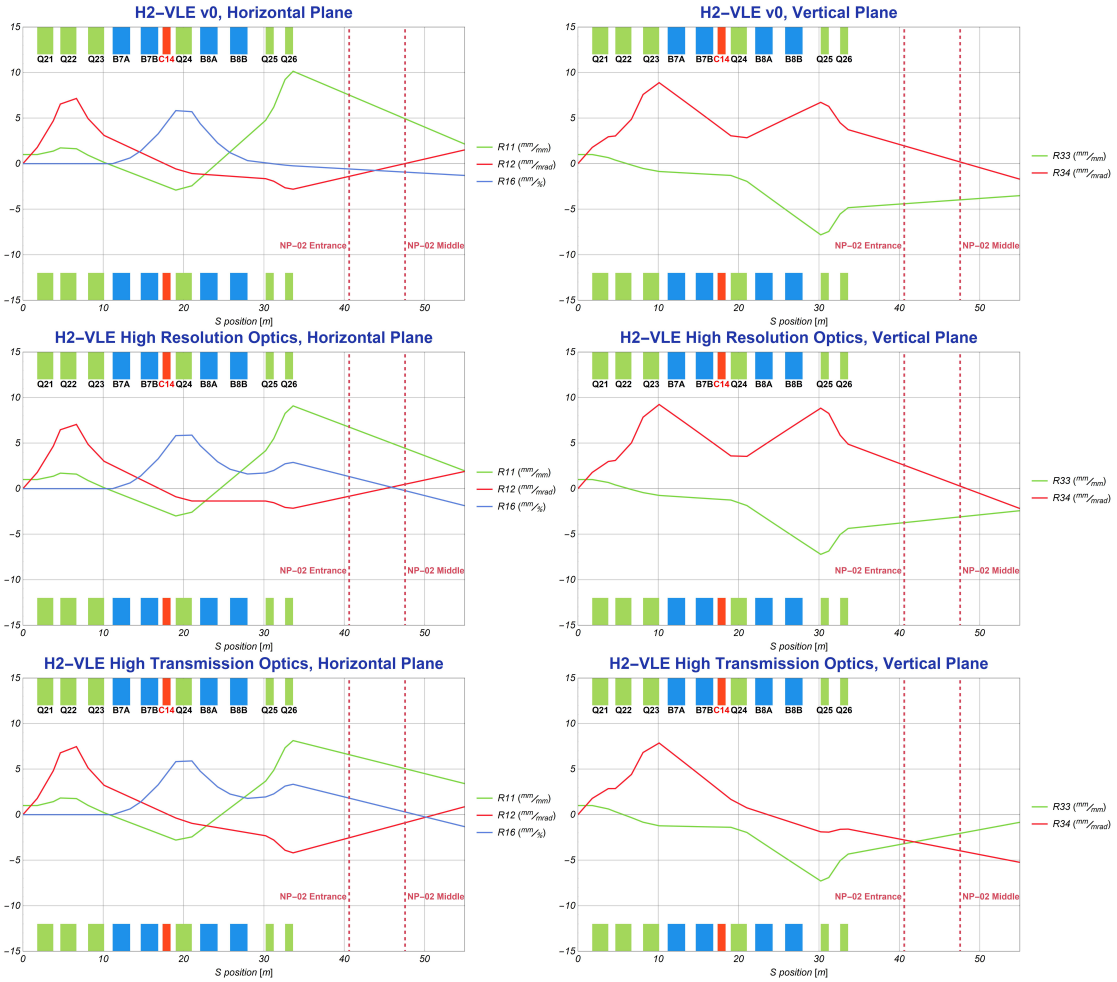

Figure 5.8: *H2-VLE final optics configurations. The initial optics, or v0, is shown for reasons of completeness.*

from contributing to the focusing of the beam at the experiment, can be useful in a measurement of the resolution of the spectrometer, constituting of a scintillator placed right before B8B and two scintillators placed after it (see Fig. 4.5).

Table 5.1 summarizes the integrated strength values for the three optics configurations of H2-VLE. A positive value indicates a focusing in the horizontal plane quadrupole, while a negative value a defocussing one.

5.3.4 Final optics configurations for H4-VLE

Similarly, Fig. 5.9 demonstrates the final optics configurations for the H4-VLE beamline, along with the initial optics configuration v0.

The 'High Resolution Optics' of H4-VLE was designed around two basic axes. Firstly, by converging the R_{33} term in the experiment, which, as was mentioned in Section 5.1, is considerably important compared to the R_{34} term, it was possible to compensate for the quickly diverging R_{36} term introduced by B20, which could not be avoided, since

Optics configurations for H2-VLE, 12 GeV/c				
	Integrated Strength [Tm/m]			
Quadrupole	v0 Optics	High Transmission Optics	High Resolution Optics	Maximum Value
Q21	-14.3	-16.01	-13.76	16.80
Q22	19.43	19.81	19.37	22.38
Q23	-11.64	-12.17	-11.47	16.80
Q24	15.74	14.41	14.57	16.80
Q25	-10.21	-10.41	-10.35	10.43
Q26	10.21	10.01	10.35	10.43

Table 5.1: *Quadrupole integrated strength values for the three optics configurations of H2-VLE for the design momentum of 12 GeV/c, along with their maximum values. The integrated strength is defined as gL, where g is the field gradient in T/m, and L is the quadrupole length in m. For lower momenta, the values are simply scaled down.*

there are no other magnetic elements afterwards. Secondly, a beam waist and a significant spot size decrease at the NP-04 entrance is achieved by steeply converging the R_{11} term.

The 'High Transmission Optics' has been developed to minimize the spot size at the dipole positions. The particle transmission is increased firstly by keeping the vertical magnification term significantly smaller at B18 and B19 compared to v0, and secondly by minimizing the R_{34} term at B19. Finally, a significant percentage of losses is avoided by adjusting the beam accordingly in B20. As explained in Section 5.2, the placement of the final dipole magnet with respect to the floor, or by $-57°$ with respect to the plotted $x' - y'$ reference system, indicates the control of the beam in the horizontal plane at this position. Therefore, the beam has been contained in the horizontal plane, by minimizing the R_{11} term as much as possible, which is the term contributing the most in the beam size.

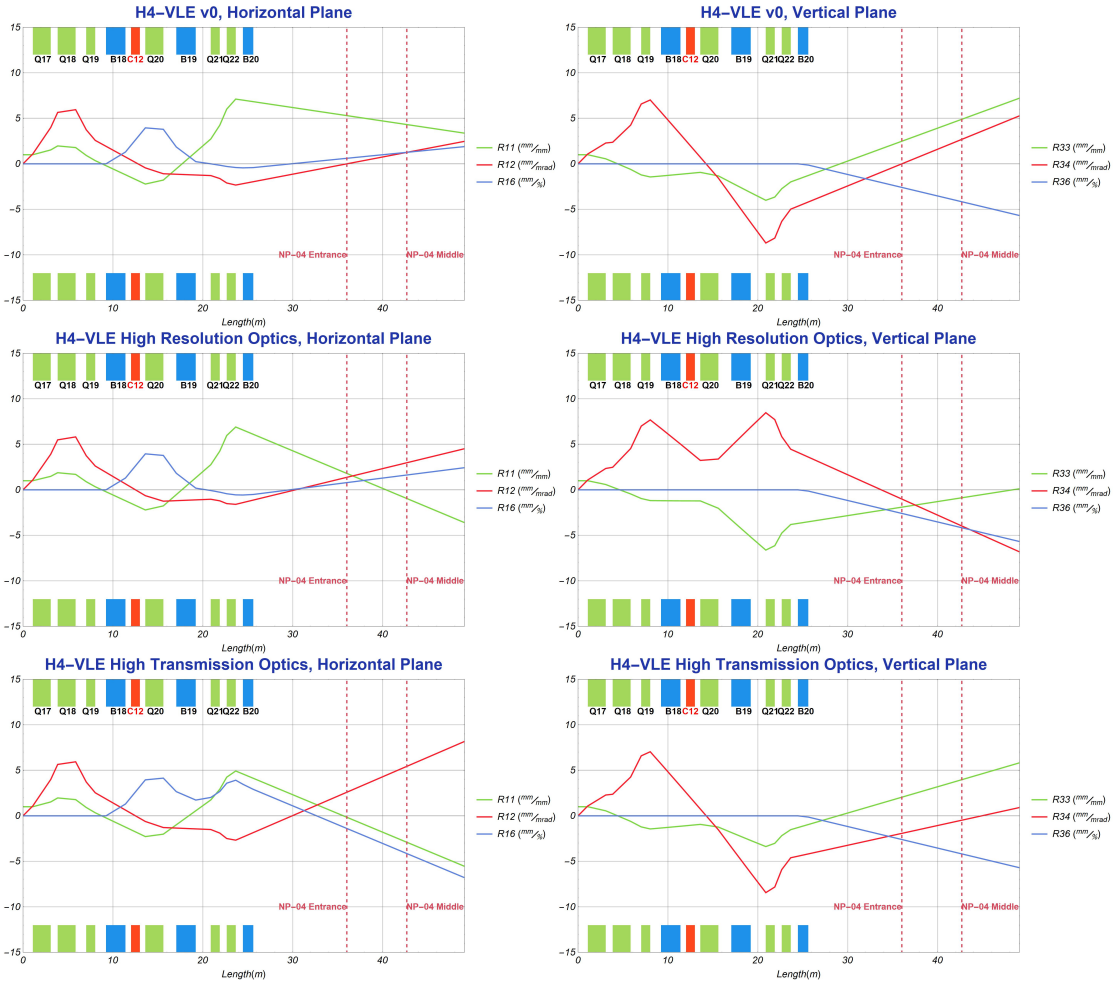

Figure 5.9: *H4-VLE final optics configurations. The initial optics, or v0, is shown for reasons of completeness.*

Optics configurations for H4-VLE, 7 GeV/c				
	Integrated Strength [Tm/m]			
Quadrupole	v0 Optics	High Transmission Optics	High Resolution Optics	Maximum Value
Q17	-11.37	-11.36	-10.46	16.80
Q18	14.48	14.52	14.07	16.80
Q19	-10.20	-10.20	-8.84	10.43
Q20	13.81	11.77	13.89	16.80
Q21	-9.91	-10.43	-9.38	10.43
Q22	8.39	10.43	9.24	10.43

Table 5.2: *Quadrupole integrated strength values for the three optics configurations of H4-VLE for the design momentum of 7 GeV/c, along with their maximum values. For lower momenta, the values are simply scaled down.*

CHAPTER 6

Tracking validation of the final optics configurations

In this chapter, tracking via PTC in a MAD-X environment of the particle distributions of Section 5.1 for the design momentum of each beamline will validate the final optics configurations. The consistency of the results for the 1 GeV/c nominal momentum will be demonstrated. In order to compare in parallel with the optics configurations of subsections 5.3.3 and 5.3.4, all results are presented in the tilted reference system of each beamline. Since BPROF4 is placed with respect to the floor of EHN1, the reader can find the expected beam profile at BPROF4 with respect to the straight reference system in Appendix B.

6.1 H2-VLE, nominal design momentum: +12 GeV/c

As described in Section 5.1, the distribution of π, K, p, and e generated from T22 by an impinging 80 GeV/c beam of 10^7 secondaries has been used as input in PTC to validate the final optics configurations. It should be noted that normally the integrated secondary beam intensity over a spill is expected to be 10^6 secondary particles, but an order of magnitude more has been used in order to increase the statistics. For the design momentum of 12 GeV/c, the corresponding distribution of 12 GeV/c $\pm 15\%$ is shown in Fig. 5.1. It is reminded that the initial selection of particles based on their momentum is completely unbiased taking into account the expected momentum acceptance as defined by the collimator maximum full gap and the R_{16} term at the collimator, and reduces the computing time considerably.

In order to visualize the H2-VLE beam in the three different optics configurations, in Fig. 6.1 the same 4000 "good" particles (particles that will reach the detector) have been tracked through the H2-VLE beamline for the three final optics configurations. The beam characteristics can be justified by comparing in parallel with the R-matrix elements shown in Fig. 5.8. Apparent is the significant vertical beam size decrease at the position of the dipoles obtained in 'High Transmission Optics' by the control of the R_{34} term , that will lead to a noteworthy rate increase. Additionally, in 'High Resolution Optics' the vertical beam waist is now more evident, as expected by the steeper R_{33} slope compared to v0 optics and the simultaneous R_{34} nullification.

Table 6.1 shows the transmission and acceptance for the three different optics modes

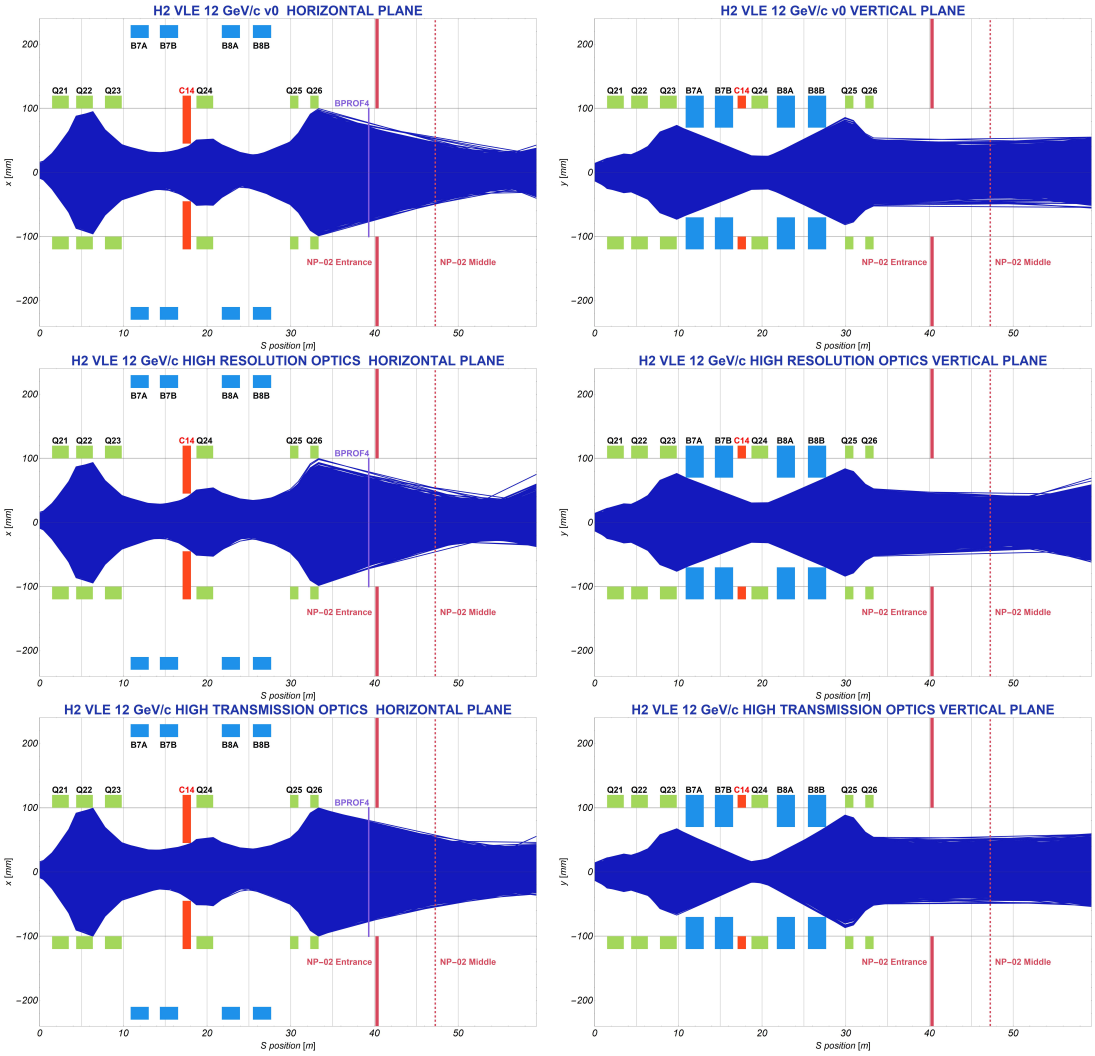

Figure 6.1: *Tracking via PTC of the same 4000 "good" particles of H2-VLE for the three final optics modes, plotted in the tilted reference system.*

obtained via PTC for 10^7 secondaries. It can be seen that 'High Transmission Optics' provides an $\sim$11% rate increase with respect to v0 Optics, while'High Resolution Optics' comes with a rate expense of $\sim$6%. Assuming an integrated intensity of 10^6 particles impinging on T22 homogeneously distributed per spill (4.8 s), the calculated expected rate at the NP-02 detector is $\sim$500 Hz, which is above its maximum acquisition rate of the detector ($\sim$100 Hz). The calculated rate by PTC neglects pion and kaon decays as well as particle interactions, and therefore is not considered very accurate, however independent G4BeamLine simulations [23] indicated that the expected rate for the 12 GeV/c H2-VLE beam is approximately 400 Hz, still well above the maximum acquisition rate. The provided rate increase, while indifferent for the design momentum, will become quite significant in the momentum of 1 GeV/c where the expected rate is much lower than the maximum acquisition rate of the electronics.

Transmission and acceptance for H2-VLE, 12 GeV/c			
	v0 Optics	High Transmission Optics	High Resolution Optics
	Transmission (out of 10^7 secondaries)		
	23146	25691	21733
	Acceptance		
μ_x (mm)	0.62	0.75	0.7
σ_x (mm)	3.32	3.38	3.36
μ'_x (mrad)	-0.83	-0.33	-0.57
σ'_x (mrad)	6.59	6.35	6.86
μ_y (mm)	-0.56	-0.52	-0.57
σ_y (mm)	3.73	3.69	3.81
μ'_y (mrad)	-0.13	0.01	-0.16
σ'_y (mrad)	4.49	5.27	4.22
$\mu_{\delta p/p}$ (%)	-0.75	-0.23	-0.63
$\sigma_{\delta p/p}$ (%)	4.67	4.29	4.4

Table 6.1: *Transmission and acceptance for the three final optics configurations of H2-VLE, for the design momentum of 12 GeV/c.*

Table 6.2 illustrates the spot sizes at BPROF4 (the final profile detector of the beamline, also visible in Fig. 6.1) and at the NP-02 middle. It is shown that in 'High Resolution Optics' the beam size RMS is reduced by ∼2-3 mm in both planes, while in 'High Transmission Optics' the beam size RMS is larger by ∼3-4 mm.

Spot sizes at BPROF4 and NP-02 middle for H2-VLE, 12 GeV/c			
	v0 Optics	High Transmission Optics	High Resolution Optics
	BPROF4 profile		
μ_x (mm)	2.23	1.35	0.28
σ_x (mm)	35.29	36.73	33.4
μ_y (mm)	1.42	1.39	1.14
σ_y (mm)	19.26	18.86	17.59
	NP-02 middle profile		
μ_x (mm)	1.29	1.52	1.16
σ_x (mm)	19.81	23.49	17.96
μ_y (mm)	1.27	0.84	1.03
σ_y (mm)	17.5	20.18	14.57

Table 6.2: *Spot sizes at BPROF4 and the NP-02 middle for the three final optics configurations of H2-VLE for the design momentum of 12 GeV/c.*

Table 6.3 shows the composition of the aforementioned generated distribution, as

well as the composition of the transmitted beam reaching the NP-02 detector.

Composition for H2-VLE, 12 GeV/c					
	Total (#)	p (%)	e (%)	π (%)	K (%)
Composition of initial distribution	735942	14.9	1.4	74.1	9.6
High Transmission Optics (without decays)	25691	12.1	8.4	70.6	9.0
High Transmission Optics (with decays)	23816	13.0	9.1	71.7	6.2

Table 6.3: *Composition of 12 GeV/c ±15% π, K, p, and e generated from T22 by an impinging 80 GeV/c beam of 10^7 secondaries, as well as that of the transmitted beam reaching the NP-02 cryostat.*

The generated particles within the specified momentum region are mostly pions and secondly protons, while kaons are only a fraction of 9.6%. The composition of the transmitted particles is mildly altered, and specifically the positron fraction has shifted from 1.4% in the initial distribution to 8.4% in the transmitted beam. This can be understood if the initial positron distribution is compared to, for example, the dominating pion distribution, as is shown in Fig. 6.2, where the two distributions have been normalized to unity. Both the spatial and the angular pion distributions are much more spread out, having an approximately double RMS compared to the positron distribution.

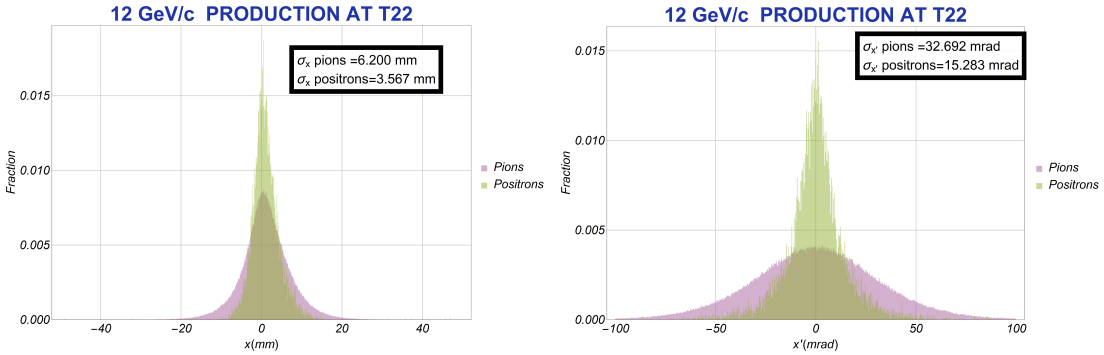

(a) **(b)**

Figure 6.2: *Comparison of the positron and pion 12 GeV/c ±15% spatial and angular distributions generated at T22, normalized to unity. The pion and positron momentum distributions (not shown) are almost identical.*

Since particles having large spatial and angular offsets will be cut by the magnetic apertures, this spread defines the transmitted composition, and specifically, while 21% of the generated positrons reach the cryostat, the corresponding fraction for the pions is only 3%. The pion, kaon and proton distributions are quite similar, and therefore the ∼3% transmission observed for the pions is consistent for the protons and kaons as well. The composition of the transmitted beam shows no significant differences for the other two optics modes.

Finally, to account for the decays of pions and kaons, the simple exponential decay formula also plotted in 4.2 has been used for a distance of 40 m (until the entrance of the detector). Shown again in Table 6.3 are the obtained results, indicating a 3% drop of the final kaon content.

Table 6.4 shows the percentage of transmitted particles through H2-VLE for 'High Transmission Optics' and v0 Optics, indicating the magnetic elements that mostly contribute to the losses. Since the initial spatial and angular distributions are quite spread out, a significant percentage of particles will be absorbed by the aperture of the first quadrupole, denoted Q21 and specifically, only ∼34% of the generated particles are transmitted through Q21. Through a better control of the R_{34} term at Q22 and Q23 (see Fig. 5.8), High Transmission Optics transmits ∼7% more particles to Q23. This particle increase is retained until B8B by controlling the vertical beam size, resulting in a ∼17% rate increase at B8B. Taking into account losses at Q25 and Q26 due to a large R_{12}, combined with a residual R_{16} term, the observed rate increase at NP-02 is ∼11% in' High Transmission Optics'.

Percentage of transmitted particles through the magnetic elements of H2-VLE, 12 GeV/c									
	Q21	Q22	Q23	B7B	C14	Q24	B8B	Q25	Q26
v0 Optics	34.4	16.0	10.8	8.7	5.6	5.6	4.7	3.7	3.1
High Trans.	34.4	16.6	11.6	9.5	6.1	6.1	5.5	4.2	3.5

Table 6.4: *Percentage of transmitted particles for H2-VLE 12 GeV/c nominal momentum*

The beam size behavior can become more clear if the beam size RMS with respect to the longitudinal distance is plotted for the acceptance of each optics mode, as is shown in Fig. 6.3. In the horizontal plane, the beam waist in 'High Resolution Optics' has shifted upstream closer to the NP-02 middle where the focus is aimed, and simultaneously there is a mild beam size decrease of ∼2 mm at this position. In the vertical plane the beam waist in more evident, having a ∼3 mm decrease compared to v0 optics. The diverging R_{34} term of 'High Transmission Optics' contributes to the vertical beam size at the experiment, but this becomes significant only after the middle of the cryostat.

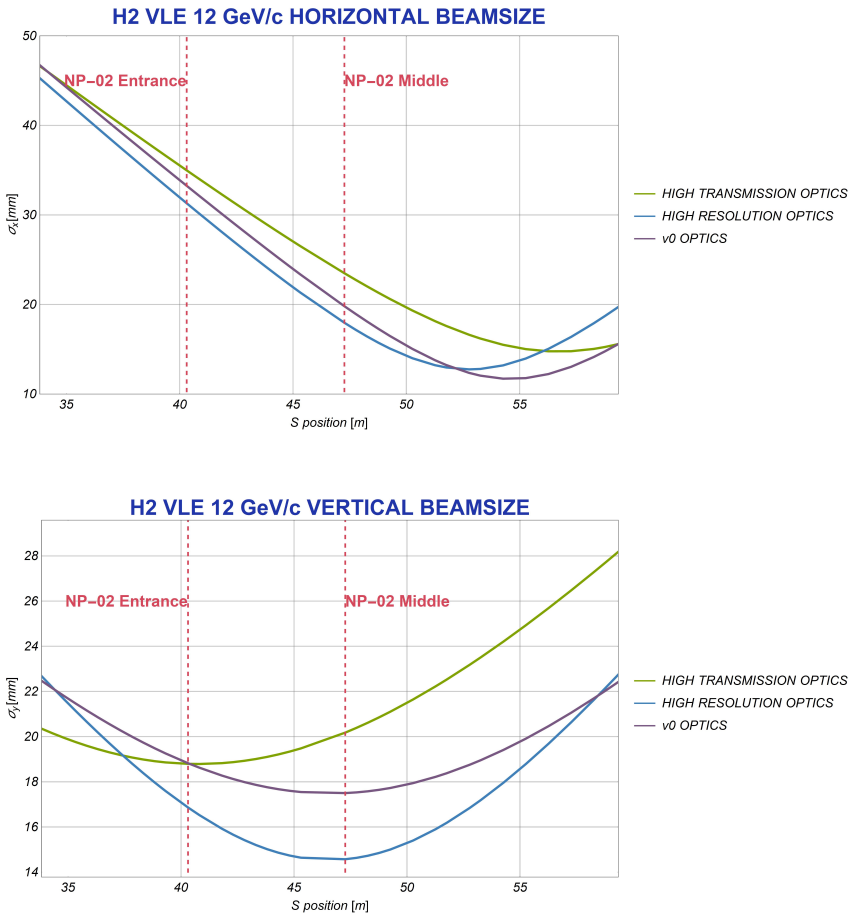

Figure 6.3: *Horizontal and vertical beam size RMS for the three optics configurations of H2-VLE, for the design momentum of 12 GeV/c*

6.2 H2-VLE, 1 GeV/c

The consistency of the results in the 1 GeV/c nominal momentum will be briefly presented and, following the same method as in the 12 GeV/c case, particles of 1 GeV/c $\pm 15\%$ have been selected over the entire spectrum of production using the G4BeamLine software, the distribution of which is plotted in Fig. 6.4.

Compared to Fig. 5.1, it is clear how much broader the distributions are in the 1 GeV/c momentum region, and specifically the spatial and angular RMS are ~7-8 times larger. While the longitudinal momentum distribution resembles that of the 12 GeV/c region, the momentum distribution is remarkably different, having a preference towards positive momentum offsets.

The correlation between the various coordinates is demonstrated in Fig. 6.5 and can be compared to Fig. 5.3. In Fig. 5.3d the particles are generated with relatively small angular offsets, and therefore the $\Delta p_z - \Delta p$ phase space lies within the $\Delta p = \Delta p_z$ line or slightly above it (corresponding to particles having transverse momentum components), while in Fig. 6.5d the entire $\Delta p > \Delta p_z$ is occupied, indicating large transverse

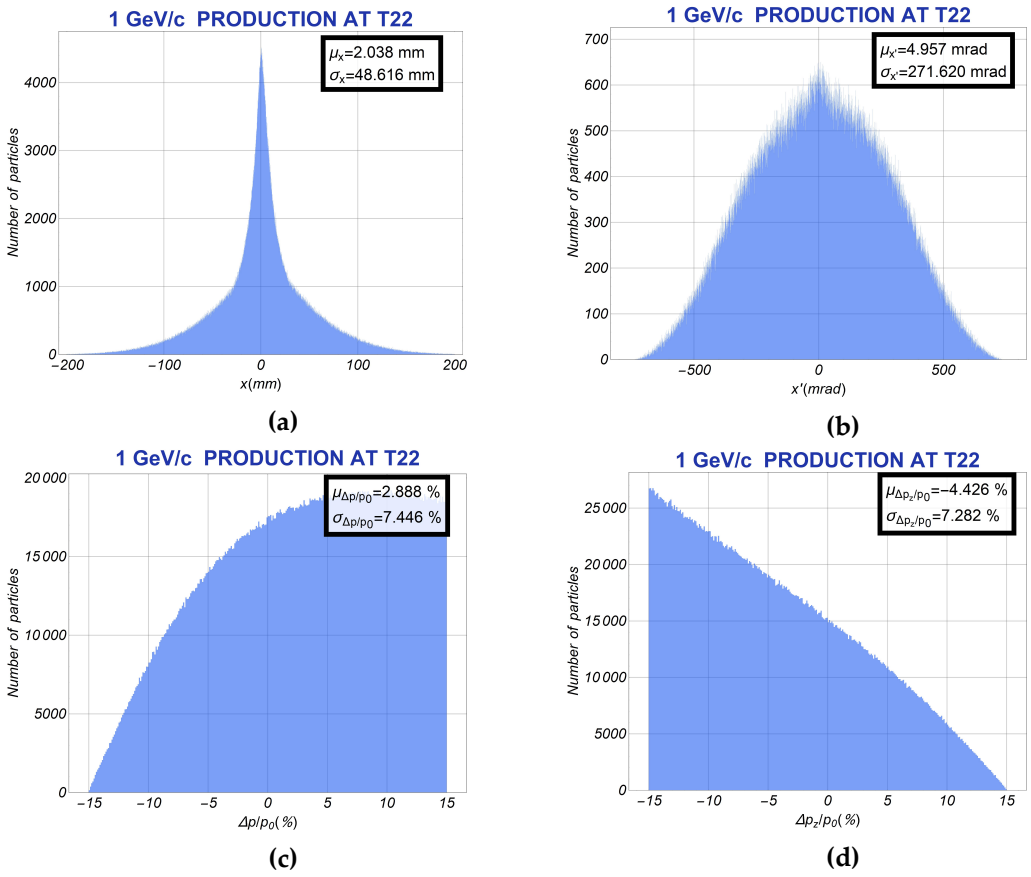

Figure 6.4: $1\,GeV/c \pm 15\%$ π, p, K, e *production at T22.*

momentum components. Fig. 6.5c reflects the fact that particles having large transverse momenta will also have larger momenta, a property mildly present in Fig. 5.3c.

The results of the PTC tracking are shown in Table 6.5. 'High Transmission Optics' provides a ∼12% rate increase compared to v0 Optics. The spatial acceptance is slightly larger by ∼1 mm for all optics configurations. This can be explained by the fact that in the 12 GeV/c region, particles with spatial offsets of for example 20 mm, will necessarily have x' offsets of more than 20mm (Fig. 5.3a). In the much more spread out $1\,GeV/c \pm 15\%$ phase space of Fig. 6.5a, particles with 20 mm but small x' offsets can be generated, which can be transmitted through the beamline. The spot size at BPROF4 and the middle of NP-02 is almost identical with the 12 GeV/c case, apart from a slight beam size increase of ∼1 mm due to the larger spatial acceptance.

It is interesting to examine the composition of the generated distribution at T22 shown in Table 6.6. As already mentioned, for 10^7 secondaries of 80 GeV/c impinging on T22, the particles generated with a momentum in the range of [0.85,1.15] GeV/c are two orders of magnitude more than those in the range of [10.2,13.8] GeV/c. However, the total number of particles reaching the detector is one order of magnitude less in the 1 GeV/c region compared to the 12 GeV/c region, expected by the broader initial

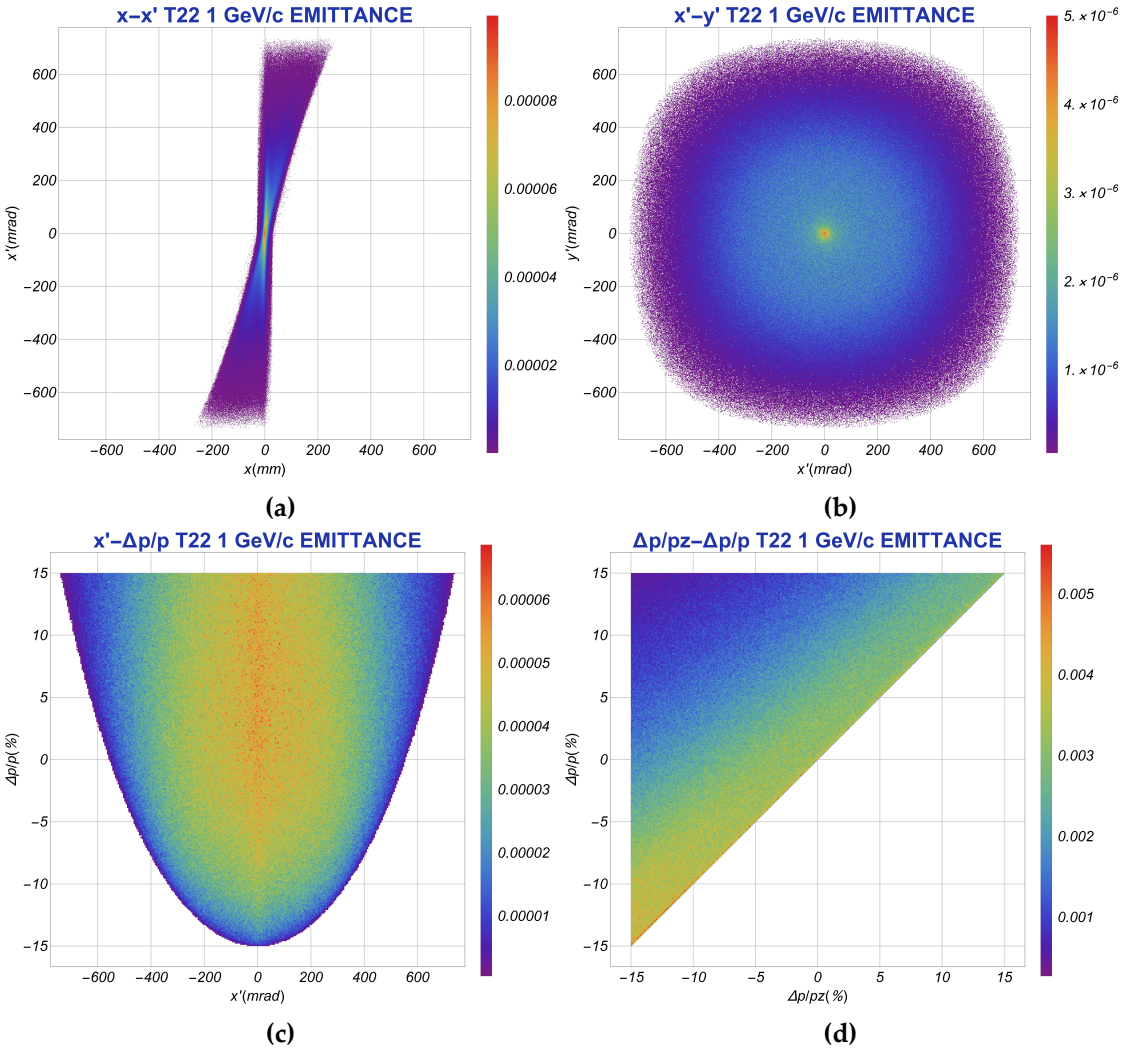

Figure 6.5: *Correlations between (a) x-x', (b) x'-y', (c) x'-$\Delta p/p$ and (d) x'-$\Delta p_z/p$ coordinates of the $1\,GeV/c$ ±15% emittance at T22.*

distributions, and specifically the calculated particle rate at the NP-02 detector is only $\sim$50 Hz, making the $\sim$12% rate increase provided by the 'High Transmission Optics' quite vital.

Moreover, the production is now dominated by both protons and pions, while kaons are only a fraction of 3.5%. The composition of transmitted particles (without taking into account the decays) is significantly altered, and particularly it is dominated by positrons by 66.5%, the generated positrons being a small fraction of only 1.2% of the initial distribution. Again, this becomes clear once the positron and pion distributions are plotted separately, as in Fig. 6.6, indicating the sharper positron distribution. Taking into account the decays by using the exponential law for a 40 m distance until the entrance of the NP-02 detector, no kaons are expected to reach the detector in the 1 GeV/c case.

Transmission and acceptance for H2-VLE, 1 GeV/c			
	v0 Optics	High Transmission Optics	High Resolution Optics
	Transmission (out of 10^7 secondaries)		
	2215	2489	2108
	Acceptance		
μ_x (mm)	0.67	0.78	0.77
σ_x (mm)	4.16	4.31	4.22
μ'_x (mrad)	-0.75	-0.43	-0.51
σ'_x (mrad)	6.66	6.38	6.95
μ_y (mm)	-0.46	-0.42	-0.58
σ_y (mm)	4.53	4.25	4.85
μ'_y (mrad)	-0.21	-0.18	-0.29
σ'_y (mrad)	4.43	5.14	4.19
$\mu_{\delta p/p}$ (%)	-0.9	-0.31	-0.83
$\sigma_{\delta p/p}$ (%)	4.78	4.42	4.49

Table 6.5: *Transmission and acceptance of H2-VLE, 1 GeV/c.*

Composition for H2-VLE, 1 GeV/c					
	Total (#)	p (%)	e (%)	π (%)	K (%)
Composition	4368578	54.5	1.2	40.9	3.5
High Transmission Optics (without decays)	2489	13.3	66.5	18.8	1.4
High Transmission Optics (with decays)	2216	15.0	74.7	10.3	0.0

Table 6.6: *Composition of* $1\ GeV/c \pm 15\%$ π, K, p, *and* e *generated from T22 by an impinging 80 GeV/c beam of* 10^7 *secondaries.*

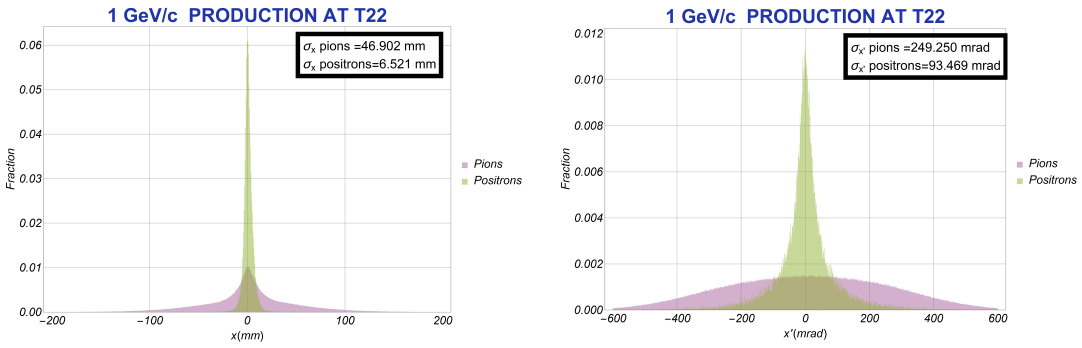

(a) **(b)**

Figure 6.6: *Comparison of the positron and pion* $1\ GeV/c \pm 15\%$ *spatial and angular distributions generated at T22, normalized to unity.*

6.3 H4-VLE, nominal design momentum: + 7 GeV/c

The distribution of particles generated at T24 having the design momentum of H4-VLE (7 GeV/c ±15%), shown in Fig. 5.2, has been used to validate the chosen optics configurations for H4-VLE.

In Fig. 6.7 tracking of the same 4000 "good" particles is visualized. Comparing in parallel with the R-matrix elements shown in Fig. 5.9, there is a slight vertical beam size decrease at B19 in 'High Transmission Optics' as well as a significant horizontal beam size decrease at B20, both accounting for the observed rate increase. It can be seen that a horizontal beam waist is achieved at the detector entrance both in 'High Resolution' and in 'High Transmission Optics' compared to v0, while the vertical plane seems similar towards the experiment in all optics configurations.

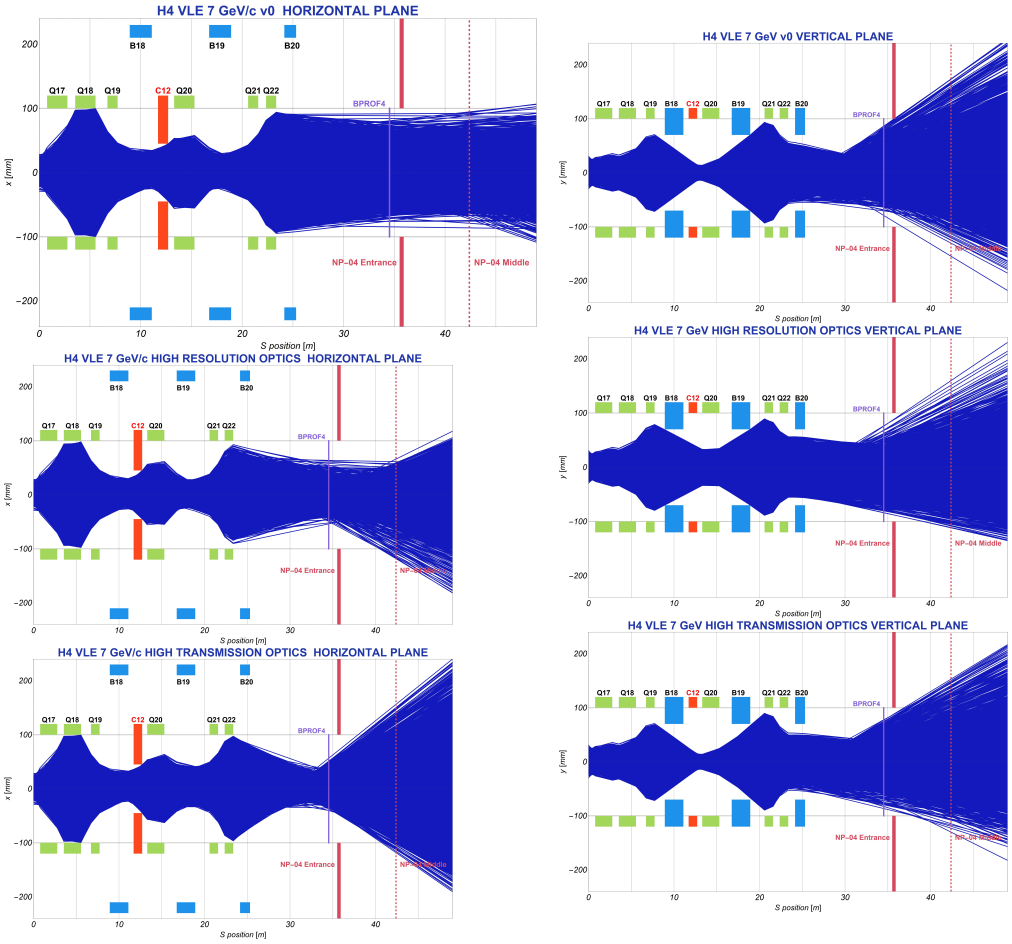

Figure 6.7: *Tracking via PTC of the same 4000 "good" particles of H4-VLE for the three final optics modes, plotted in the x'-y' reference system.*

Table 6.7 illustrates the transmission and acceptance for the three final optics configurations obtained via PTC. 'High Transmission Optics' provides a ∼13% rate increase compared to v0, while 'High Resolution Optics' comes without any rate expense. Similar to H2-VLE, the provided rate increase is not important for the NP-04 experiment,

since it is well above the maximum data acquisition rate of the detector. The independent G4BeamLine study indicates a $\sim$300 Hz expected rate.

Transmission and acceptance for H4-VLE, 7 GeV/c			
	v0 Optics	High Transmission Optics	High Resolution Optics
	Transmission (out of 10^7 secondaries)		
	18626	20986	18718
	Acceptance		
μ_x (mm)	-0.32	0.14	-0.6
σ_x (mm)	7.83	8.01	7.5
μ'_x (mrad)	0.06	0.66	-0.29
σ'_x (mrad)	7.35	7.78	8.18
μ_y (mm)	-0.9	-0.7	-1.14
σ_y (mm)	8.89	9.42	9.58
μ'_y (mrad)	0.01	0.1	-0.44
σ'_y (mrad)	5.55	5.48	5.76
$\mu_{\delta p/p}$ (%)	1.92	1.37	-0.41
$\sigma_{\delta p/p}$ (%)	6.2	5.64	6.63

Table 6.7: *Transmission and acceptance for the three final optics configurations of H4-VLE, for the design momentum of 7 GeV/c.*

Table 6.8 shows the spot sizes at BPROF4 and at the NP-04 entrance, where the focus is aimed. Both 'High Transmission' and 'High Resolution' optics provide a significant spot size decrease in the horizontal plane compared to v0 optics, and specifically there is a $\sim$16 mm spot size reduction in 'High Resolution Optics', and a $\sim$13 mm reduction in 'High Transmission Optics'. The vertical plane shows no considerable reduction.

In Table 6.9 the composition of the 7 GeV/c $\pm$15% initial distribution is shown, as well as the composition of the beam reaching the NP-04 detector. Similar to the 12 GeV/c $\pm$15% production at T22, the generated particles are mostly pions and secondly protons, the kaons being only a fraction of $\sim$9.3%. The positron fraction has shifted from 2.2% in the generated composition to 19.6% in the transmitted beam, again defined by the significantly sharper initial positron distribution.

Table 6.10 indicates the particle transmission through H4-VLE for 'High Transmission Optics' and v0 Optics. Since the 7 GeV/c distribution is broader than the 12 GeV/c, a fraction of only $\sim$23% of the generated particles are transmitted through the first quadrupole, denoted Q17 (compared to the corresponding 34% at Q21 of H2-VLE), while only $\sim$9% is transmitted through the second quadrupole, Q18 (in comparison with the corresponding 16% at Q22 of H2-VLE). The currents of the quadrupole triplet are almost identical for the two optics modes, leading to a similar particle transmission until Q19. A $\sim$5% rate increase in 'High Transmission Optics' is achieved at B19 by a decrease of the R_{33} term at this position. This particle rate increase is retained until Q22,

Spot sizes at BPROF4 and NP-04 entrance for H4-VLE, 7 GeV/c			
	v0 Optics	High Transmission Optics	High Resolution Optics
	BPROF4 profile		
μ_x (mm)	2.31	1.61	-2.61
σ_x (mm)	34.28	15.92	17.83
μ_y (mm)	-4.96	-4.33	2.82
σ_y (mm)	28.49	30.03	28.17
	NP-04 entrance profile		
μ_x (mm)	2.1	1.42	-3.05
σ_x (mm)	33.16	20.02	17.5
μ_y (mm)	-6.5	-5.59	3.2
σ_y (mm)	30.03	31.82	29.57

Table 6.8: *Spot sizes at BPROF4 and the NP-04 entrance for the three final optics configurations of H4-VLE, for the design momentum of 7 GeV/c.*

Composition for H4-VLE, 7 GeV/c					
	Total (#)	p (%)	e (%)	π (%)	K (%)
Composition	1168920	16.2	2.2	72.2	9.3
High Transmission Optics (without decays)	20986	10.3	19.6	62.6	7.5
High Transmission Optics (with decays)	19048	11.3	21.6	62.9	4.2

Table 6.9: *Composition of 7 GeV/$c\pm$15% π, K, p, and e generated from T24 by an impinging 80 GeV/c beam of 10^7 secondaries, as well as that of the transmitted beam reaching the NP-04 cryostat.*

and, by better controlling the beam envelope in the horizontal plane to adjust to the B20 aperture, placed with respect to the EHN1 floor, ∼12% more particles are transmitted at B20. Due to the spread out v0 optics beam, additional losses at the NP-04 entrance aperture, leading to the observed rate increase of 'High Transmission Optics', ∼13% compared to v0 Optics.

Percentage of transmitted particles through the magnetic elements of H4-VLE, 7 GeV/c											
	Q17	Q18	Q19	B18	C12	Q20	B19	Q21	Q22	B20	NP-04
v0 Optics	22.6	9.2	6.7	6.1	4.3	4.2	2.8	2.3	1.8	1.6	1.6
High Trans.	22.6	9.2	6.7	6.1	4.3	4.2	3.0	2.4	2.0	1.8	1.8

Table 6.10: *Particle transmission in % for H4-VLE 7 GeV/c nominal momentum.*

Fig. 6.8 shows the beam size RMS with respect to the longitudinal distance. While

there was no horizontal beam waist in v0 Optics, there is an evident waist at the NP-04 entrance in 'High Resolution Optics'. In 'High Transmission Optics', the waist is upstream from the NP-04 entrance, but the beam is quickly diverging due to the behavior of the R_{11}, R_{12} and R_{16} terms in Fig. 5.9. In the vertical plane the three optics modes behave quite similarly, with the difference that in 'High Resolution Optics' the beam is diverging more gradually, due to a better control of the R_{33} term.

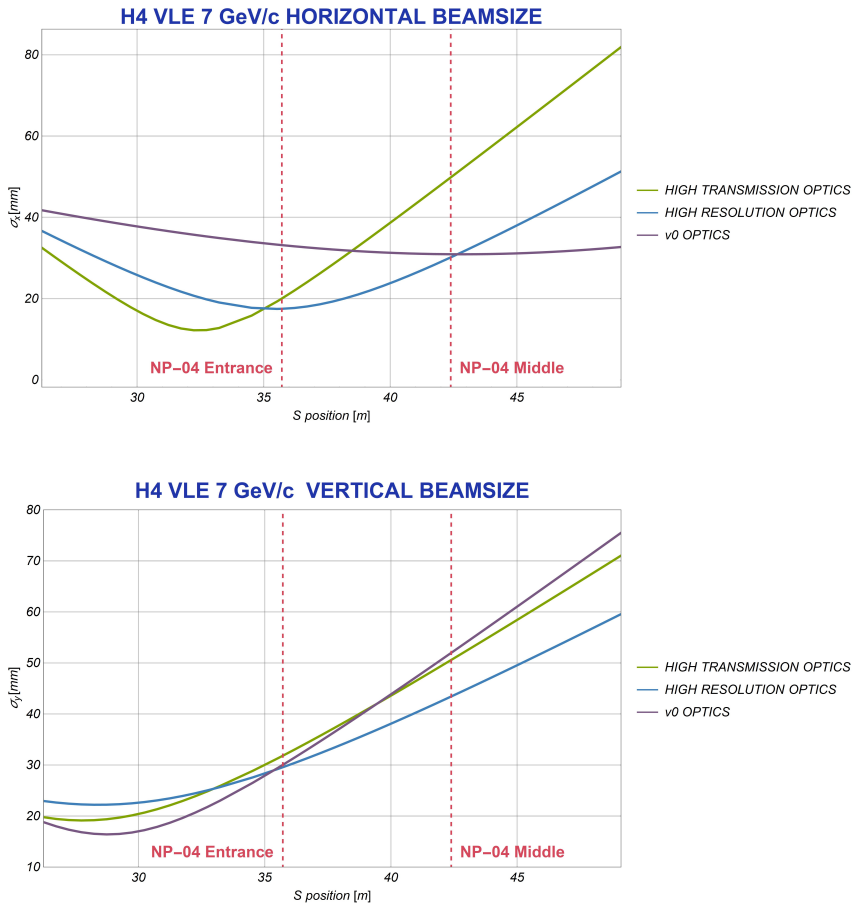

Figure 6.8: *Horizontal and vertical beam size RMS for the three optics configurations of H4-VLE, for the design momentum of 7 GeV/c*

6.4 H4-VLE, 1 GeV/c

Particles of 1 GeV/c $\pm 15\%$ have been selected over the entire spectrum of production at T24 and tracked along H4-VLE, to confirm the validity of the aforementioned results in the low momentum region. The generated distribution is almost identical to the corresponding 1 GeV/c $\pm 15\%$ distribution at T22, shown in Figs. 6.4 and 6.5.

The results of the PTC tracking are shown in Table 6.11, where it can be seen that 'High Transmission Optics' provides a $\sim 14\%$ rate increase compared to v0 Optics. Again, assuming a integrated intensity of 10^7 secondaries impinging on T24, the calculated rate is only ~ 50 Hz, therefore a rate increase is quite crucial for the experiment.

Transmission and acceptance for H4-VLE, 1 GeV/c			
	v0 Optics	High Transmission Optics	High Resolution Optics
	Transmission		
	2947	2944	3376
	Acceptance		
μ_x (mm)	-0.03	0.47	-0.67
σ_x (mm)	8.32	8.55	8.28
μ'_x (mrad)	0.01	0.53	-0.3
σ'_x (mrad)	7.6	8.04	8.33
μ_y (mm)	-0.58	-0.4	-1.09
σ_y (mm)	9.26	9.72	10.04
μ'_y (mrad)	-0.12	0	-0.4
σ'_y (mrad)	5.62	5.5	5.86
$\mu_{\delta p/p}$ (%)	1.57	1.06	-0.81
$\sigma_{\delta p/p}$ (%)	6.34	5.76	6.85

Table 6.11: *Transmission and acceptance for the three final optics configurations of H4-VLE, for the nominal momentum of 1 GeV/c.*

The composition of the particles produced at T24 in the 1 GeV/c $\pm 15\%$ as well as that of the transmitted beam is almost identical to the H2-VLE 1 GeV/c $\pm 15\%$ case, and therefore is not shown.

The spot sizes at BPROF4 and at the entrance of NP-04 show a slight increase of 1 mm compared to the 7 GeV/c case due the slightly larger spatial and angular acceptance, and are not shown.

6.5 Comparison of PTC with G4BeamLine simulation

Figs. 6.9 and 6.10 illustrate the good particles profiles at the four profile monitors of H2-VLE for 12 GeV/c nominal momentum, as obtained in the aforementioned PTC analysis for 10^7 secondaries impinging on T22 (left). In parallel, they are compared to the independent Monte Carlo simulation with G4BeamLine that has been discussed in Section 5.1, where the H2-VLE geometry has been precisely modeled, for the same number of secondaries (right). Although BPROF4 is placed with respect to the ground, all profiles are with respect to the tilted reference system, to be directly comparable with the G4BeamLine simulation.

The extent of the histograms ([-100,100]) corresponds to that of the proposed profile monitors, as will be discussed in Chapter 8, allowing for a direct comparison with the profiles that will be obtained in the real H2-VLE beam.

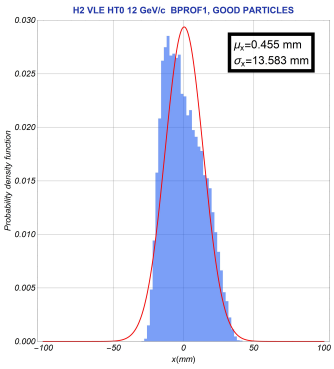

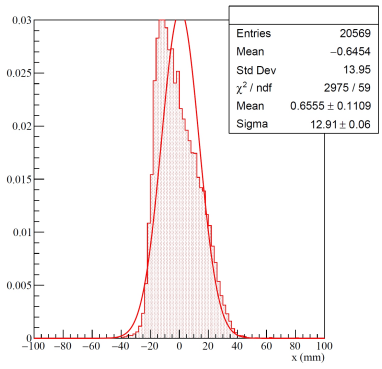

(a) *BPROF1, Horizontal*

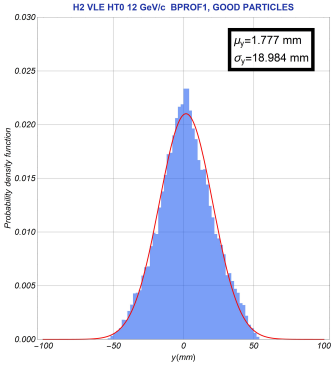

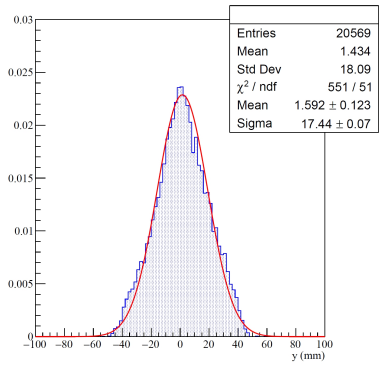

(b) *BPROF1, Vertical*

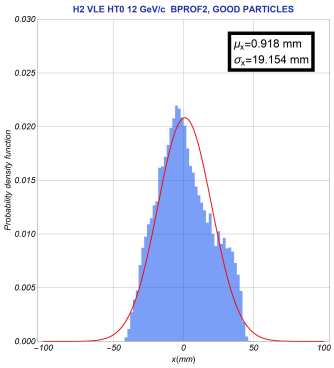

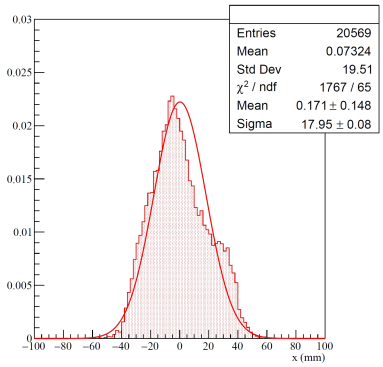

(c) *BPROF2, Horizontal*

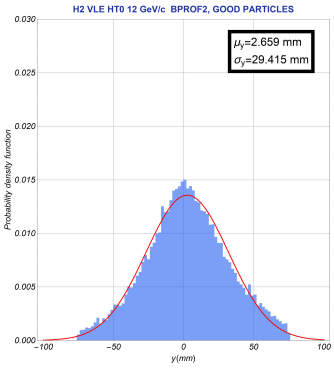

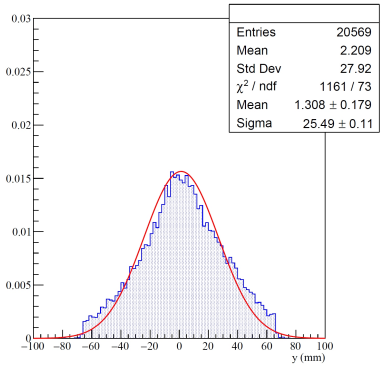

(d) *BPROF2, Vertical*

Figure 6.9: *H2-VLE 12 GeV/c good particles profiles in PTC (left) and G4BeamLine (right).*

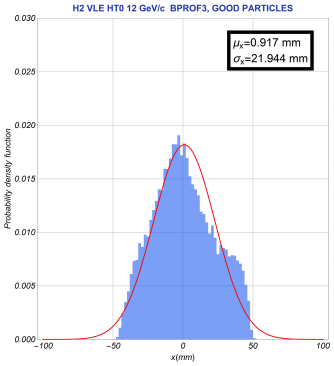

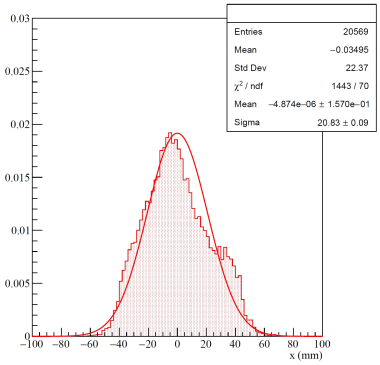

(a) *BPROF3, Horizontal*

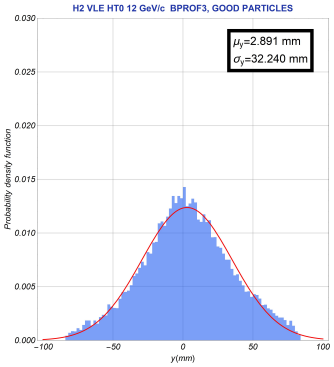

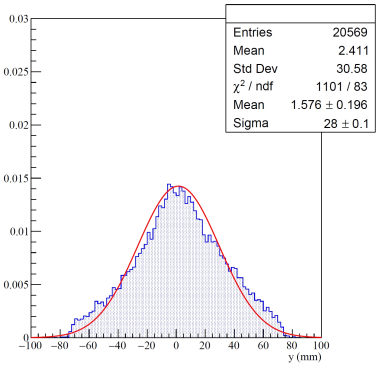

(b) *BPROF3, Vertical*

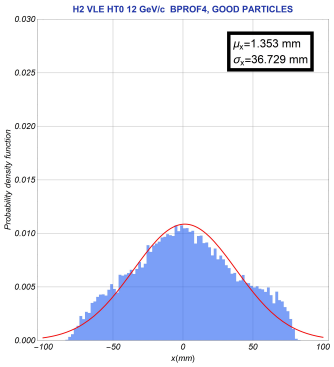

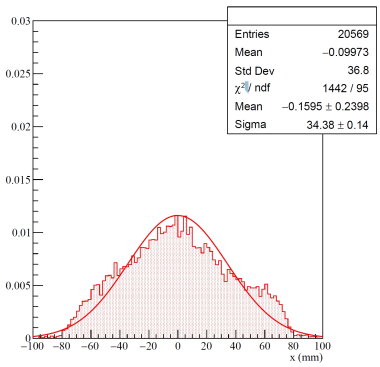

(c) *BPROF4, Horizontal*

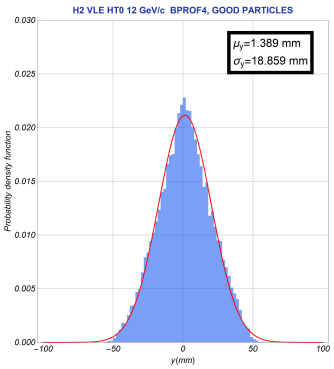

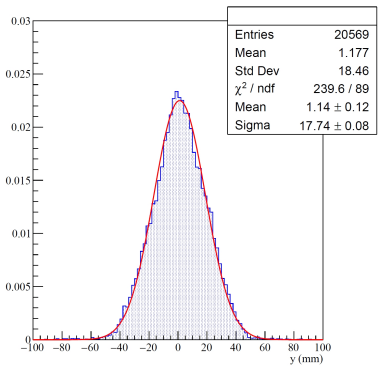

(d) *BPROF4, Vertical*

Figure 6.10: *H2-VLE 12 GeV/c good particles profiles in PTC (left) and G4BeamLine (right).*

For 12 GeV/c nominal momentum, the rate increase in 'High Transmission Optics' with respect to V0 optics obtained in G4BeamLine is 11%, identical to PTC. However, as will be justified below, the particle transmission is $\sim$26000 particles in PTC, while in G4BeamLine it is only $\sim$21000. Since the number of entries is different for PTC and G4BeamLine, the histograms represent the probability density functions. In both PTC and G4BeamLine results, a Gaussian distribution with unit area has been fitted.

The beam characteristics of Figs. 6.9 and 6.10 are summarized in Table 6.12, where the results obtained in v0 optics in the two approaches are shown as well. The mean and RMS shown are those of the actual distributions, and not of the fitted Gaussians.

H2-VLE 12 GeV/c, Good particles profiles								
	v0 Optics				**High Transmission Optics**			
	$\mu_x(mm)$	$\sigma_x(mm)$	$\mu_y(mm)$	$\sigma_y(mm)$	$\mu_x(mm)$	$\sigma_x(mm)$	$\mu_y(mm)$	$\sigma_y(mm)$
	BPROF1							
G4BL	-0.23	12.24	1.13	21.46	-0.65	13.95	1.43	18.09
PTC	0.50	11.81	1.34	23.63	0.46	13.58	1.78	18.98
	BPROF2							
G4BL	1.33	18.98	1.80	31.14	0.07	19.51	2.21	27.92
PTC	1.78	18.63	2.16	33.99	0.92	19.15	2.66	29.41
	BPROF3							
G4BL	1.27	22.08	1.97	33.70	-0.03	22.37	2.41	30.58
PTC	1.84	21.67	2.37	36.75	0.92	21.94	2.89	32.24
	BPROF4							
G4BL	1.30	35.49	1.15	19.40	-0.10	36.80	1.18	18.46
PTC	2.23	35.29	1.42	19.26	1.35	36.73	1.39	18.86

Table 6.12: *Comparison between the good particles distributions at the four profile monitors of H2-VLE for a nominal momentum of 12 GeV/c, as obtained in the PTC simulations, and independent G4BeamLine simulations. All profiles are with respect to the tilted reference system.*

The same method has been followed for H4-VLE, and the results obtained for 7 GeV/c nominal momentum are illustrated in Figs. 6.11 and 6.12. The profiles at BPROF1, BPROF2 and BPROF3 are with respect to the tilted reference system, while these of BPROF4 with respect to the ground.

The rate increase in 'High Transmission Optics' with respect to v0 optics is $\sim$12% in G4BeamLine, in good agreement with the $\sim$13% rate increase obtained via PTC. Similarly to H2-VLE, the transmission in PTC for the same number of secondaries is higher than in G4BeamLine, and in particular, PTC yields $\sim$21000 good particles, while G4BeamLine $\sim$16000.

Table 6.13 summarizes the results of Figs. 6.11 and 6.12, showing the results for v0 Optics as well.

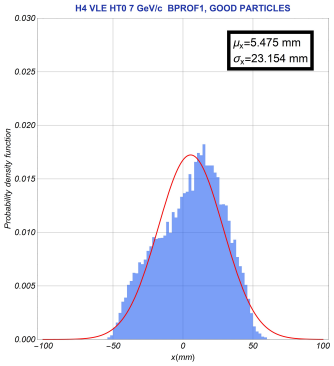

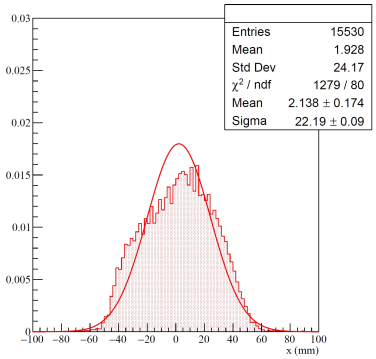

(a) *BPROF1, Horizontal*

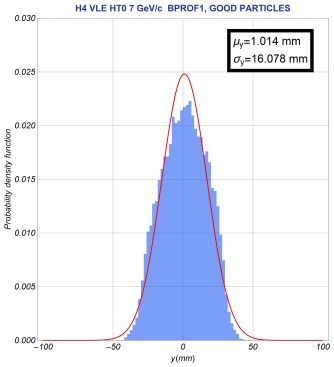

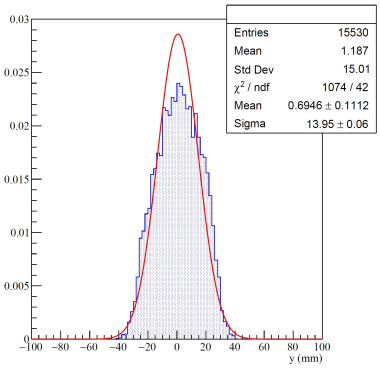

(b) *BPROF1, Vertical*

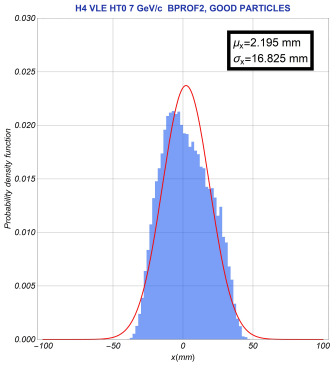

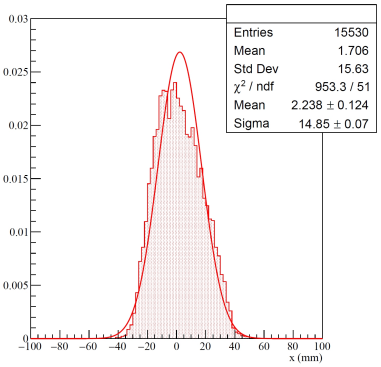

(c) *BPROF2, Horizontal*

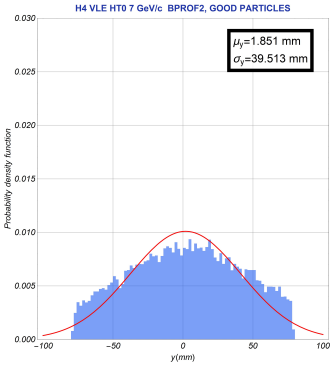

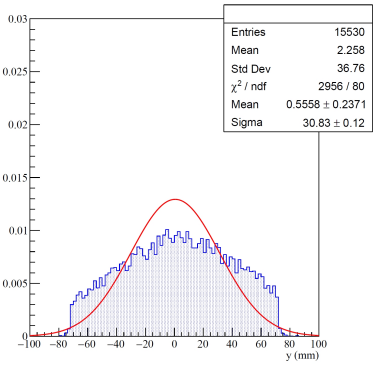

(d) *BPROF2, Vertical*

Figure 6.11: *H4-VLE 7 GeV/c good particles profiles in PTC (left) and G4BeamLine (right).*

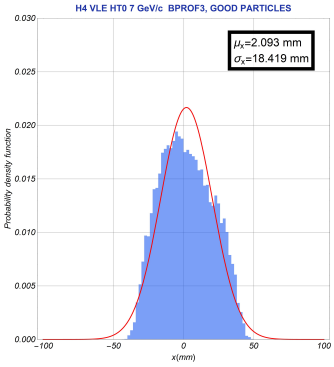

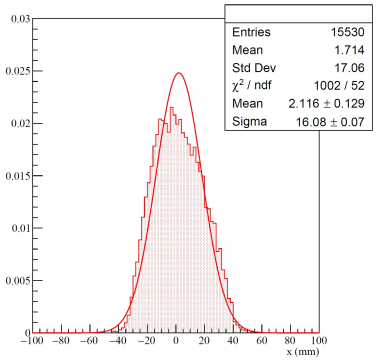

(a) *BPROF3, Horizontal*

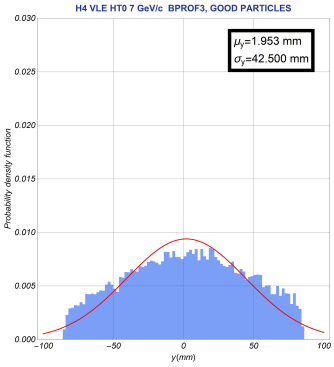

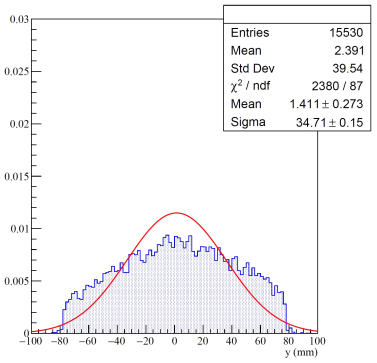

(b) *BPROF3, Vertical*

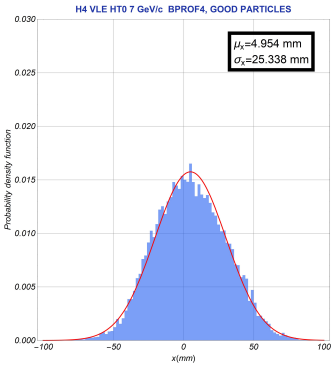

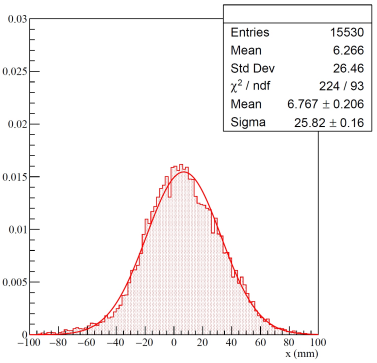

(c) *BPROF4, Horizontal*

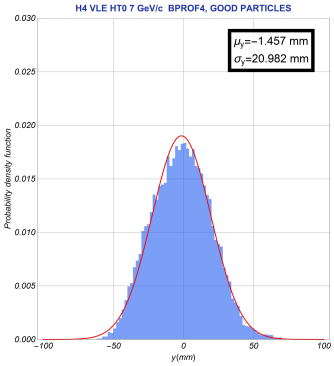

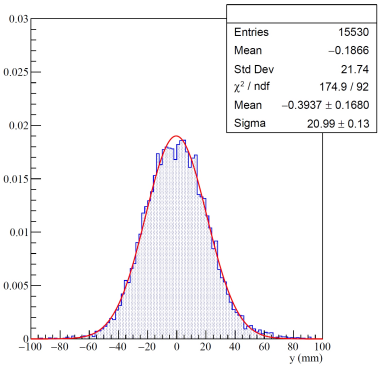

(d) *BPROF4, Vertical*

Figure 6.12: *H4-VLE 7 GeV/c good particles profiles in PTC (left) and G4BeamLine (right).*

H4-VLE 7 GeV/c, Good particles profiles								
	v0 Optics				High Transmission Optics			
	$\mu_x(mm)$	$\sigma_x(mm)$	$\mu_y(mm)$	$\sigma_y(mm)$	$\mu_x(mm)$	$\sigma_x(mm)$	$\mu_y(mm)$	$\sigma_y(mm)$
	BPROF1							
G4BL	3.73	21.94	0.85	15.01	1.93	24.17	1.19	15.01
PTC	6.68	20.48	1.25	16.03	5.47	23.15	1.01	16.08
	BPROF2							
G4BL	2.97	14.30	1.84	36.94	1.71	15.63	2.26	36.76
PTC	2.56	15.09	2.65	39.86	2.19	16.83	1.85	39.51
	BPROF3							
G4BL	3.01	15.97	1.96	39.74	1.71	17.06	2.39	39.54
PTC	2.49	16.90	2.82	42.88	2.09	18.42	1.95	42.50
	BPROF4							
G4BL	7.10	33.18	0.28	31.09	6.26	26.46	-0.19	21.74
PTC	5.97	29.97	-1.27	30.93	4.95	25.34	-1.46	20.98

Table 6.13: *Comparison between the good particles distributions at the four profile monitors of H4-VLE for a nominal momentum of 7 GeV/c, as obtained in the PTC simulations, and independent G4BeamLine simulations.BPROF1, BPROF2 and BPROF3 are placed tilted, while BPROF4 with respect to the EHN1 floor.*

The results obtained are very consistent with each other, despite core differences in the two programs.

In particular, the tracking of a particle inside a magnetic element is realized differently in G4Beamline (and any other Monte Carlo code) and in PTC. Specifically, while in PTC analytical integration of the Exact Hamiltonian is used for the trajectory of each particle, G4BeamLine numerically integrates the equation of motion, rendering the former superior in terms of precision.

The G4BeamLine simulation however is superior to PTC in modeling the detailed beamline geometry. In PTC the dipole magnets are simplistically simulated having a rectangular aperture corresponding to the aperture of magnetic core. The quadrupole magnets are modeled as circular, with their aperture corresponding to the beam pipe aperture inside the magnets (100 mm in radius). In G4BeamLine, the exact design of these magnets is modeled, including the coil material and surrounding metal, allowing also for interaction of the impinging particles with the material, possibly generating particle showers.

Additionally, in PTC the magnetic field of the dipole magnets is assumed homogeneous along the x axis, while the "default", simplistic model for the fringe field extent has been implemented. The G4BeamLine simulation uses a map of the magnetic field, as measured in [24].

The beam pipe in PTC is unavoidably modeled as circular, with its center following the central trajectory. While this is realistic for the drift spaces and the quadrupole magnets, the beam pipe inside a bending magnet is in reality custom-made as illustrated in Fig. 6.13, compared to the curved beam pipe of the PTC model. This is considered the primary reason leading to major differences in the expected rate with the more accurate G4BeamLine simulations.

G4BeamLine models the instrumentation of the beamline, allowing for interaction

of the beam with the detector material, leading to energy losses and multiple scattering. Finally, in contrast to PTC, G4BeamLine accounts for particle decays.

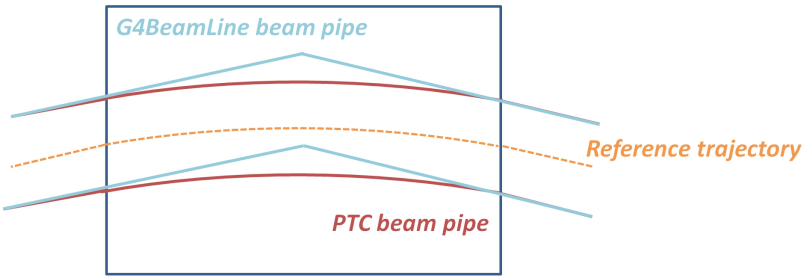

Figure 6.13: *Modeled beam pipes inside a bending magnet in PTC and in G4BeamLine, the later corresponding to its realistic design. The bending angle is exaggerated.*

6.6 Asymmetric profiles in the VLE beamlines

As shown in Tables 6.12 and 6.13, all profiles along H2-VLE and H4-VLE are asymmetric. For the horizontal plane, the asymmetry is more evident if all particles are tracked (rather than only the good particles).

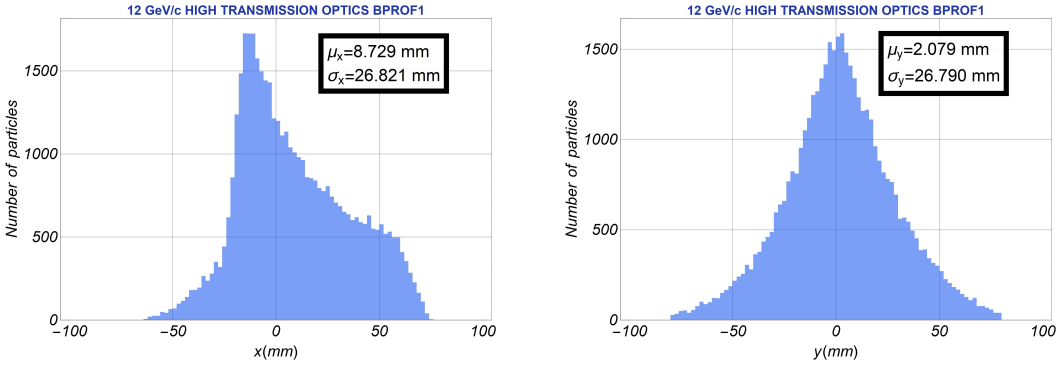

Figure 6.14: *Profiles at BPROF1 in H2-VLE, 'High Transmission Optics', when all particles are tracked. The horizontal plane is asymmetric towards positive and negative x, while the vertical is symmetric, apart from a $\sim 2mm$ offset.*

For example, in Fig. 6.14 the profiles of all particles at BPROF1 in H2-VLE are shown. A ~ 8 mm offset is visible in the horizontal plane, while the corresponding offset is only ~ 0.46 mm if only the good particles are tracked (Table 6.12). In the vertical plane, a 2mm offset is visible, which is almost identical to the offset of the good particles distribution. Compared to the horizontal plane which is asymmetric, the vertical plane shows no particular asymmetry. The above observations are also qualitatively confirmed by G4BeamLine simulations but, since G4BeamLine includes the muon background, particle showers etc., further comparison is impossible.

Similar results are obtained at BPROF2, and in particular a ∼16 mm offset is visible in the highly asymmetric horizontal profile (in contrast to the ∼2 mm offset of the corresponding good particles distribution), while the vertical plane is consistent with the good particles distribution, illustrating a ∼2 mm offset. BPROF3, placed right after BPROF2, exhibits similar characteristics.

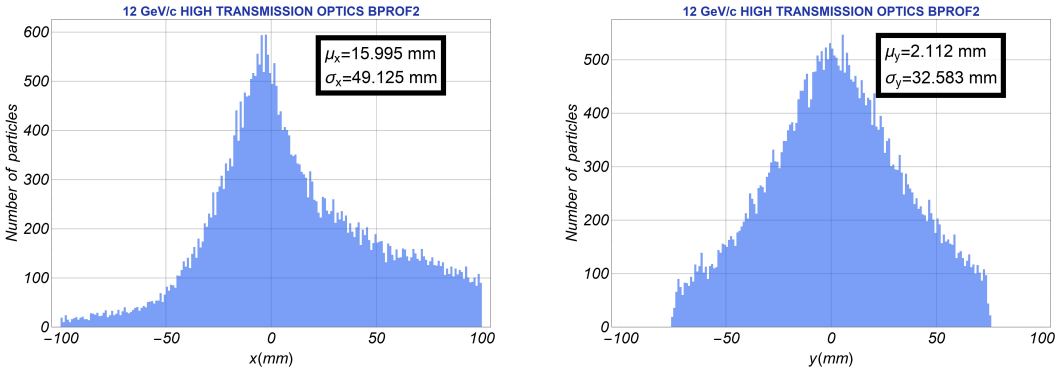

Figure 6.15: *Profiles at BPROF2 in H2-VLE, 'High Transmission Optics', when all particles are tracked. The horizontal plane is asymmetric towards positive and negative x, while the vertical is symmetric, apart from a ∼2 mm offset.*

Whichever asymmetries observed in the beam profiles stem from two sources; firstly, asymmetries in the initial particle distribution and secondly, higher order effects.

As already discussed in Section 3.4, the first order calculations are sufficient even for large spatial and angular offsets. The first order approach should therefore explain the observed vertical beam offset at the profile monitors, since in the non-bending plane the higher order corrections are practically negligible (Fig. 3.1). In first order, the coordinates of a particle in the non-bending plane at each position are a linear combination of the spatial and angular coordinates at the production point and therefore, for a symmetric emittance distribution, no asymmetries in the profiles throughout the beamline are expected. However, as already mentioned in Section 5.1, the initial 12 GeV/c production illustrates a 1.1 mm horizontal offset with respect to the EHN1 floor which is translated, in the tilted reference system, into a horizontal offset of 0.8 mm and a vertical offset of -0.6mm. This initial offset determines the vertical acceptance (Table 6.1), which is ∼-0.6 mm for all optics modes. Combining with a rather large negative R_{33} term at the position of the three profile monitors (~ -6 mm/mm) the observed positive offset at the vertical BPROFs is understood. It therefore becomes clear that the impinging H2 beam defines all observed asymmetries in the vertical plane.

In the asymmetric profiles at the detectors in the horizontal plane contributes the initial emittance, having a $\mu_x = 0.8$ mm. Similarly, combining with the positive R_{11} term at the position of the profile monitors, the observed positive offsets could be explained. More important than this contribution is, however, the higher order dispersive terms in the bending plane. It has been shown that the first order approach breaks down only when significant momentum offsets (at the order of ∼5%) are introduced. Fig. 6.16

illustrates the real trajectory of a particle generated at T22 having momentum offsets $\delta = \pm 5\%$ (up) and $\delta = \pm 10\%$ (down), but zero initial spatial and angular coordinates, as simulated via PTC.

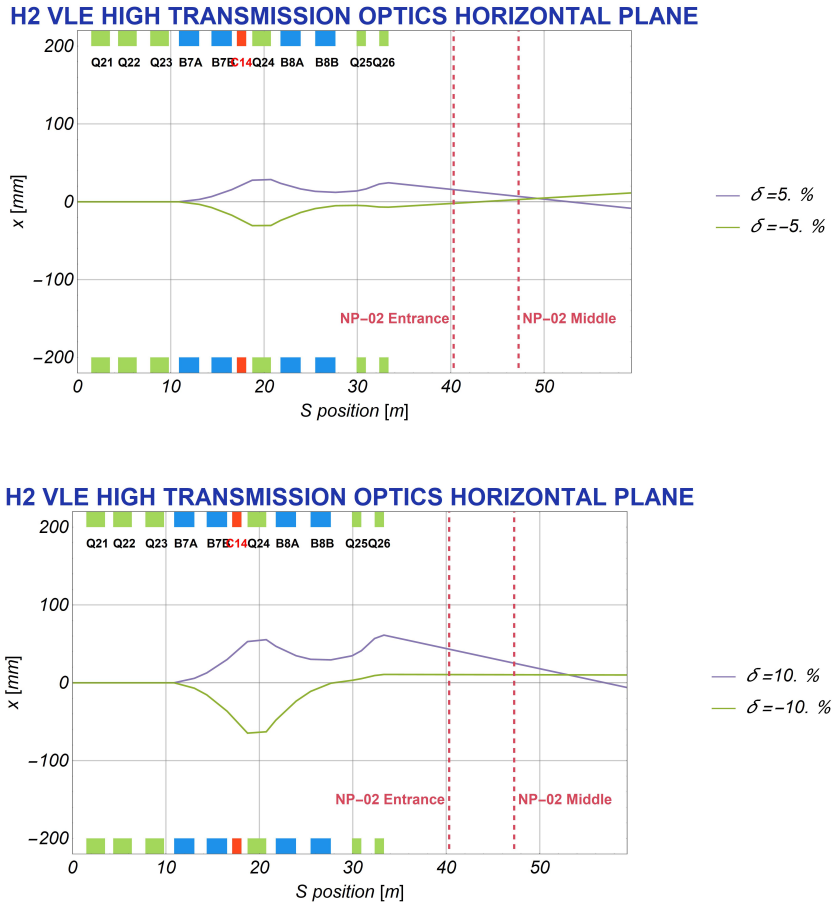

Figure 6.16: *Tracking of particles generated at T22 with zero spatial and angular coordinates, having the momentum offsets (a) ±5% and (b) ±10%.*

It can be seen that for the same magnitude, the positive and negative momentum offsets are not symmetric with respect to the reference trajectory, as would be expected in first order. Particles entering a bending magnet having zero x and x' with respect to the reference trajectory but with opposite momentum offsets follow paths with different arc lengths inside the dipole, and therefore acquire non-symmetric coordinates at the exit of the magnet. For example, for an H2-VLE magnet of deflection angle of $\sim$58 mrad for the reference trajectory, a particle with $\delta = 5\%$ will exit the dipole with coordinates $x_{5\%} = 2.99\,\text{mm}$, while the exit coordinates of a particle with $\delta = -5\%$ are $x_{-5\%} = -3.31\,\text{mm}$. The exit angles are negligibly asymmetric. Therefore, the two particles, passing through B7A and B7B result at non-symmetric positions at Q24, and specifically $x_{5\%} = 27.7\,\text{mm}$, $x_{-5\%} = -30.6\,\text{mm}$. From then on, and due to higher order chromatic aberrations at the quadrupoles, the two particles will follow different trajectories, leading to the tracks plotted in Fig. 6.16. For example at Q26, the particle

coordinates are $x_{5\%} = 24.4mm$ and $x_{-5\%} = -6.9$ mm respectively. This asymmetry is even more striking for particles with $\delta = \pm 10\%$, and particularly at Q26 the horizontal coordinates are $x_{10\%} = 43.2$ mm and $x_{-10\%} = 10.5$ mm. This "preference" towards positive spatial coordinates after B8B is evident in all optics modes of H2-VLE and is consistent with the observed profiles at BPROF1, BPROF2 and BPROF3.

6.7 Momentum bite vs collimator gap

A useful result for the NP-02 and NP-04 experiments is the dependence of the momentum acceptance (or *"momentum bite"*) on the collimator full opening. A scan of the collimator gap of H2-VLE and H4-VLE for the design momentum has been performed. The results for H2-VLE will be presented, while the results for H4-VLE are quite similar.

Fig. 6.17 illustrates the results obtained for v0 Optics and 'High Transmission Optics' for a collimator full opening from 10 mm to 90 mm, the later corresponding to its maximum value.

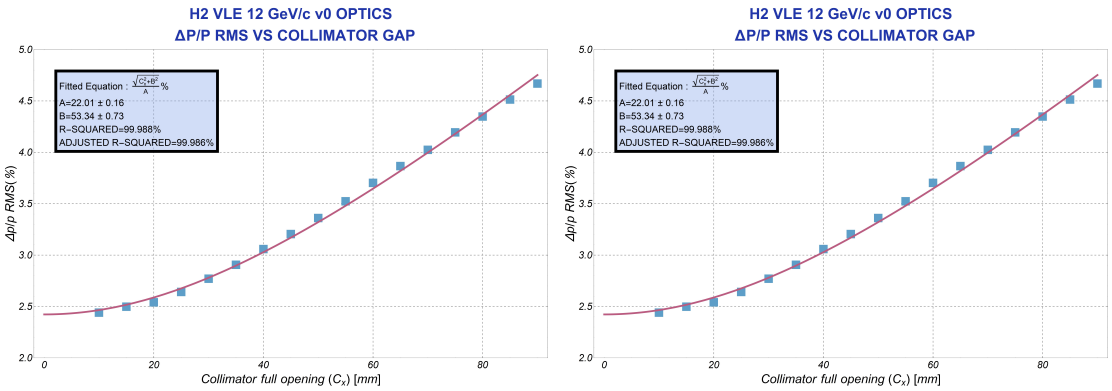

(a) **(b)**

Figure 6.17: *Momentum bite vs collimator full opening for (a) v0 optics and (b) High Transmission Optics of H2-VLE, for a nominal momentum of 12 GeV/c.*

By fitting the points similar to [11], the empirical formula has been obtained for v0 Optics,

$$\frac{\Delta p}{p}(\%) = \frac{\sqrt{C_x^2 + 53.3^2}}{22.0}\% \tag{6.1}$$

where C_x is the collimator full opening in mm. The corresponding fit, obtained in [11] via tracking in G4BeamLine yielded the empirical formula

$$\frac{\Delta p}{p}(\%) = \frac{\sqrt{C_x^2 + 51.1^2}}{22.6}\% \tag{6.2}$$

in good agreement with the result obtained via PTC.

For 'High Transmission Optics' the same fit results in the formula:

$$\frac{\Delta p}{p}(\%) = \frac{\sqrt{C_x^2 + 57.1^2}}{24.4}\% \tag{6.3}$$

It is clear from Fig. 6.17 that 'High Transmission Optics' results in a generally smaller momentum spread compared to v0, for the same collimator settings, due to the better focusing of the beam at the collimator. In particular, in the initial optics configuration, $R_{11} = -2.54\,\text{mm/mm}$, $R_{12} = -0.13\,\text{mm/mrad}$, while in 'High Transmission Optics', $R_{11} = -2.43\,\text{mm/mm}$, $R_{12} = 0.07\,\text{mm/mrad}$. For example for the maximum collimator opening, 'High Transmission Optics' provides a 4.3% $\Delta p/p$ RMS, while v0 Optics 4.7%. For a full opening of 60mm, the former provides 3.5%, while the latter 3.7%. As the gap is reduced, the results gradually coincide. This is a result of the non-zero R_{11} and R_{12} values at the collimator, and therefore as the gap is reduced, the contribution of the aforementioned terms dominates that of the dispersive term, and unavoidably particles with large spatial and angular offsets will be absorbed.

Fig. 6.18 illustrates the transmission of particles as a function of the collimator gap for v0 and 'High Transmission Optics'. The results have been normalized to the particle transmission in 'High Transmission Optics' obtained in the maximum collimator opening. 'High Transmission Optics' retains a generally larger particle rate, but for collimator settings below 40 mm, the two curves begin to converge, due to inevitable absorption of particles generated at T22 having large spatial and angular offsets.

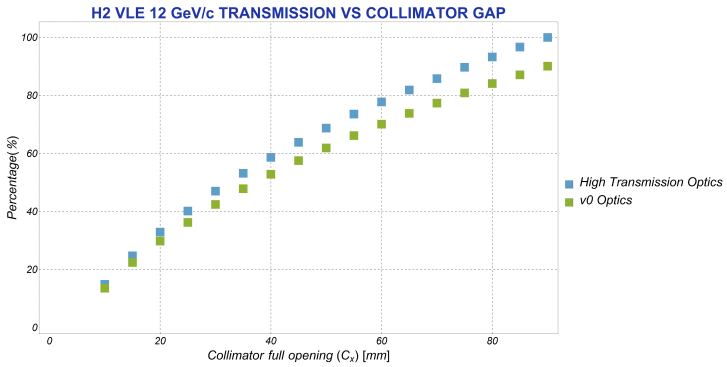

Figure 6.18: *Particle transmission vs collimator full opening for v0 Optics and High Transmission Optics, normalized to the High Transmission Optics particle transmission for the maximum collimator opening.*

CHAPTER 7

Misalignment studies

Since all the magnetic elements of the newly installed extensions will be placed om a tilted plane with respect to the ground, as also discussed in Chapter 4 , and taking into account their considerable weight (∼28 tons for an "MBPL" magnet, ∼9 tons for a "QPL" magnet), their exact alignment can be a quite challenging process.

Fig. 7.1 shows the placement of the MBPL magnets on their support for H2-VLE and H4-VLE. The exterior of the quadrupole magnets is also rectangular, and therefore their placement on their support is similar.

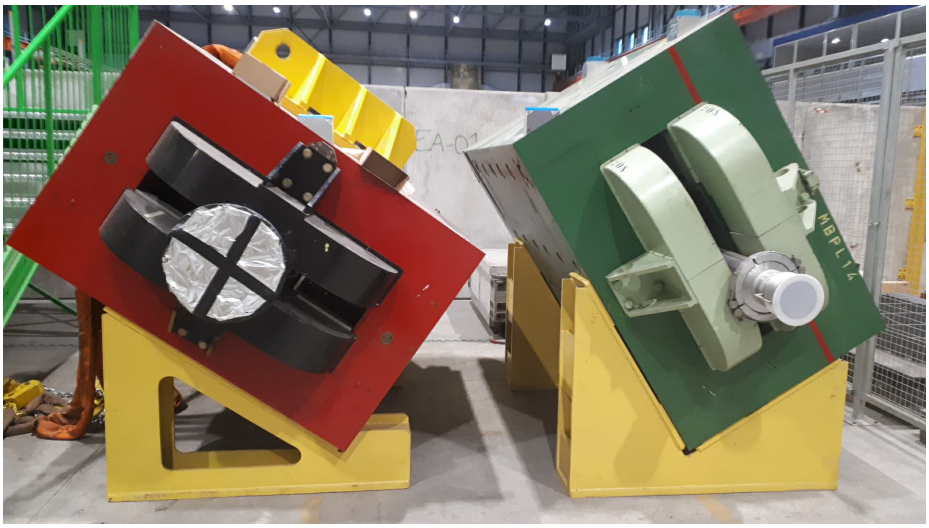

Figure 7.1: *Placement of the MBPL magnets on their support in H2-VLE (left) and H4-VLE(right).*

The errors of the magnet placement stem from various sources, and particularly:
- mistakes in the construction of the support
- error in the placement of the magnet on its support
- error in the alignment of the support itself.

The surveying process however is theoretically expected to align the magnets within an error of 0.1 mm for spatial misalignments and 0.05° for angular misalignments.

The purpose of the present study is to explore all possible misalignment types and report the ones that affect the beam characteristics the most in terms of particle losses

and beam offsets at the experiment. Moreover, a dependence of these characteristics on the misalignment tolerance will be studied.

In order to be as close to reality as possible, the following types of misalignments have been included in the analysis, schematically shown in Fig. 7.2: a magnet can be misplaced along the longitudinal distance s, as shown in (1). The magnet can be either misplaced transversely on its support, or the entire support can be misplaced transversely (cases (2) and (3) respectively). Finally, the tilt angle of a magnet can be misaligned, as in case (4).

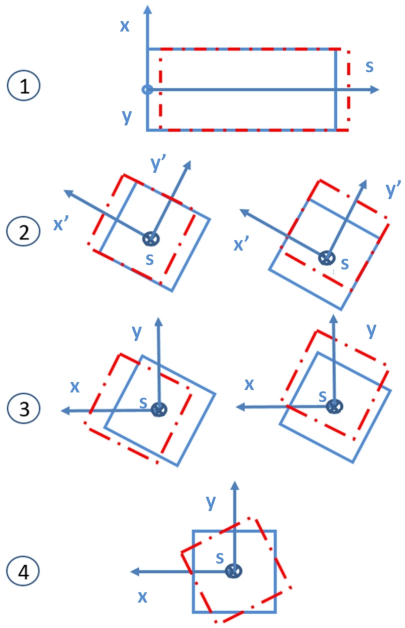

Figure 7.2: *(1) Longitudinal misalignments, (2) transverse misalignments along the tilted reference system, (3) transverse misalignments along the straight reference system and (4) angular misalignments.*

Given that the exact placement of each magnet is unknown (within the theoretical alignment precision), numerous iterations, each one misplacing the magnet by a different value had to be examined. Therefore, for every misalignment type studied, 500 runs were considered, each one misplacing the magnet randomly around its ideal position using a Gaussian distribution. Various standard deviations of the distribution have been examined, corresponding to realistic cases, pessimistic or optimistic ones. For each run, a subset of the initial acceptance (5000 particles, to reduce the computing time) were tracked along H2-VLE or H4-VLE. All results have been compared to the ideal magnet placement.

7.1 Dependence of beam characteristics on misalignment type

A first study is to determine the misalignment type that mostly affects the beam characteristics for both beamlines. For this purpose, the following cases have been examined:

quadrupole transverse misalignments, quadrupole angular misalignments, quadrupole longitudinal misalignments, dipole transverse misalignments and dipole longitudinal misalignments. In each case all magnets have been misaligned simultaneously, each one with a random value around the ideal position with a standard deviation $\sigma = 0.5\,\text{mm}$ for the case of spatial misalignments, and $\sigma = 0.5°$ for the case of angular, corresponding to rather pessimistic cases, with a safety factor of 5 and 10, respectively, compared to the theoretical alignment tolerance.

In Fig 7.3 the mean losses obtained in the 500 random runs for each of the aforementioned cases are shown, both for H2-VLE and H4-VLE. The error bars correspond to one standard deviation of the losses. It can be seen that the transverse misalignments of the quadrupoles is the most significant misalignment type, leading to an average of $\sim$10% losses in both beamlines with respect to the ideal magnet placement. The misalignment type also influencing the particle transmission considerably is the angular misalignment of the quadrupoles, having an average of $\sim$7% mean losses. All other misalignments have minor effect on the particle transmission.

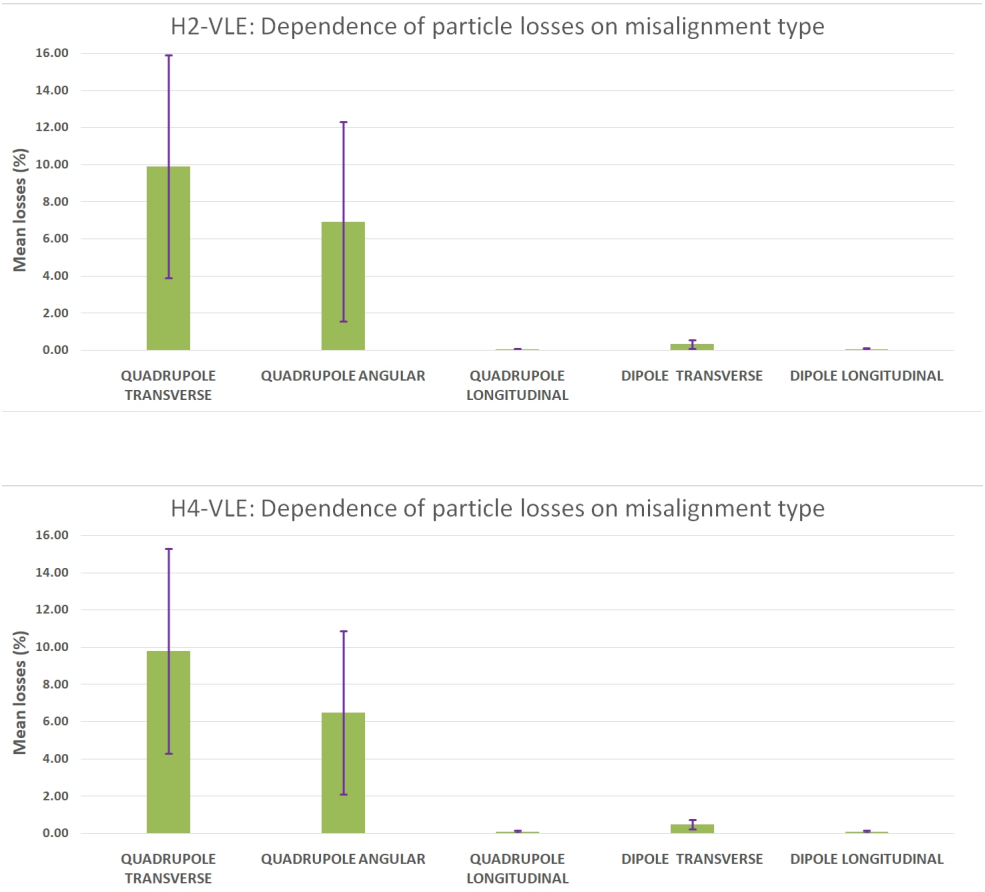

Figure 7.3: *Mean losses of various misalignment types for H2-VLE and H4-VLE. The standard deviation of the Gaussian distribution is 0.5 mm for spatial and 0.5° for angular misalignments. The transverse and angular misalignments of the quadrupoles affect the particle transmission the most.*

Apart from the expected losses, a meaningful quantity of measurement is the beam transverse position at the experiment compared to the expected position of the beam in the ideal magnet placement. A useful quantity is the RMS of the beam offset, the magnitude of which indicates how sensitive the position of the beam is in each misalignment type studied. The beam offset has been calculated at BPROF4 (the last profile monitor of both beamlines) with respect to the floor of EHN1, in order to provide useful information to reverse engineer any potential observed beam offset. It is shown in Fig. 7.4 that the transverse misalignments of the quadrupoles affect the beam position at BPROF4 the most, with an RMS of $\sim$9.6 mm in the horizontal plane for H2-VLE (5.1 mm for H4-VLE), and $\sim$8.3 mm in the vertical (4.3 mm for H4-VLE). No other misalignment affects the beam position notably.

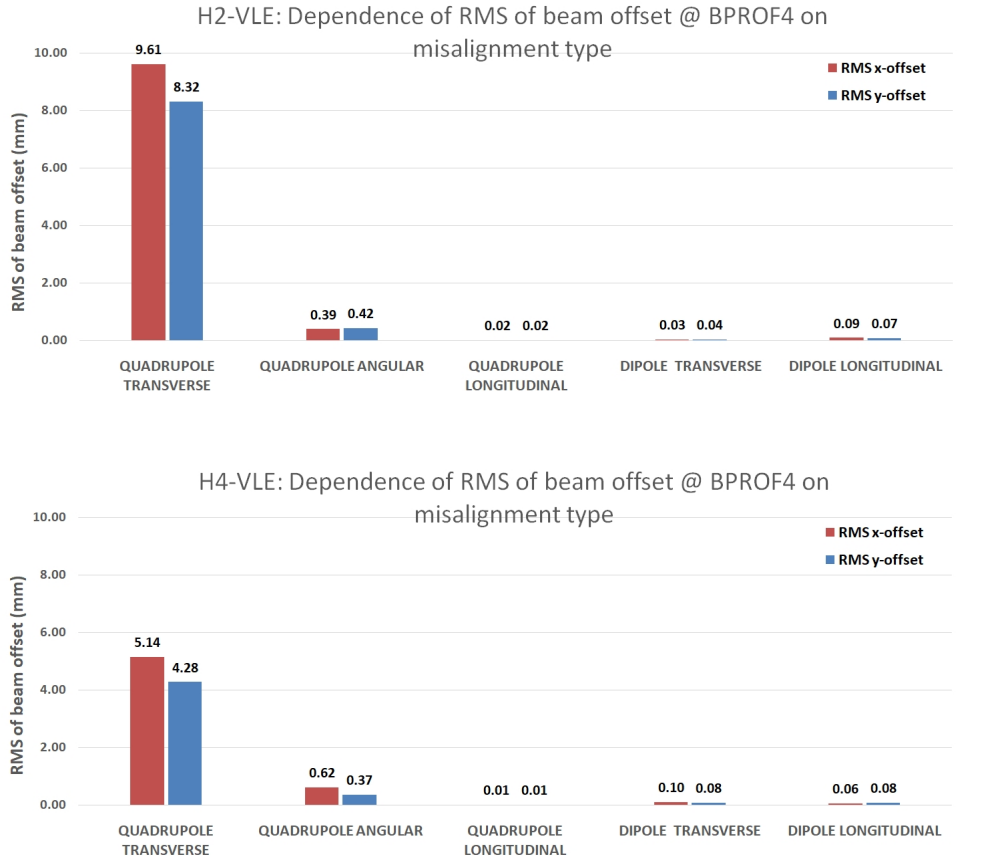

Figure 7.4: *Beam offsets of various misalignment types for H2-VLE and H4-VLE. The standard deviation of the Gaussian distribution is 0.5 mm for spatial and 0.5° for angular misalignments. Only the transverse misalignments of the quadrupoles affect the beam position.*

When a quadrupole is misaligned transversely, its focal point shifts in the same manner. This causes particle losses in the aperture of the next magnetic elements and, inevitably, the beam transverse position is also shifted. Spot size changes of the order of $\sim$1 mm are expected.

A longitudinal quadrupole misalignment simply moves the focal point along the s

axis, causing a potential enlargement or reduction of the beam size at the experiment and mildly affecting the losses. This effect is however negligible; the variation of the beam size at BPROF4 is only 0.01 mm in both beamlines, and the mean losses are 0.04% in H2-VLE (0.08% in H4-VLE).

A quadrupole angularly misaligned will focus and defocus the beam in a reference system rotated along s by the same misalignment angle. This focusing leads to significant aperture losses and a variation of the spot size at BPROF4 ($\sim$2 mm in both planes), without affecting the transverse position of the beam at the experiment.

Misalignments of a dipole along the axis parallel to its poles (x' in the notation used in the thesis) result to no observable effect due to the assumed uniformity of the magnetic field along x (see Section 4.4). Such a misalignment could only lead to losses due to the horizontal dipole apertures, but since these are extremely large (210 mm half gap), the horizontal misalignment leads to practically zero effect on the beam.

Misalignments along the y' axis of the dipole alter the field "seen" by the beam due to the y-dependent fringe field effects, however these, as can be seen in Fig. 7.4, are negligible. Additionally, due to its small vertical aperture (70 mm half gap), a misalignment along y' leads to minor losses in the dipole apertures (0.3% mean particle losses in H2-VLE, 0.5% in H4-VLE).

Due to the restricted definitions of the reference systems, it was impossible to study the angular misalignments of the dipole magnets using PTC in a MAD-X environment. Nonetheless, the angular misalignments of the dipoles are expected to affect the beam characteristics at a magnitude similar to the transverse misalignments of the quadrupoles.

It should be mentioned that the transverse misalignments of the quadrupoles illustrated in Figs. 7.3 and 7.4 are with respect to the tilted reference system (case (2) of Fig. 7.2). However, the misalignments with respect to the straight reference system (case (3) of Fig. 7.2) are simply a linear combination of those with respect to the tilted reference system and therefore the results are expected to be very similar, as is shown in Table 7.1. All transverse quadrupole misalignments have therefore been studied in the tilted reference system, since the obtained results can be better interpreted when the magnets are misplaced along their "natural" axes.

Transverse quadrupole misalignments of H2-VLE - tilted and straight reference system			
	Average losses (%)	RMS x-offset (mm)	RMS y-offset (mm)
Titled system	9.8 ± 6.1	9.40	8.01
Straight system	9.9 ± 6.0	9.61	8.32

Table 7.1: *Comparison between transverse misalignments of the quadrupoles with respect to the tilted or the straight reference system for H2-VLE. The standard deviation of the Gaussian distribution is $\sigma = 0.5$ mm in both cases.*

7.2 Quadrupole transverse misalignments: Dependence of beam characteristics on misalignment tolerance

Given that the beam characteristics are mostly affected by the transverse misalignments of the quadrupoles, a second study was conducted to determine the dependence of the results on various standard deviations of the Gaussian distribution. This is illustrated in Figs. 7.5 and 7.6 and specifically the cases $\sigma = 0.5$ mm (pessimistic case), $\sigma = 0.1$ mm (realistic case) and $\sigma = 10$ μm. (optimistic case) have been examined.

It can be seen that the dependence of both the mean losses and the RMS of beam offsets on the standard deviation of the Gaussian distribution is almost linear for both beamlines. Additionally, for a standard deviation of 0.1 mm (corresponding to the theoretical maximum alignment error) or less, the deviations are not significant.

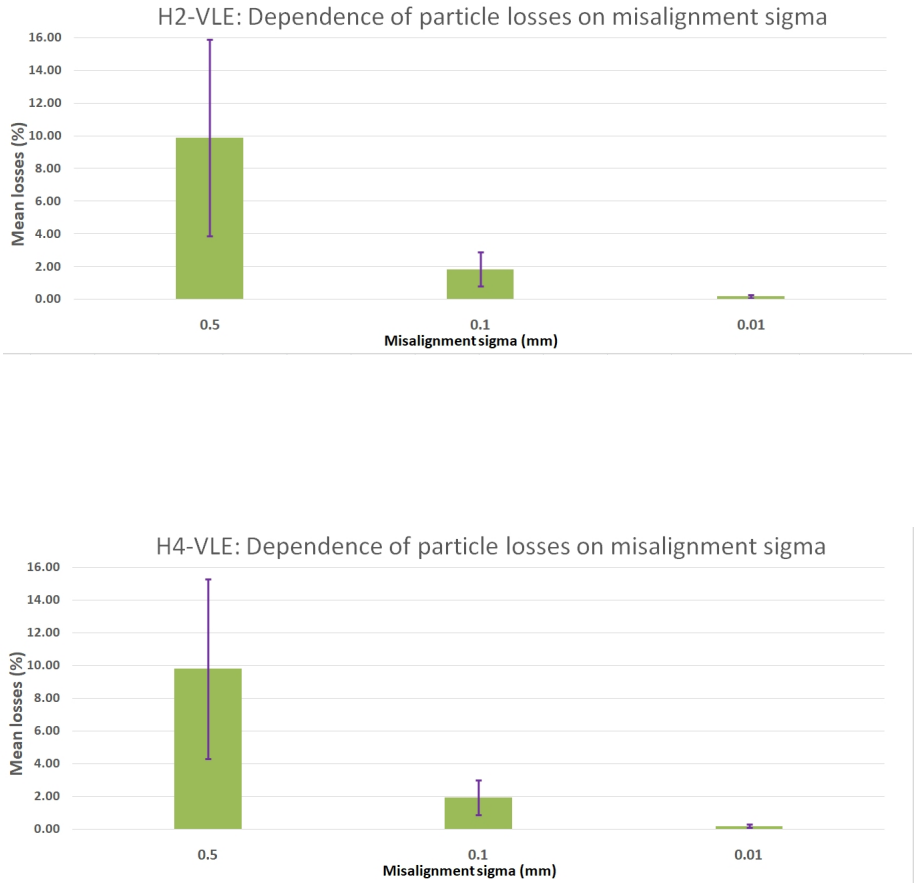

Figure 7.5: *Mean losses of the transverse misalignments of the quadrupoles in H2-VLE and H4-VLE, for various standard deviations of the Gaussian distribution.*

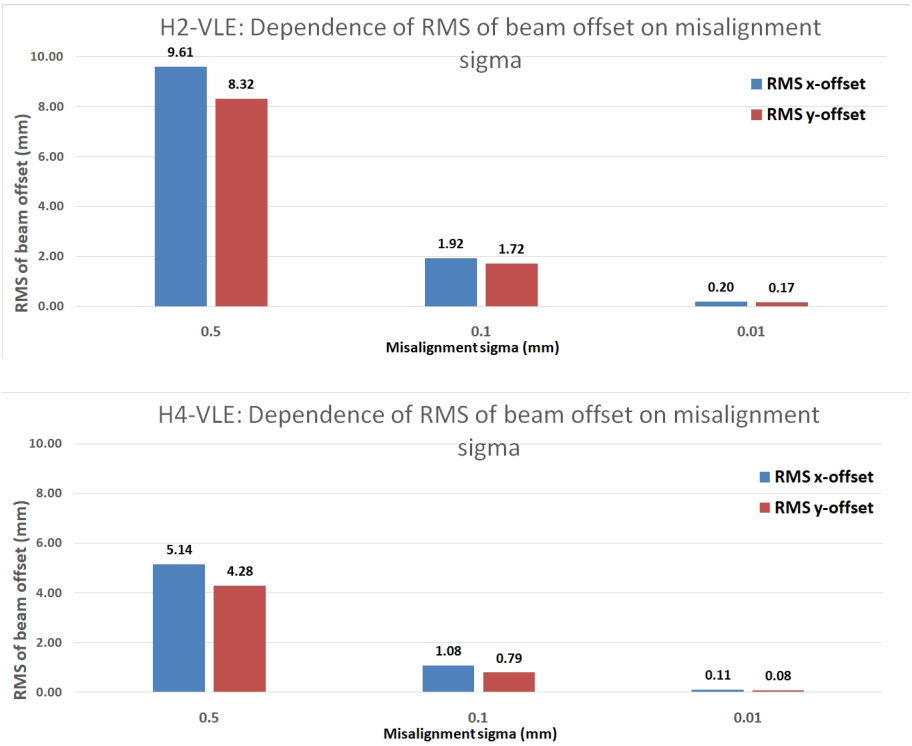

Figure 7.6: *Beam offsets at BPROF4 of the transverse misalignments of the quadrupoles in H2-VLE and H4-VLE, for various standard deviations of the Gaussian distribution.*

7.3 Quadrupole sensitivity analysis

A useful result for the surveying process is to identify specifically which quadrupoles mostly affect the beam characteristics. For this purpose, a study was conducted where each quadrupole has been misaligned separately, and similarly, 500 runs with a standard deviation of σ =0.5 mm have been examined for each quadrupole. Since the results are qualitatively different for H2-VLE and H4-VLE, the two beamlines will be presented separately.

7.3.1 H2-VLE

The results for H2-VLE are shown in Fig. 7.7, indicating that the beam is mostly sensitive to the quadrupole triplet, and specifically the second quadrupole of the beamline (Q22). The field lens and the focusing doublet do not contribute to the losses or the beam offset considerably.

This behavior can be better understood if the factors contributing to the sensitivity of the beam characteristics on a specific quadrupole are identified. Specifically, a misaligned quadrupole of large $\sqrt{k}L$ value is expected to affect the beam more than a quadrupole of a small $\sqrt{k}L$ value, for the same misalignment magnitude (see Eq. 2.21 and 2.22). A quadrupole placed towards the experiment will affect the beam less than a quadrupole placed at the beginning of the beamline, since the effect is cumulative. Finally, a misaligned quadrupole is expected to affect the beam the most at the positions

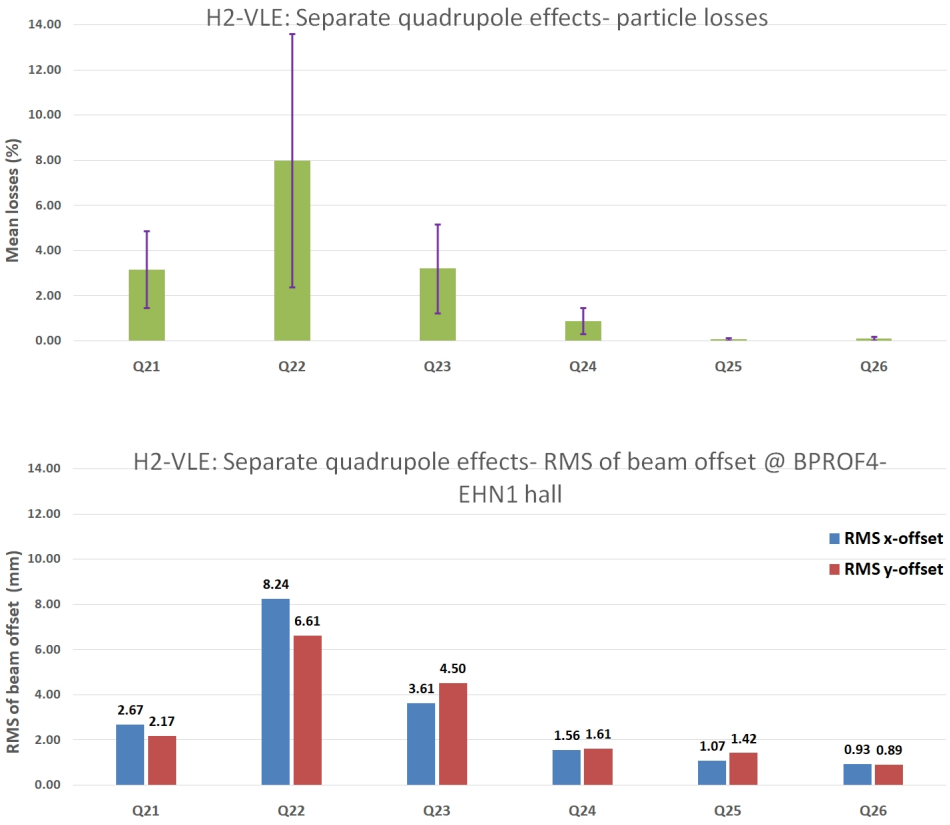

Figure 7.7: *Mean losses and beam offsets of separate transverse quadrupole misalignments for H2-VLE having a standard deviation 0.5 mm*

where the beam envelope is large.

In order to correlate the aforementioned parameters with the observed results, Fig. 7.8 shows the results of Fig. 7.7, this time with respect to the tilted reference system. Fig. 7.9 illustrates the tracking of 1000 particles in the ideal magnet placement, showing simultaneously the $\sqrt{k}L$ values of the quadrupoles.

It is shown that the misplacement of Q22 affects the horizontal (tilted) beam position at BPROF4 the most, with an RMS of 10.03 mm. This is consistent with the large horizontal beam size at Q22, combined with its $\sqrt{k}L$ value, which is the largest of all quadrupoles. The vertical beam position at BPROF4 is affected less (3.30 mm in RMS), due to the much smaller vertical beam size at Q22. Additionally, Q23 affects the beam position significantly due to the large $\sqrt{k}L$ value. Again, due to the larger vertical beam envelope at this position, the vertical beam position is more sensitive than the horizontal. While the beam size at Q21 is rather small, since it is the first quadrupole of the beamline and due to its large $\sqrt{k}L$ value, it also contributes to the beam offset significantly. Misalignments of Q24 cause mild beam offsets and particle losses due to the small beam envelope at this position. Finally, despite the large vertical beam envelope at Q25 and the horizontal beam envelope at Q26, these quadrupoles do not result to

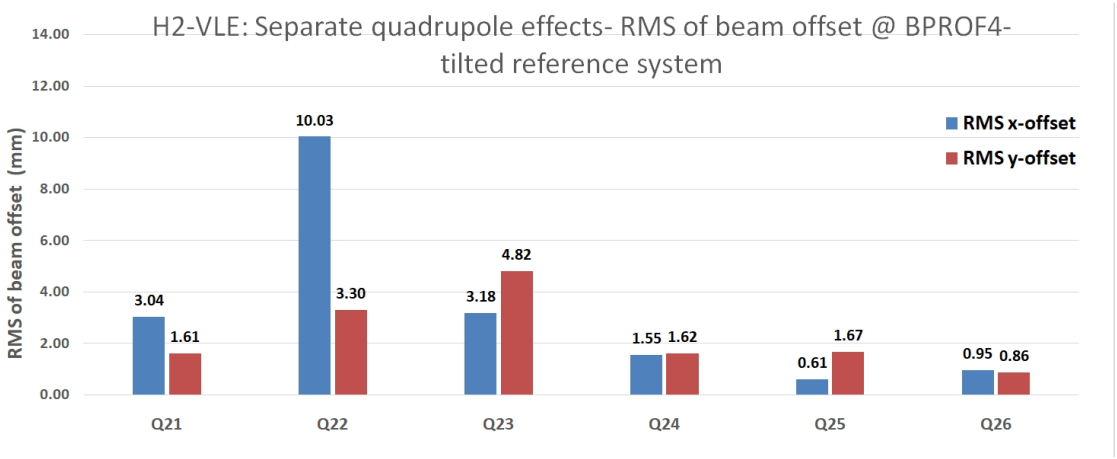

Figure 7.8: *Beam offsets of separate transverse quadrupole misalignments. The standard deviation of the Gaussian distribution is 0.5mm.*

significant changes of the beam characteristics, due to their small $\sqrt{k}L$ value, and due to their vicinity from the experiment. To conclude, during the alignment process, particular attention should be paid to the transverse placement of Q22 and Q23.

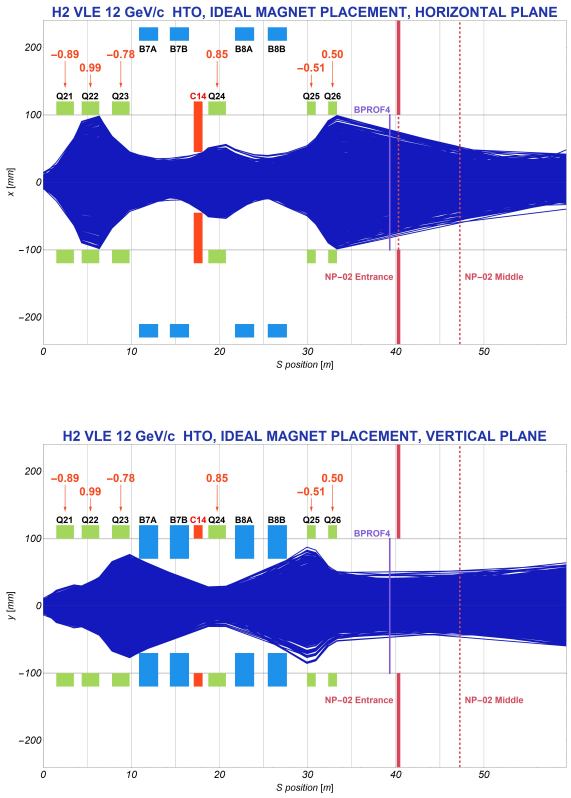

Figure 7.9: *Tracking of 1000 particles along the H2-VLE beamline, assuming an ideal magnet placement.*

A visualization of the effect of the transverse misalignments of the quadrupoles is

shown in Fig. 7.10, for the same 1000 particles of Fig. 7.9. In (a) Q22 has been misaligned by 1 mm in the horizontal (tilted) plane, while in (b) Q23 has been misaligned in the vertical (tilted) plane by the same magnitude. It is seen that by misaligning Q22 along the x-axis, the horizontal plane is mostly affected, leading to losses at the collimator and at Q26, and to a quite large beam offset towards negative values at the experiment. The corresponding vertical plane is only mildly affected. By misaligning Q23 along the y-axis, the horizontal plane remains unaffected, while the vertical plane exhibits significant losses at B8B and the beam is steered at the experiment. Both cases can be justified in the context of the previous discussion.

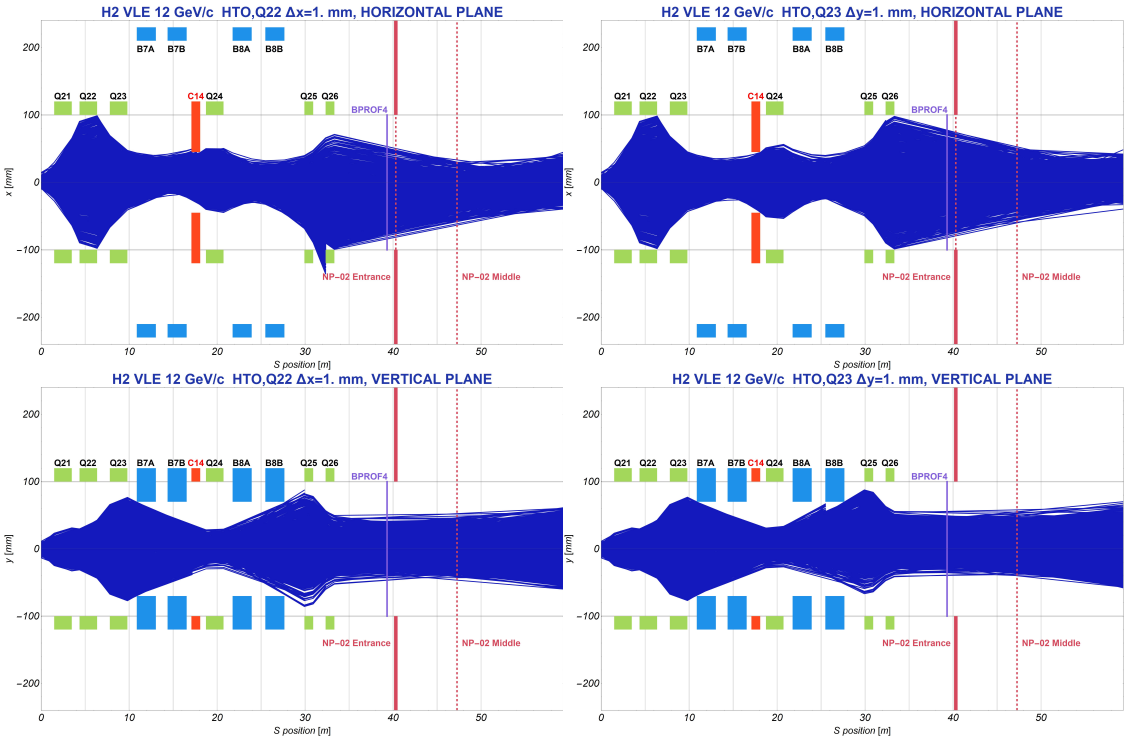

(a) $Q22$, $\Delta x = 1\,mm$ **(b)** $Q23$, $\Delta x = 1\,mm$

Figure 7.10

Finally, Fig. 7.11 illustrates the effect of the angular misalignment of all quadrupoles simultaneously. The particular set of misalignments is a specific case obtained in the first study shown in 7.3, leading to the maximum losses observed out of all 500 runs. Specifically, the misalignment angles are $\theta_{21} = 0.14°$, $\theta_{22} = -1.63°$, $\theta_{23} = 0.90°$, $\theta_{24} = 1.35°$, $\theta_{25} = 0.25°$, $\theta_{26} = 0.58°$, some of which are at the 3σ of the Gaussian, corresponding to a pessimistic case. In both planes, no offsets are observed at BPROF4, but significant losses occur. As already mentioned, by angularly misaligning the quadrupoles, the beam focuses in a plane rotated by the misalignment angle, and therefore it is not successfully focused at the collimator, leading to losses in the horizontal plane. Moreover, losses occur at B8B in the vertical plane due to ineffective focusing, and at Q26 in the horizontal plane. This focusing also leads to a variation of the spot size at BPROF4,

without affecting the position of the beam.

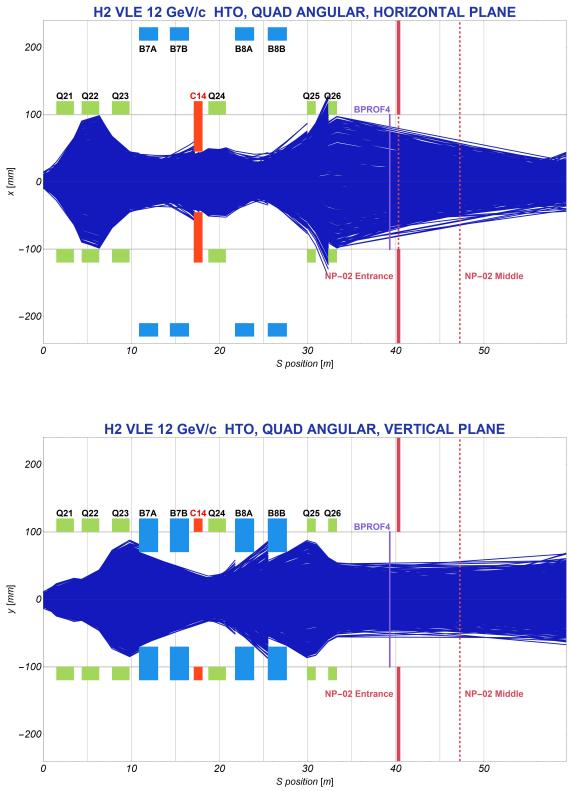

Figure 7.11: *Angular misalignment of all quadrupoles of H2-VLE.*

A final useful result for the H2-VLE beamline is the expected beam profiles at the profile monitors BPROF3 and BPROF4, in cases where a specific quadrupole has been misaligned. The placement of the monitors along the H2-VLE beamline can be found in Fig. 4.5. Specifically, BPROF3 is placed right after B8B by the same tilt angle as the magnetic elements ($\sim 34°$), and therefore the calculated profiles at this detector are also shown with respect to the tilted reference system. The results for BPROF4 (placed upstream the entrance of the cryostat) are shown in the straight reference system, due to its placement with respect to the floor of EHN1. In order to be as realistic as possible, rather than tracking a subset of the acceptance (as was done in the previous misalignment studies), in this study the entire emittance from T22 has been tracked.

In Fig. 7.12a Q22 has been misaligned by 1 mm in the horizontal (tilted) plane. It can be seen that the horizontal profile at BPROF3 is affected significantly, compared to the vertical profile that remains almost identical, consistent with the large horizontal beam envelope at Q22. At BPROF4 both profiles show considerable changes due to the mixing of the horizontal and vertical coordinates introduced by its placement with respect to the floor. Specifically the beam position has shifted ~ 11 mm in the horizontal and ~ 7 mm in the vertical plane.

In Fig. 7.12b Q22 has been misaligned by 1 mm in the vertical (tilted) plane. It is shown that even the vertical profile at BPROF3 is not that sensitive to the vertical mis-

alignment of Q22, due to the rather small beam envelope at Q22. The expected shift in the beam position at BPROF4 is only ∼3 mm in the horizontal and ∼4 mm in the vertical plane.

Fig. 7.13a shows the results obtained for a horizontal misalignment of Q23 by $1\,mm$. The horizontal profile at BPROF3 is again affected more than the corresponding vertical profile which remains almost identical, but, due to the rather small horizontal beam envelope, the expected differences are not significant. The shift in the beam position at BPROF4 is only ∼4 mm in the horizontal and ∼3 mm in the vertical plane.

Finally, in Fig. 7.13b Q23 has been misaligned by 1 mm in the vertical (tilted) plane. A shift of ∼4 mm in the horizontal plane and ∼9 mm in the vertical is expected at BPROF4, justified by the rather large vertical beam profile at Q23 and its large $\sqrt{k}L$ value.

For all cases, the beam size variation at BPROF4 is negligible (∼ 0.5 mm).

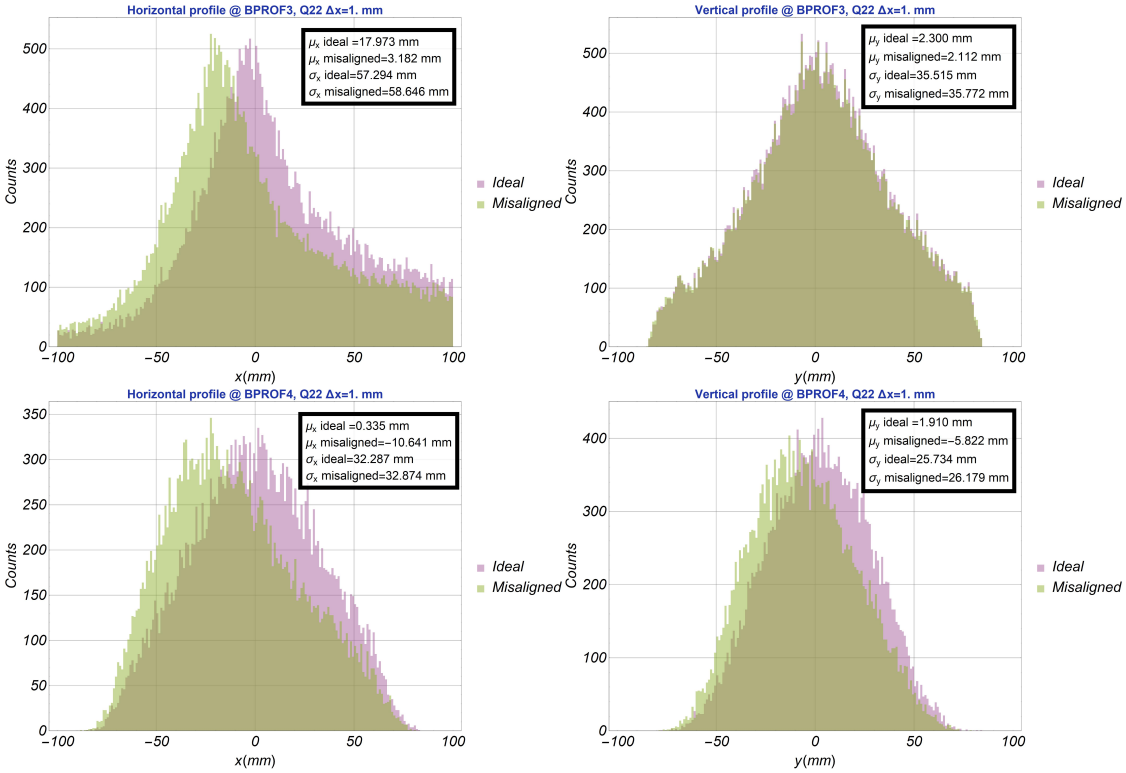

(a) *Misalignment of Q22 by* $\Delta x = 1\,mm$

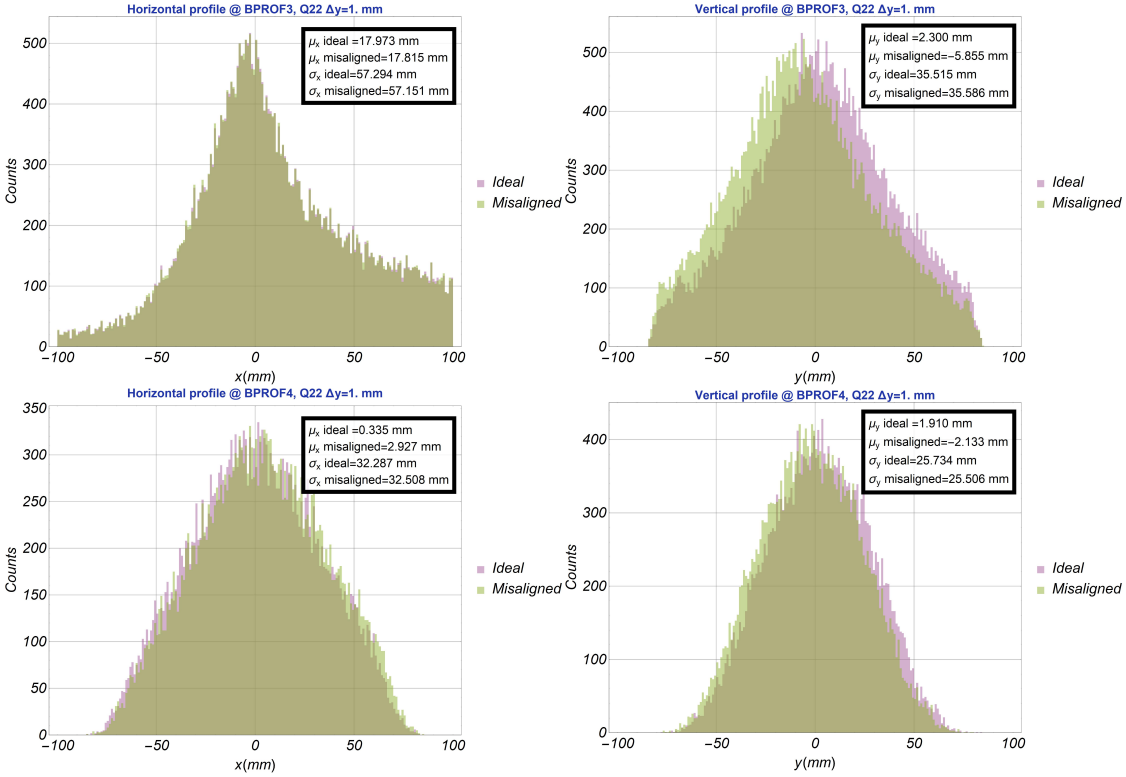

(b) *Misalignment of Q22 by* $\Delta y = 1\,mm$

Figure 7.12: *Expected profiles at BPROF3 and BPROF4 of H2-VLE, for the ideal and misaligned magnet placement.*

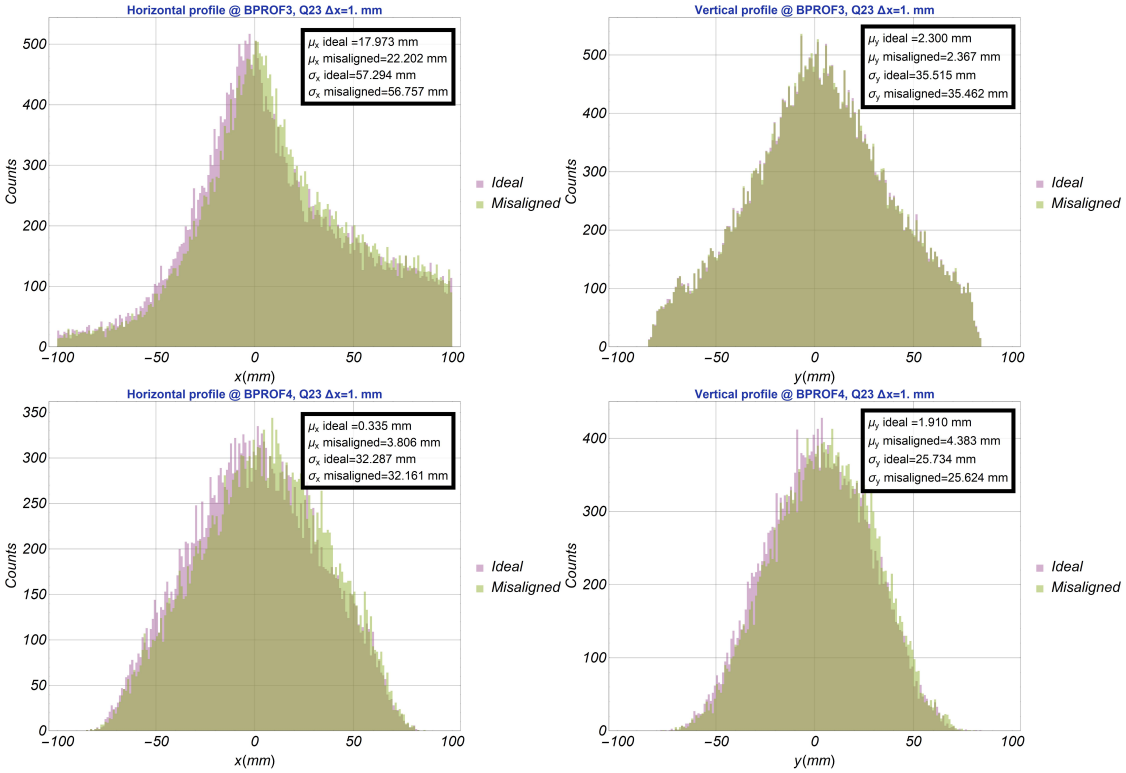

(a) *Misalignment of Q23 by* $\Delta x = 1\,mm$

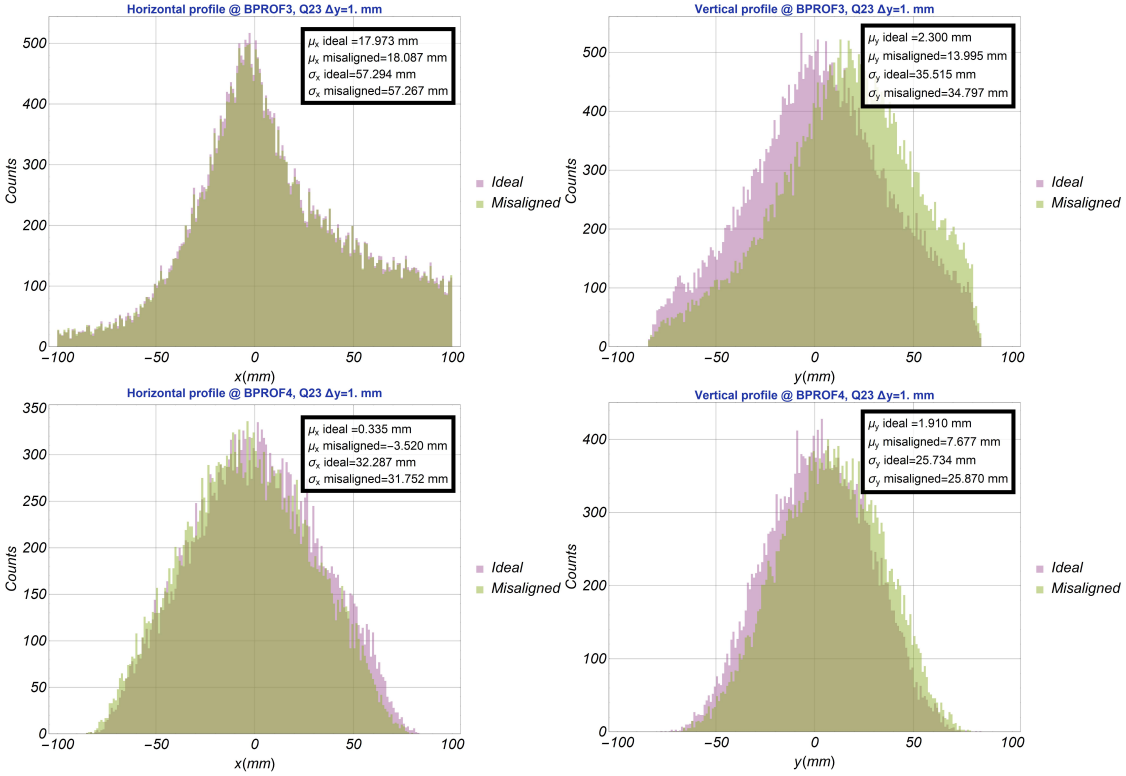

(b) *Misalignment of Q23 by* $\Delta y = 1\,mm$

Figure 7.13: *Expected profiles at BPROF3 and BPROF4 of H2-VLE, for the ideal and misaligned magnet placement.*

7.3.2 H4-VLE

Following the same method as in H2-VLE, the transverse misalignments of each quadrupole have been examined separately for the H4-VLE beam, to determine the ones that the beam characteristics are most sensitive to. Similarly, illustrated in Fig. 7.14 are the results obtained using a standard deviation of σ=0.5 mm.

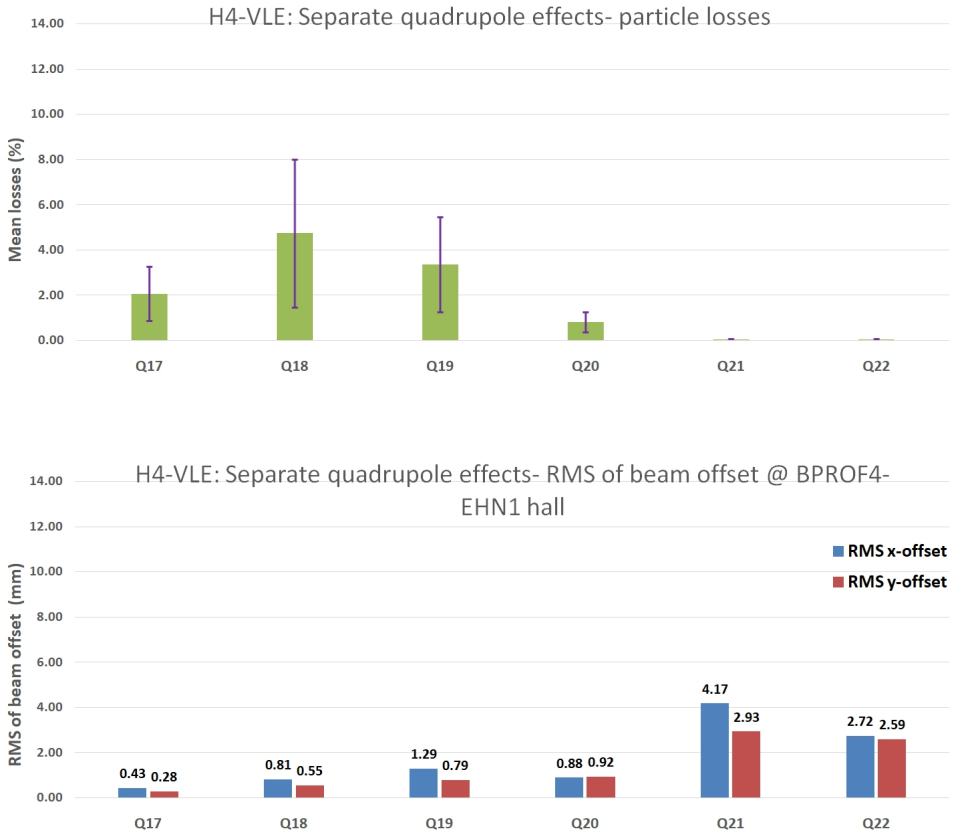

Figure 7.14: *Mean losses and beam offsets of separate transverse quadrupole misalignments for H4-VLE having a standard deviation 0.5mm*

The mean losses are qualitatively similar to the H2-VLE beam; the misalignment of the quadrupoles of the triplet leads to significantly loses, and particularly Q18. The other quadrupoles do not affect the transmission significantly. The beam position, however, is sensitive to quadrupoles Q21 and Q22 primarily, in contrast with the H2-VLE beam, where the initial triplet dominated. As will be later proved, this difference is a consequence of the final bending magnet, B20, placed with respect to the floor. This leads to results that cannot be interpreted by the $\sqrt{k}L$ values and the beam size at each quadrupole, as was attempted in the case of H2-VLE.

In order to understand this qualitative difference, Fig. 7.15 illustrates the results of Fig. 7.14, this time right after Q22. In Fig. 7.16, 1000 particles have been tracked along the H4-VLE beamline, simultaneously indicating the $\sqrt{k}L$ values of each quadrupole, and similar to H2-VLE, the observed results can be interpreted.

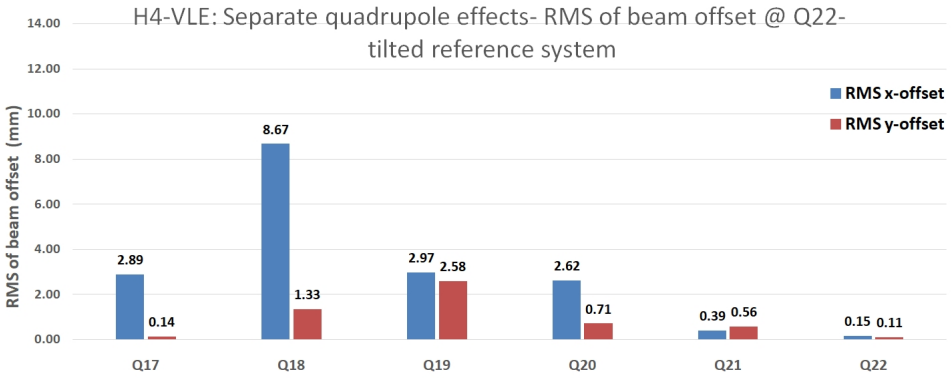

Figure 7.15: *Beam offset after Q22 with respect to the tilted plane due to separate transverse quadrupole misalignments for H4-VLE having a standard deviation 0.5 mm.*

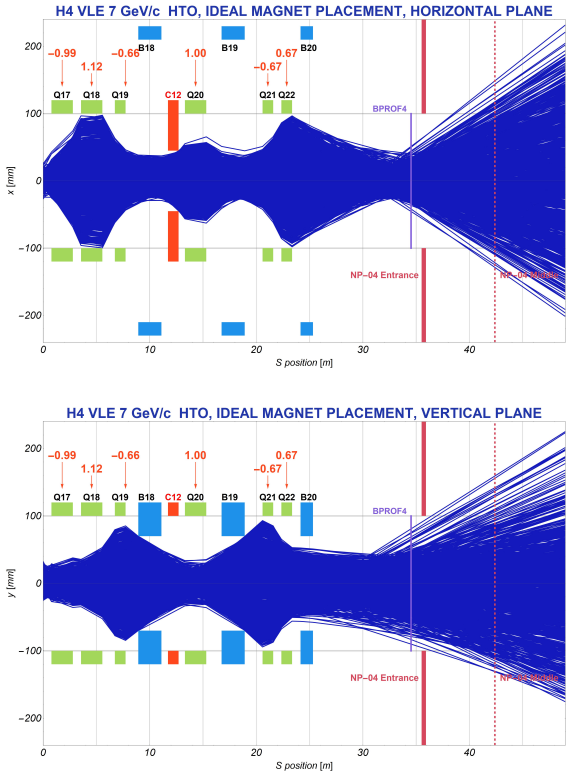

Figure 7.16: *Tracking of 1000 particles along the H4-VLE beamline, having placed the magnets in their ideal positions.*

To conclude, misalignments of the quadrupole triplet lead to significant losses, while misalignments of the final focusing doublet lead to beam offsets at BPROF4.

Finally, the expected beam profiles at the four monitors of H4-VLE, in cases where a specific quadrupole has been misaligned have been studied. The placement of these monitors can be found in Fig. 4.5, and specifically, BPROF1 is placed before B19, while BPROF2 and BPROF3 after it. BPROF4 is placed right before the entrance of the cryostat.

Similar to H2-VLE, the first three monitors are placed parallel to the magnetic elements ($\sim 57°$), while BPROF4 is placed with respect to the floor of EHN1.

Fig. 7.17a shows the expected profiles along the H4-VLE beamline in the case that Q18 has been misaligned by 1 mm along the horizontal (tilted) reference system. At BPROF3, the deviation of the ideal and misaligned horizontal profiles is $\sim$5 mm, justified by the large beam size at the position of Q18 combined with its $\sqrt{k}L$ value, while at BPROF4 this deviation is less than 1 mm in both planes. Therefore, if Q18 is misaligned horizontally, a beam offset is expected at BPROF3, but not at BPROF4, due to the final steering dipole, B20.

In Fig. 7.17b Q19 has been misaligned by 1 mm in the vertical (tilted) plane. At BPROF3, the expected deviation of the vertical profile is $\sim$6 mm, due to the large vertical beam envelope at Q19. Similarly, at BPROF4, the deviation does not exceed 1 mm in each plane.

Finally, in Fig. 7.18a Q21 is misaligned by $\Delta y = 1$ mm and in Fig. 7.18b Q22 is misaligned by $\Delta x = 1$ mm. Despite their small $\sqrt{k}L$ values, and their proximity to the experiment, considerable beam offsets are expected at BPROF4. Specifically in case 7.18a the expected deviation is $\sim$8 mm in the horizontal and $\sim$5 mm in the vertical plane, while in case 7.18b it is $\sim$3 mm in the horizontal and $\sim$4 mm in the vertical plane.

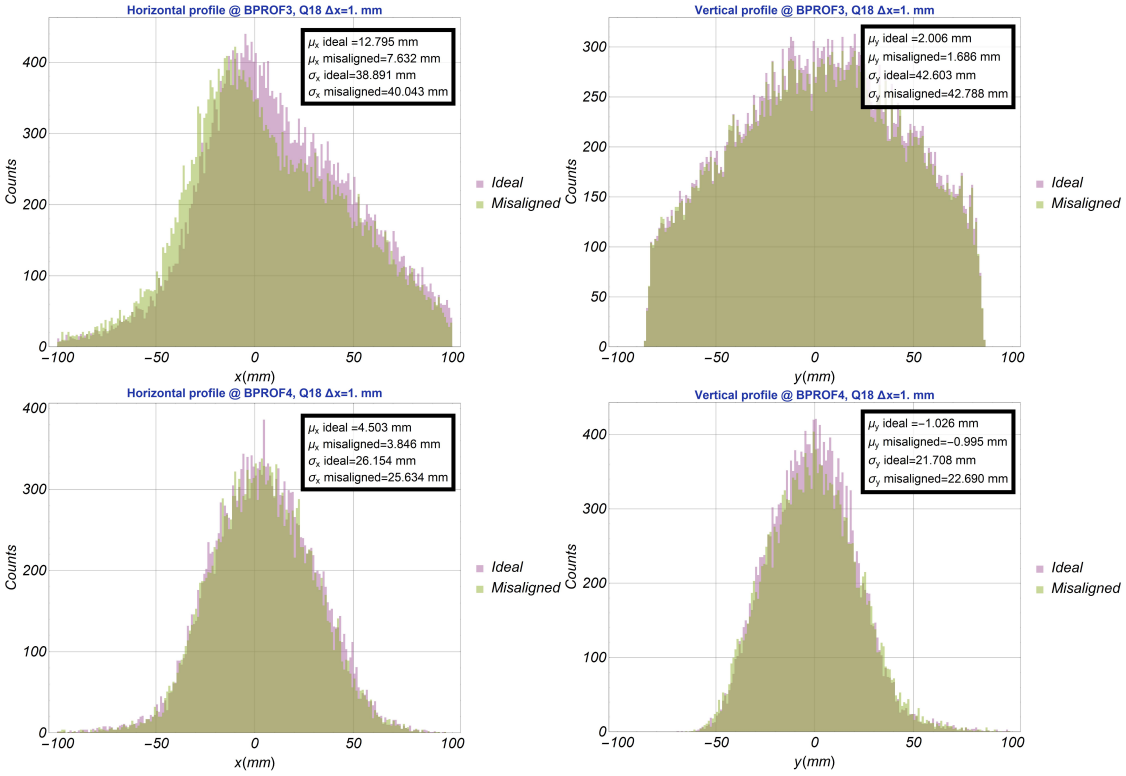

(a) *Misalignment of Q18 by* $\Delta x = 1\,mm$

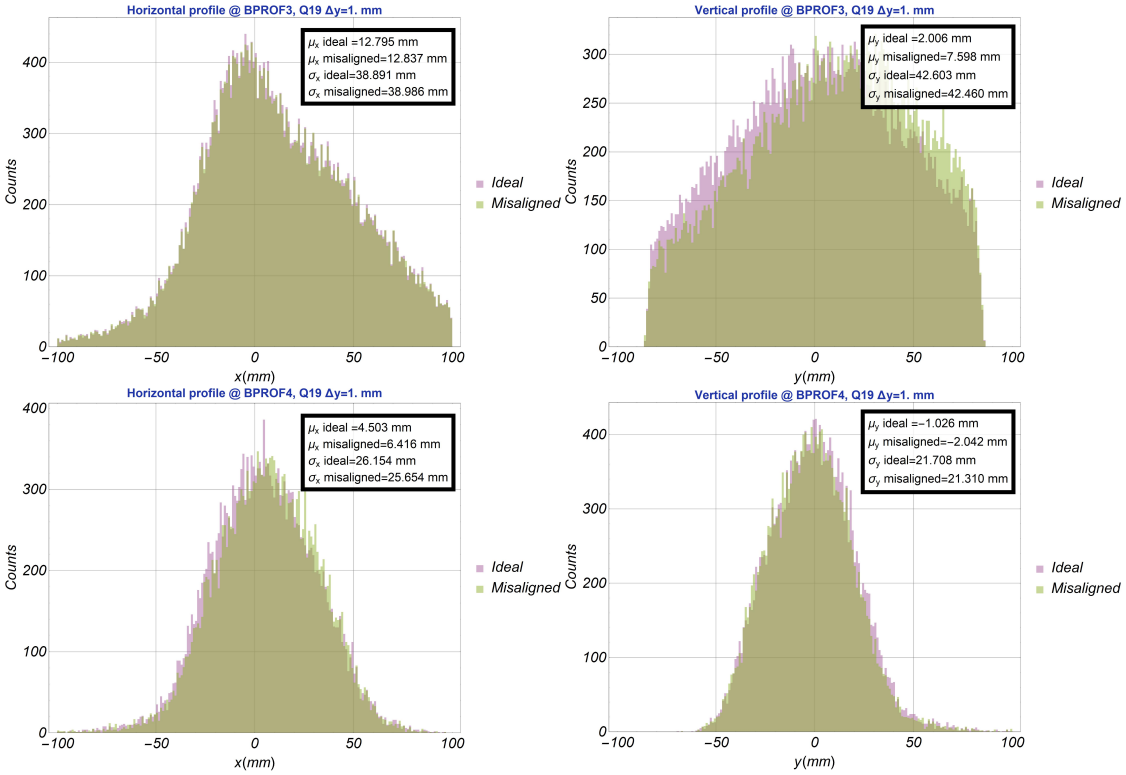

(b) *Misalignment of Q19 by* $\Delta y = 1\,mm$

Figure 7.17: *Expected profiles at BPROF3 and BPROF4 of H4-VLE, for the ideal and misaligned magnet placement.*

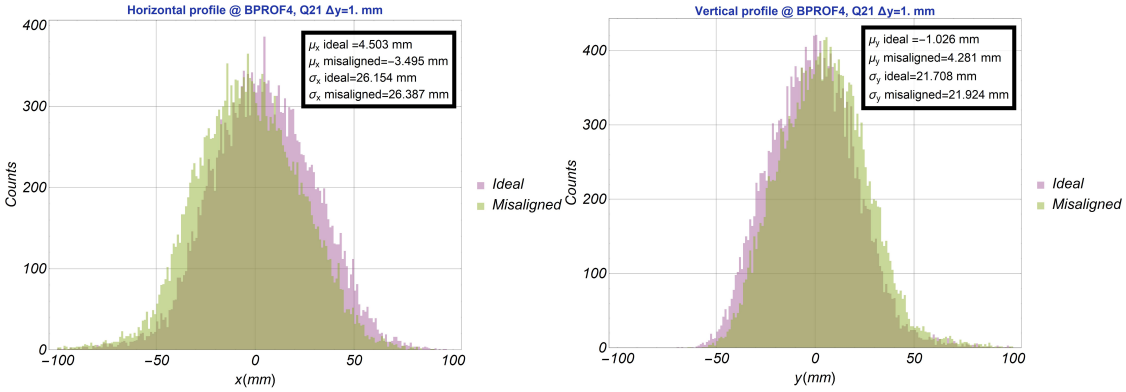

(a) *Misalignment of Q21 by* $\Delta y = 1\,mm$

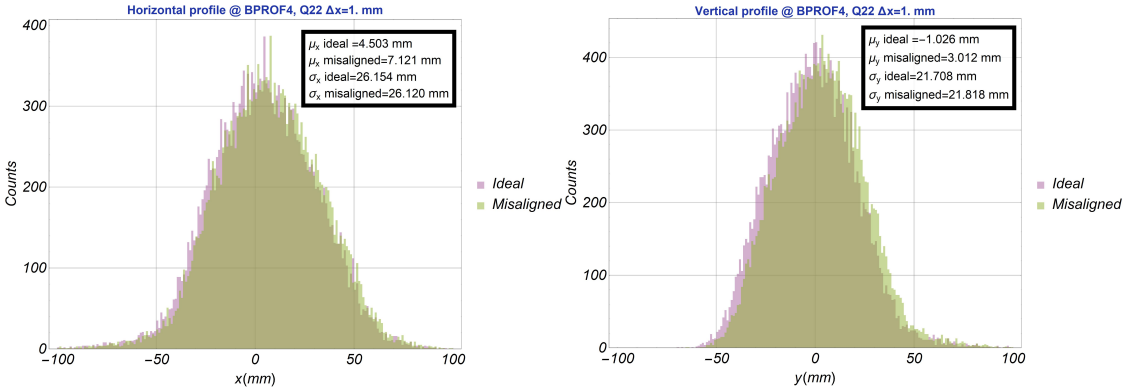

(b) *Misalignment of Q22 by* $\Delta x = 1\,mm$

Figure 7.18: *Expected profiles at BPROF4, for the ideal and misaligned magnet placement.*

Part II

Efficiency measurement and ToF demonstration of novel SciFi detectors in the East Hall

CHAPTER 8

Development of SciFi detectors: motivation and principle of operation

This chapter discusses the instrumentation needs of the VLE beamlines of the Neutrino Platform Project, necessitating the development and integration of new detector technologies, that will also potentially substitute the instrumentation of other beamlines in the future. The principle of operation of these novel detectors is explained.

8.1 Instrumentation requirements of the new VLE beamlines

The VLE beamlines will be instrumented with detectors crucial for the beam tuning and also providing particle by particle information, useful for the event reconstruction of NP-02 and NP-04. Particularly, due to the rather low event rate, the beamline detectors will provide each particle's entrance position and angle, its type and momentum, the latter with a resolution finer than the expected $\sim$5% momentum spread with the collimator at its full opening.

Specifically, the proposed instrumentation for the VLE beamlines is:

- **Beam profile monitors**, providing:

  - Beam profiles at various positions along the two beamlines, necessary for the beam tuning

  - Position and angle of incidence of each particle at each cryostat

  - Precise momentum measurement

- **Three scintillator counters**, providing:

  - General trigger signals for the beamline instrumentation

  - Time-of-Flight measurement

  - Intensity information

- **Two Threshold Cherenkov counters**, that, together with the ToF measurement will allow for particle tagging at the entire momentum range. [11]

The proposed beam instrumentation of H4-VLE is illustrated in Fig. 8.1, while similar instrumentation will be used for the H2-VLE beamline. The trigger detectors are colored with red. "TOF1" is placed between the quadrupoles Q18 and Q19 (not shown in the figure, but visible in 4.5), allowing for a ToF measurement over a distance of $\sim$29 m until "TOF2".

The profile monitors of the beamline are colored with green, each one providing the beam profile in one plane (either "X" or "Y" in the figure). The two final sets of profile detectors (namely "BPROFext" and "BPROF4") allow the determination of the position and angle of incidence of each particle at the NP-04 detector in both planes. The momentum spectrometer, comprising of three horizontal profile monitors designated "BPROF1", "BPROF2" and "BPROF3", one of them placed before B19 and two placed after it allows for momentum measurement, as discussed in [11].

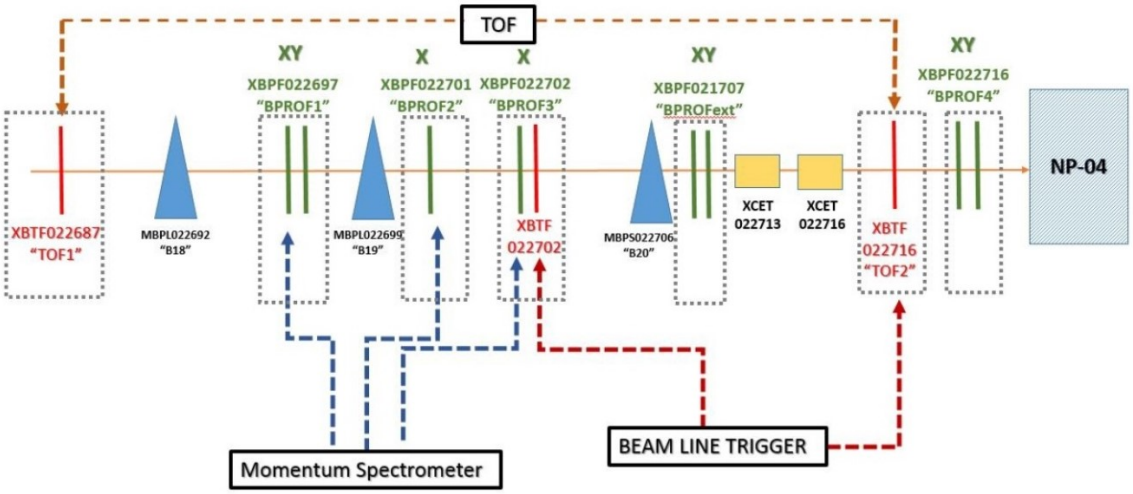

Figure 8.1: *Schematic layout of the H4-VLE beamline instrumentation.*

The crucial need to minimize the material budget, due to the low energy of the beamline particles, renders the use of common beam profile monitors and counters (Scintillation Paddles, Delay Wire Chambers [29] etc.) unsuitable due to the inability to be placed under vacuum.

Therefore the use of two newly designed detector prototypes, developed by the BE - BI Group of CERN in collaboration with the LPHE laboratory of EPFL, that can operate under vacuum, has been suggested for the two beamlines [30]. Both detectors are Scintillating Fiber ("SciFi") detectors, fabricated with the same active material, that can cover a large active area of 200x200 mm^2, sufficient for the expected beam size. One prototype can provide quick pulses necessary for trigger signals, while the other will track individual particles, their difference lying in the photodetection mechanism. The two aforementioned detector prototypes will be used in the two beamlines as the necessary trigger detectors and beam profile monitors, respectively.

8.2 SciFi detector prototype principle of operation

A SciFi detector consists of a series of parallel fibers composed of a scintillating material, each one covered by a thin layer of a material of low refractive index. A transversing particle will excite the scintillator, therefore producing light that, through total internal reflection inside the fiber will be guided to a photomultiplier mounted at one end, allowing for the light detection.

8.2.1 Scintillation Mechanism

Organic and inorganic materials can be used as the fiber core, however Polystyrene has been preferred in this detector type. Polystyrene is an organic material, and therefore, like all organic materials, the fluorescence process is achieved by transitions in the energy level structure of its molecule. The energy levels of Polystyrene are shown in Fig. 8.2, the S_0, S_1, S_2 etc. states corresponding to singlet states (S=0), while the T_1, T_2 to triplet states (S=1). Illustrated with dashed lines are the vibrational molecule levels.

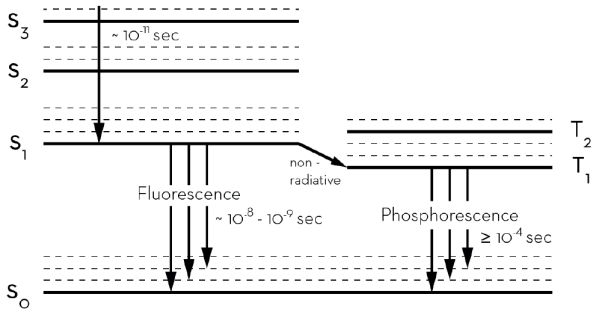

Figure 8.2: *Polystyrene energy levels and possible electronic transitions.*

Excitation of the molecule to the higher singlet states is quickly de-excited to S_1 via radiationless internal conversion, the process lasting $\sim 10^{-11}$ s. Moreover, any additional vibrational energy state above the S_1 state is quickly de-excited to S_1. De-excitation to the S_0 ground state (or one of its vibrational levels) has a typical lifetime of 10^{-8} s, considerably longer than the aforementioned transitions. Finally, an occupied triplet state will be de-excited in lifetimes of 10^{-4} s, and therefore delayed light is produced, in a mechanism referred to as "phosphorescence".

Due to its opacity to its own emitted light, the polystyrene matrix is doped with a fluorescent dye that absorbs the emitted light and re-emits it in larger wavelengths. This wavelength shift at the same time increases the efficiency of the photocathode (when a photomultiplier tube is used for the light detection), because of its sensitivity to larger wavelengths.

8.2.2 Fiber Optics

The scintillation material is fabricated as small cylindrical or square fibers, covered by a cladding of plexiglass [31]. Photons generated by a transversing particle will reach the boundary, and will be either reflected at the surface or refracted to the cladding

(Fig. 8.3), depending on the angle of incidence and the refractive indices of the two media.

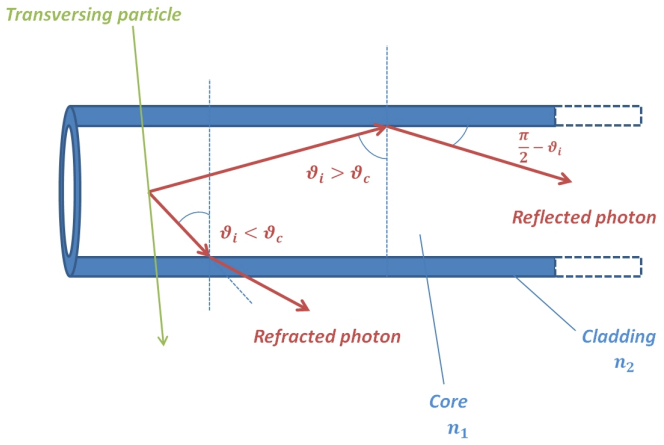

Figure 8.3: *Reflection or refraction of the generated photon inside the fiber active material.*

The critical angle of incidence, above which total internal reflection occurs (and no refraction) can be calculated via Snell's law, requiring that the refraction angle is $\theta_f = \pi/2$, and therefore:

$$\theta_c = arcsin\left(\frac{n_2}{n_1}\right) \tag{8.1}$$

where n_1 is the core refractive index, while n_2 that of the cladding. With refractive indices of the Polystyrene being $n_1 = 1.6$ and that of plexiglass $n_2 = 1.49$, the critical angle of the above configuration is $\sim$21°. [31]

8.3 SciFi detector photodetection

Two SciFi detector types have been constructed, each one consisting of 192 fibers of 1 mm thickness in parallel, closely stacked together in a total active area of 200x200 mm^2. If the generated photons of the separate fibers are all detected using a single photodetector, then the designed SciFi detector operates as a counter detector. If each fiber is mounted to a separate photodetector, then the particle position can also be measured.

The former detector type, designated "XSCINT", is shown in Fig. 8.4a, while the later, named "XBPF", is shown in 8.4b. For both detector types, the other fiber end is glued on a high-reflectivity mirror, decreasing the percentage of escaping photons.

The estimated light yield for a MIP particle impinging on a single fiber of 1 mm thickness and 50 cm length has been calculated in [31] as approximately 15 - 20 photons. This light yield imposes that the photodetector mounted to the fibers be sensitive to low light levels.

8.3.1 XSCINT

The photodetector of the XSCINT prototype is a typical photomultiplier tube (illustrated in Fig. 8.5) with a bi-alkali photocathode ([33]), the operation principle of which

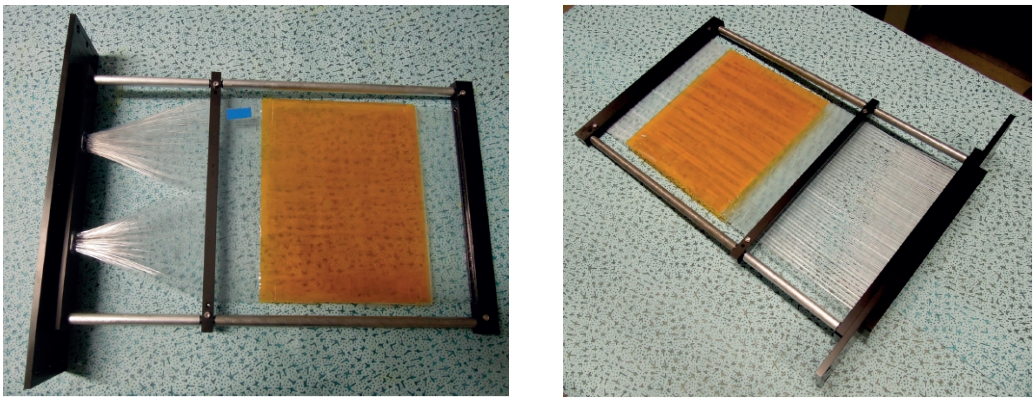

(a) *XSCINT* **(b)** *XBPF*

Figure 8.4: *XSCINT (a) and XBPF (b) prototypes*

can be found in common textbooks such as [32].

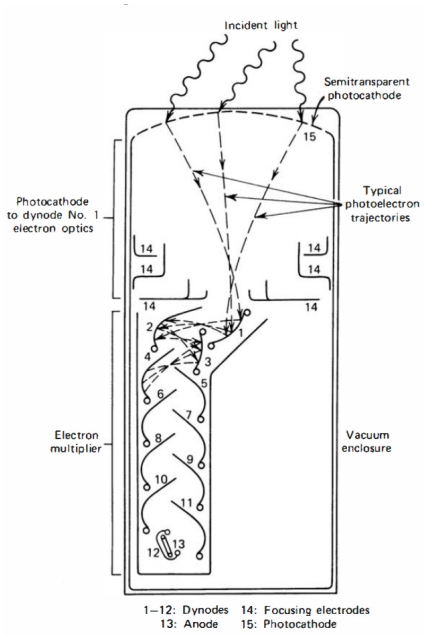

Figure 8.5: *A typical photomultiplier tube [32].*

In short, an impinging on the photocathode photon (generated in the scintillator, therefore of wavelength in the visible or near the visible region) will interact with the metal via the photoelectric effect, this interaction mechanism being the dominant for the specific photon energy. The generated photoelectron, after inelastic collisions with the electrons of the metal will reach the surface, and can escape it, if its kinetic energy is sufficient to overcome the metal - vacuum potential. This probability, determined by the initial photon energy, the photocathode material and its width, defines the quantum efficiency of the photomultiplier tube, which is 43% for the specific bi-alkali photocath-

ode. The escaping photoelectron is accelerated towards the first dynode, held at a positive potential of several hundred volts, causing ionization. In their turn, the escaping from the first anode electrons will further be accelerated in the second dynode due to the applied potential, and via a series of dynodes the initial photoelectron will result in a detectable current.

The spread in transit time of the particular PMT model ([33]) is very sharp ($\sim$0.3 ns) potentially allowing for high resolution ToF measurements, as will be analyzed in Section 9.5 .

As shown in Fig. 8.4a, to reduce the excessive mechanical stress of the fibers, rather than using a single PMT for the entire detector, two PMTs are preferred, each one mounted to half of the fibers.

8.3.2 XBPF

To measure the transverse particle position, in the XBPF prototype each fiber is mounted to an individual photodetector. Each photodetector is a Silicon Photomultiplier (SiPM), which is a matrix of Geiger-Mode Avalanche Photodiode (G-APD) cells.

A G-APD, illustrated in Fig. 8.6, is a photodiode (a complex p-n junction) where a reverse voltage above the breakdown is applied.

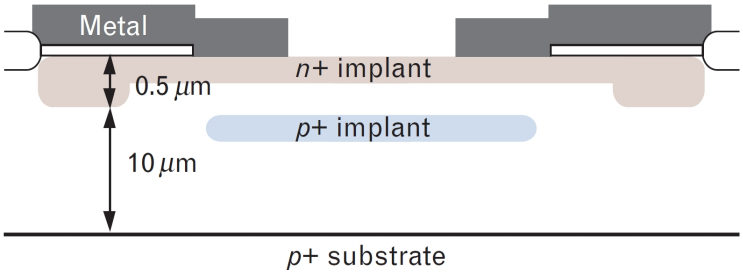

Figure 8.6: *A typical G-APD [34].*

In a p-n junction, electrons from the n-type semiconductor are able to diffuse to the p-type due to the concentration derivative, and therefore re-combine with its excess holes, while at the same time holes of the p-type will migrate to the n-type region. This charge migration depletes the boundary region on each side from majority carriers, and results in a contact potential in the boundary region (referred to as the "depletion region"), that prevents any further diffusion. However, if additional energy (either by an impinging photon or by thermal motion) is provided to one of the valence electrons of the depletion region, the equilibrium is disturbed and the conduction electron will drift, due to the contact potential, to the n-side, while at the same time the hole to the p-side. Electron-holes pairs created outside the depletion region, due to the lack of electric field, are most likely quickly recombined.

When a p-n junction is reverse biased (the positive voltage is applied to the n-side), the minority carriers from both sides will diffuse towards the depletion region, widening it and at the same time increasing the potential barrier, therefore there is a resistance

to the flow of charge carriers. Due to the increased electric field, a valence electron excited by the aforementioned means to the conduction zone will be accelerated and, if the electric field is high enough for it to gain a kinetic energy above the material band gap, its collision with another electron-hole pair can ionize the latter. This process results to an avalanche of electrons that can be detected.

While the resistance will increase with an increasing bias voltage, beyond a critical level the diode will "break down", causing an abrupt reverse current increase. When a photodiode is applied such voltage, it is referred to as operating in Geiger mode.

Beyond this critical applied voltage, the electrons and holes are multiplying faster than can be extracted. To quench this avalanche, a resistor is used. Since the output signal is not proportional to the input, the G-APD is practically a digital device, which switches from "off" to "on" when a single photon is detected.

The SiPM is an array of the aforementioned G-APD cells, each one having dimensions of tens of microns, so that it is practically very unlikely that a single cell will be hit by two photons at the same scintillation pulse. Each G-APD is connected in series with a resistor, to quench the generated avalanches.

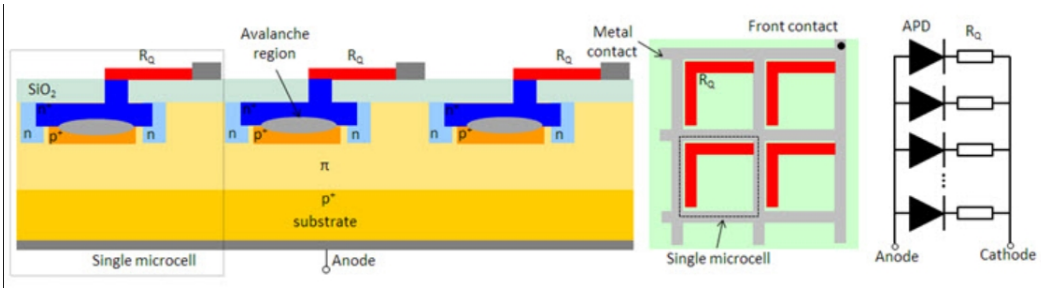

Figure 8.7: *Schematic illustration of a SiPM [35].*

8.4 Additional characteristics

In the particular fiber model used for both SciFi detector prototypes, each fiber is square with 200 mm height and 1 mm width, while the cladding covers 0.02 mm in each fiber side. The cladding does not scintillate, and therefore is considered as a "dead" area, reducing the detector efficiency. Therefore, the theoretically maximum efficiency of both the trigger and the beam profile monitors is calculated as 96%, which is referred to as its "Geometrical Efficiency".

Another important characteristic of the fiber detectors is a phenomenon cited as "Optical Cross - talk". An escaping photon from a specific fiber can be trapped inside a neighboring fiber, therefore compromising the spatial resolution of the profile monitors. To suppress this, it is common to cover the fibers with an ultra-thin aluminum coating, reflecting the primary photons.

Apart from these characteristics, the scintillator is sensitive to π, K, p e and μ of both polarities in the momentum range of interest and has lower material budget compared to other detection options initially investigated (for example GEMs, MicroMegas etc.).

Additionally, the prototypes are radiation resistant and have a simple maintenance, since no gas or cooling systems are required for their performance.

CHAPTER 9

Efficiency and multiplicity measurement of SciFi detectors

Since the exact behavior of the two detector prototypes described in Chapter 8 was unknown, a dedicated test was organized in order to study the characteristics of both modules in the T10 test beam of the East Hall during the final week of November 2017. In particular, the efficiency and multiplicity of the beam profile monitor have been measured in various beam conditions, and the feasibility of the trigger detectors as Time of Flight modules was demonstrated. This chapter presents the setup and the read-out electronics of the experiment, as well as the data analysis and preliminary results.

9.1 The T10 test beam at the East Hall of CERN/PS

The T10 test beam, hosted at the East Hall of CERN, delivers secondary hadron beams of both polarities and of a 6 GeV/c maximum design momentum. A partial illustration of the East Hall, including the T10 beamline, is shown in Fig 9.1. The overall beamline length from the primary target (designated "NORTH Multitarget" in the figure) is $\sim$40 m, while the experimental zone covers only the last $\sim$15 m (designated "T10c").

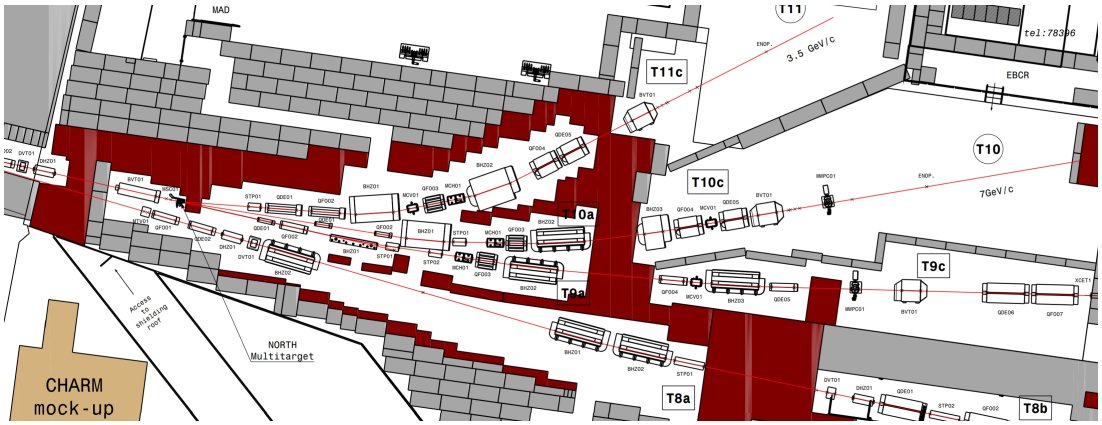

Figure 9.1: *Partial illustration of the East Hall. The T10 and T11 beams are entirely visible, while the T8 and T9 beams extend further downstream. [36]*

9.2 Experimental Setup

The setup of the SciFi experiment was installed in the T10 experimental zone of PS, as shown in Fig. 9.2. For reasons of flexibility in the placement of the detectors, and also allowing for the possibility to interchange (if needed) the trigger and the profile planes, a special holder - tank was constructed. Each one of the two tanks can hold up to two fiber planes (either profile or trigger modules). Two tanks were installed, each one containing one XSCINT and one XBPF detector, separated over a $\sim$13.5 m distance. The upstream XBPF is a horizontal profile monitor, while the downstream a vertical one. The setup is also schematically illustrated in Fig. 9.3.

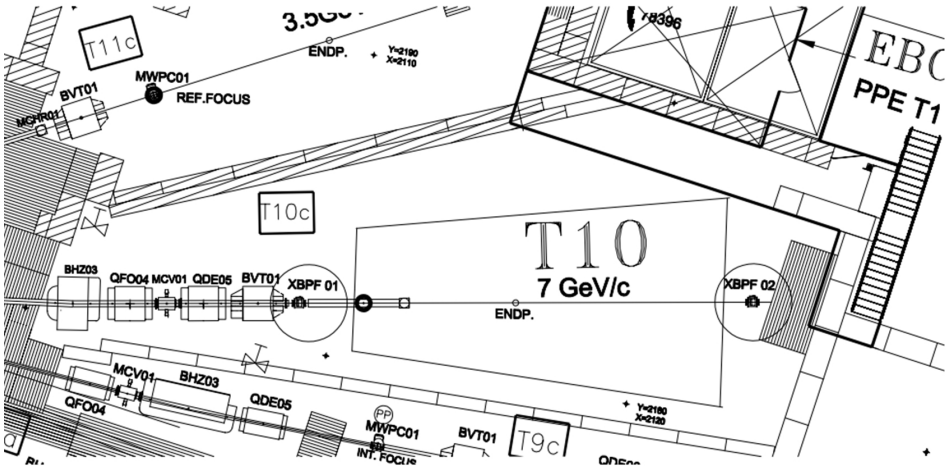

Figure 9.2: *The T10 experimental zone, including the installed monitors. [28]*

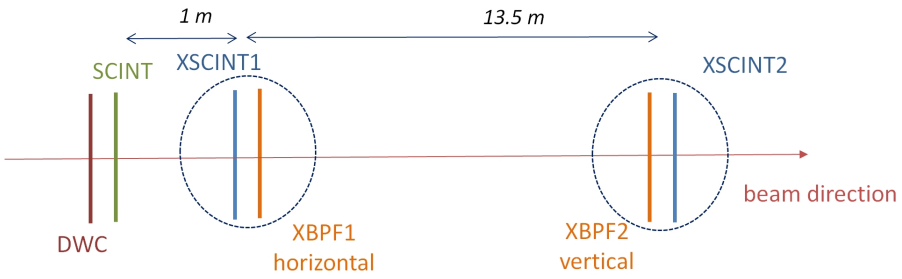

Figure 9.3: *Schematic presentation of the experimental setup.*

The upstream profile and trigger counter detectors will be referred to as "XBPF1" and "XSCINT1", while the downstream "XBPF2" and "XSCINT2" respectively. The setup is such that a particle traversing from both XSCINT1 and XSCINT2, will have certainly transversed from XBPF1 and XBPF2 as well.

In both profile monitors, half of the fibers have been covered with a thin aluminum coating, to test its impact to the fiber cross - talk, as explained in Section 8.4.

Apart from aforementioned detectors, the line was also equipped with a plastic scintillator mounted to a PMT (designated "SCINT" in Fig. 9.3), and a Delay Wire Chamber (designated "DWC") [29]. Both beam detectors cover an active area of 100x100 mm^2.

A photograph of the upstream tank, containing the first set of detectors, is shown in the left of Fig. 9.4a. The beam direction is from right to left, while the beam detectors can also be seen on the right side of the picture. The downstream tank is shown in Fig. 9.4b, where the front-end board connected to the XBPF is visible.

(a) *Upstream tank (containing XBPF1 and XSCINT1), Delay Wire Chamber and Scintillator (from left to right). The beam direction is from right to left.*

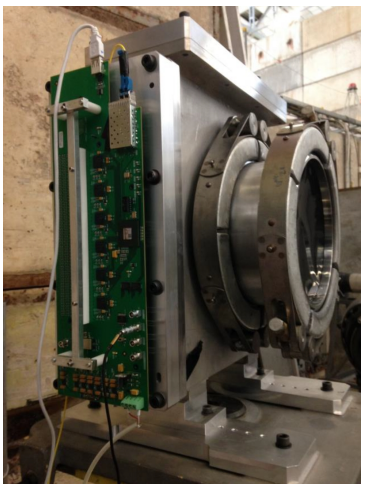

(b) *Downstream tank (containing XBPF2 and XSCINT2). The front end board mounted to the XBPF is shown.*

Figure 9.4

9.3 Read-out electronics and data format

The analog signals generated by the two trigger modules are connected to a Constant Fraction Discriminator (CFD). In the CFD a NIM pulse of 200 ns is generated when the input signal reaches a certain fraction of the peak value. The logic pulses of the two trigger modules arrive to a coincidence module, which has a 200 ns time window to account for the time difference due to the 13.5 m distance between XSCINT1 and XSCINT2. The coincidence pulse (if generated) is then converted to TTL and sent to the back-end board.

The XBPF's 192 SiPMs described in subsection 8.3.2 are connected to 6 CITIROC ASIC [37], each one having 32 input channels and 32 digital output channels, and therefore each SiPM is mounted to a separate channel. Via a leading edge discriminator, a TTL pulse is generated when the incoming SiPM pulse of a single fiber exceeds a preset threshold.

Every 100 ns, the front-end board of the XBPF sends to the back-end board the status of the 192 fibers (whether they scintillated in that time frame or not).

The VFC back-end board receives all the events from the profile monitors and also the external trigger from the trigger detectors, and assigns to each event and trigger a

time-stamp via White Rabbit (WR). The event with the closest timestamp is selected, provided that it lies within a 100 ns time window compared to the trigger timestamp.

The buffer of the VFC board is limited to 3276 trigger events. It is synchronized with SPS beam extraction signals, so that it is emptied right before the beam extraction, and therefore only events during the extraction are recorded. The data are extracted from the VFC board at each spill, and stored separately for each XBPF.

Each line in the stored data corresponds to a trigger signal, whether there was a corresponding event (signal in at least one of the 192 fibers) or not. For each trigger signal, the trigger timestamp as well as the event timestamp (the timestamp of the closest event) are recorded, both having the WR precision (8 ns).

Additionally, for every trigger event, the CITIROC chips mounted to the SiPMs provide information about the specific fibers that scintillated within the 100 ns time window, the first chip providing information about fibers 1 - 32, the second about fibers 33 - 64 and so on. In particular, each one of the six chips provides a number that, when converted to binary, is a series of 32 digits of 0 and 1, the former denoting the absence of a signal in the particular fiber while the latter its presence. Since the coincidence signal triggers the acquisition of both XBPFs, all the trigger signals recorded in XBPF1 are recorded in XBPF2 as well. The data format is also shown in Fig. 9.5.

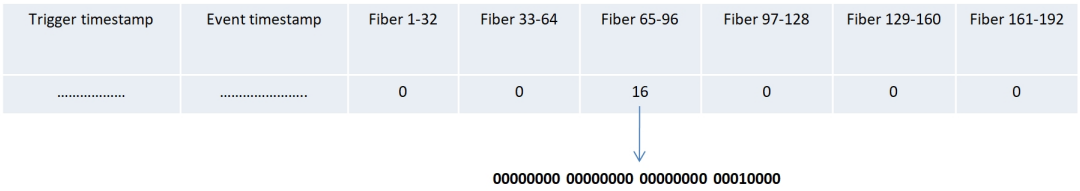

Figure 9.5: *Data format provided by the VFC board for the efficiency/multiplicity measurement of the XBPF prototype. By converting the last six numbers to binary, information about which of the 192 fibers scintillated is extracted.*

The two XSCINT modules will be additionally used for the Time of Flight measurement, due to the small spread in transit time of their mounted photomultiplier tube model (0.3 ns). A TDC (Time to Digital Converter) device with a sub-nanosecond time resolution compatible with the WR will timestamp the events. The analog signals generated by the two XSCINT, after the CFD module, are converted to TTL signals and travel to the TDC module, where they are flagged with a timestamp and saved in the buffer. The timestamps are saved separately for XSCINT1 and XSCINT2.

The described setup for the two measurements is presented in Fig. 9.6.

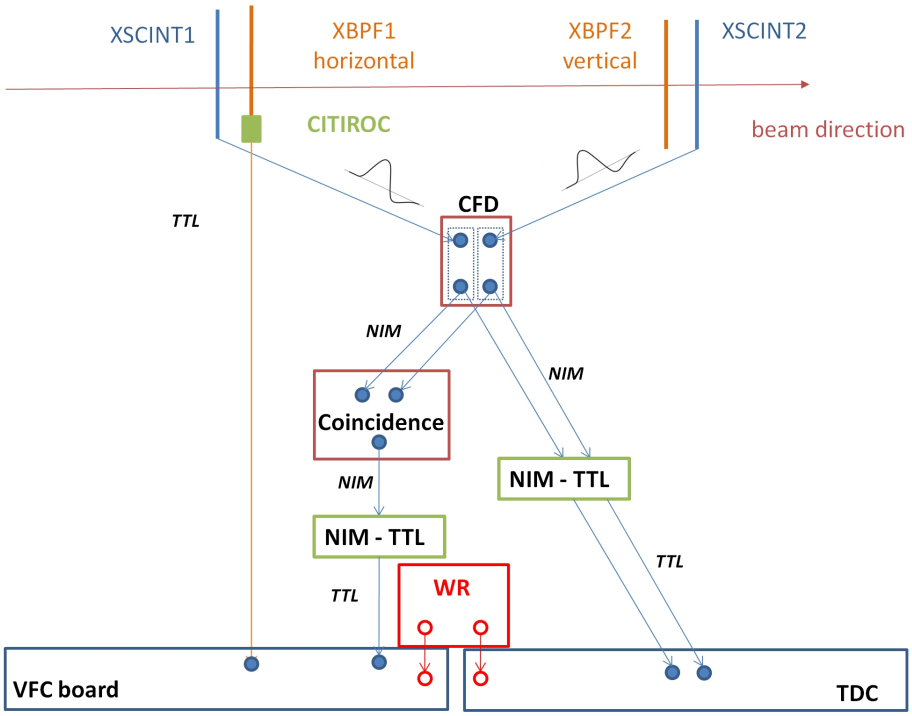

Figure 9.6: *Schematic presentation of the read out electronics for the efficiency/multiplicity measurement of the XBPF module (left) and the ToF measurement (right). The optical fiber connecting the XBPF front end board with the VFC board transfers the information about each SiPM separately. For simplicity, only the connection of XBPF1 is shown, while the connection of XBPF2 is identical.*

9.4 Efficiency and multiplicity measurement of XBPF module

Data were accumulated in various beam characteristics of the T10 beam to investigate the response of the profile monitor to a range of intensities, momenta and particle types. Specifically integrated intensities of $\sim 10^3 - 10^5$ particles/spill were tested in the case of the secondary hadron beam, with nominal momenta of either ± 6 GeV/c or ± 1 GeV/c. Lower intensity ($10^2 - 10^3$ particles/spill) muon beams were also available, with a maximum momentum of 6 GeV/c however a quite wide momentum spread, due to their production mechanism.

In order to increase the statistics, for each run, data from numerous spills were extracted, each spill having a maximum of 3276 trigger events.

9.4.1 Parameters of interest

The quantities of interest in each run (each different beam settings) for both profile monitors are the following:

- **XBPF efficiency**, defined as the percentage of events where at least one fiber scintillated with respect to the total trigger events.

- **Optical cross - talk**, defined as the number of events where two neighboring fibers scintillated, divided by the number of events where at least two fibers scintillated (neighboring or distant).
- **Fractional multiplicity**, defined as the number of events where at least two fibers scintillated, divided by the number of events where at least one fiber scintillated. The fractional multiplicity does not separate multiple particles from optical cross - talk.

For an integrated intensity of $\sim 10^4 - 10^5$ particles per spill, due to the limited buffer size, only the beginning of each spill is recorded. In Fig. 9.7 the timestamp data of a -6 GeV/c hadron beam of $\sim 10^5$ particles/spill are shown. The recorded spill duration is only ~ 0.07 s, corresponding to the beginning of the spill.

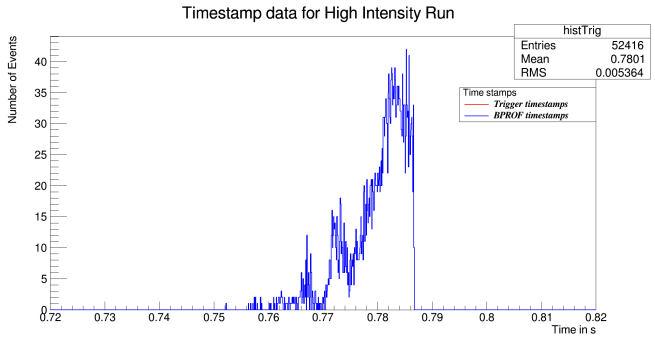

Figure 9.7: *Timestamps of a recorded spill for a -6 GeV/c hadron beam of $\sim 10^5$ particles/spill. Only the first part of the spill is recorded.*

By using a lower intensity -6 GeV/c muon beam the entire burst can be recorded, as illustrated in Fig. 9.8.

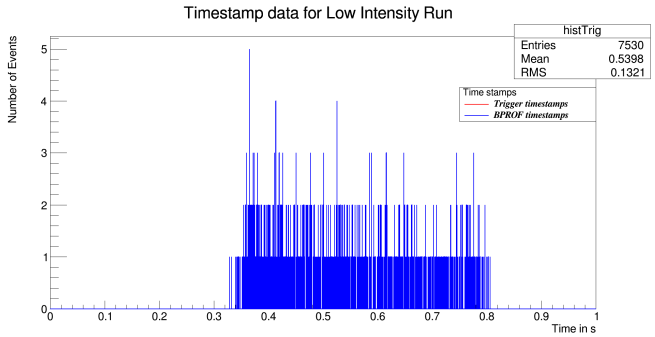

Figure 9.8: *Timestamps of the recorded data for a -6 GeV/c hadron beam of low intensity. The entire spill of ~ 0.5 s is recorded.*

9.4.2 Data analysis

Fig. 9.9 illustrates the reconstructed profile as measured at BPROF1 for a -6 GeV/c mixed hadron beam of 10^5 particles/spill. Data from 9 spills have been accumulated. Due to

an electronics malfunction, fiber n. 135 would always scintillate, and therefore channel 135 has been excluded from the analysis for XBPF1.

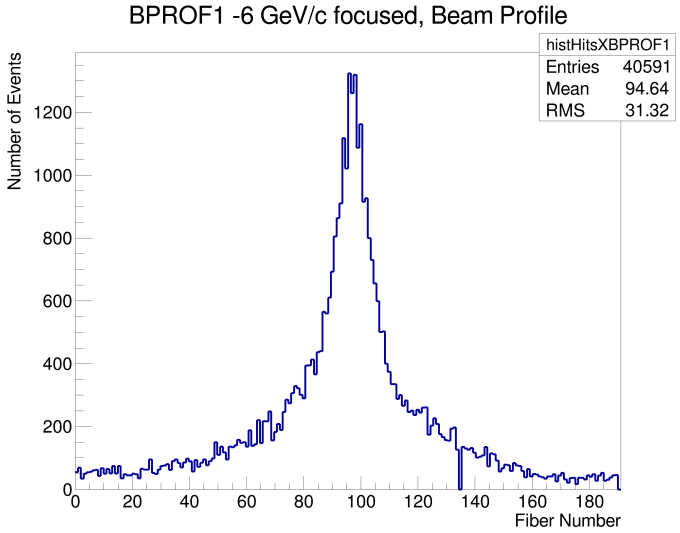

Figure 9.9: *Fiber profile of XBPF1 for a -6 GeV/c beam. Channel 135 has been excluded from the analysis, as described in the text.*

The measured efficiency, after rejecting channel 135, is $\epsilon = 95.8 \pm 0.3\%$, where the error corresponds to the standard deviation of the individual efficiency for each of the 9 spills. The measured efficiency is within the maximum theoretical geometrical efficiency.

In Fig. 9.10 the multiplicity analysis is shown for the same beam settings, separately for the aluminum coated fibers (A) and the clear (C) fibers.

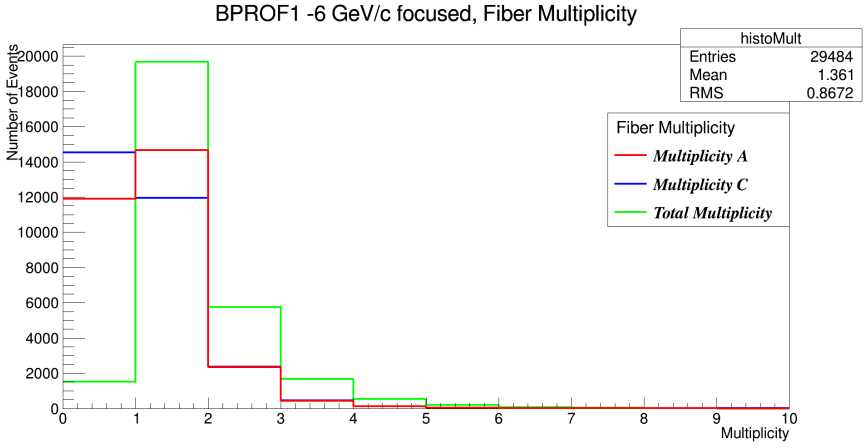

Figure 9.10: *Multiplicity analysis of XBPF1 for a beam momentum of -6 GeV/c.*

A multiplicity of 0 corresponds to the XBPF1 inefficiency. Multiplicity=1 corresponds to the number of events where only one fiber scintillated, multiplicity=2 in

events where two fibers scintillated etc. The fractional multiplicity, as defined in subsection 9.4.1, is $28 \pm 2\%$. This percentage of multiple scintillations can either be attributed to simultaneous particles, or optical cross - talk phenomena.

Finally, in cases where at least two fibers scintillated, the distance between these fibers has been calculated and is shown in Fig. 9.11 in a logarithmic scale. The probability that two neighboring fibers will scintillate (or the percentage of optical cross talk) corresponds to a $\sim$12% of the total events where at least two fibers scintillated. In cases where the distance is greater than two, the simultaneous scintillation is assigned to different particles. However, as will be explained in subsection 9.4.5, the probability of simultaneous particles is theoretically calculated to be much lower than the measured, and therefore the fiber span should further be investigated.

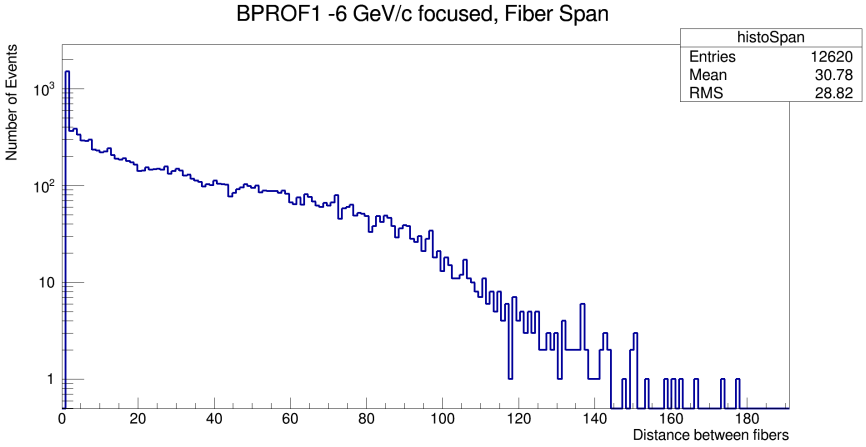

Figure 9.11: *Fiber span analysis of XBPF1 for a high intensity beam of -6 GeV/c.*

Figs. 9.12, 9.13 and 9.14 summarize the results obtained in various beam settings for XBPF1. The first run, denoted "-6 GeV/c", corresponds to the already shown run of Figs. 9.9, 9.10 and 9.11.

In the second run ("-6 GeV/c unfocused"), the beam size is enlarged by changing the quadrupole currents, the transverse profile of which is shown in Fig. 9.15. The calculated efficiency in this case is within the statistical error of the previous measurement, and specifically $\epsilon = 95 \pm 0.6\%$. All other parameters (fractional multiplicity, optical cross - talk) are identical, and therefore it can be inferred that the XBPF performance does not depend on the focusing of the beam.

By changing the beam polarity, and refocusing the beam similary to the initial configuration of Fig. 9.9, there is a significant drop in the efficiency. However, by investigating each spill separately, it was found that the efficiency was not systematically reduced, but rather, there were spills with the maximum efficiency of $\sim$96% and spills with a significantly lower efficiency of $\sim$81%, resulting in a large error, as shown in Fig. 9.12- "6 GeV/c ". This behavior has not been fully understood, but most likely is a buffer issue.

The above assumption is further strengthened by investigating the performance of

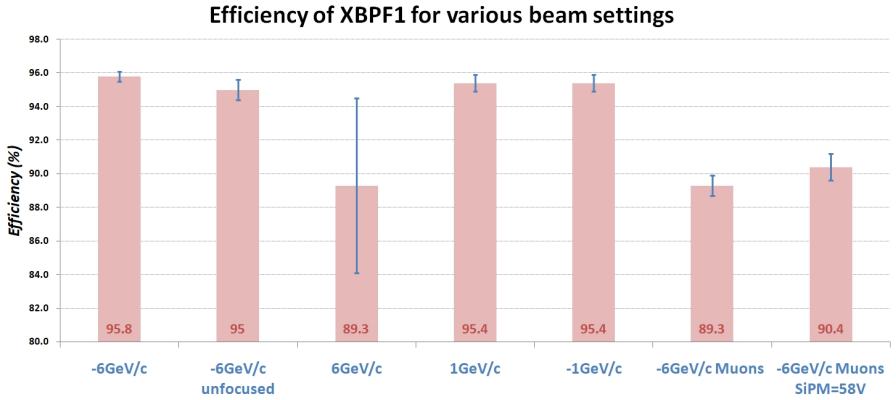

Figure 9.12: *Efficiency of XBPF1 for various settings of the T10 beam.*

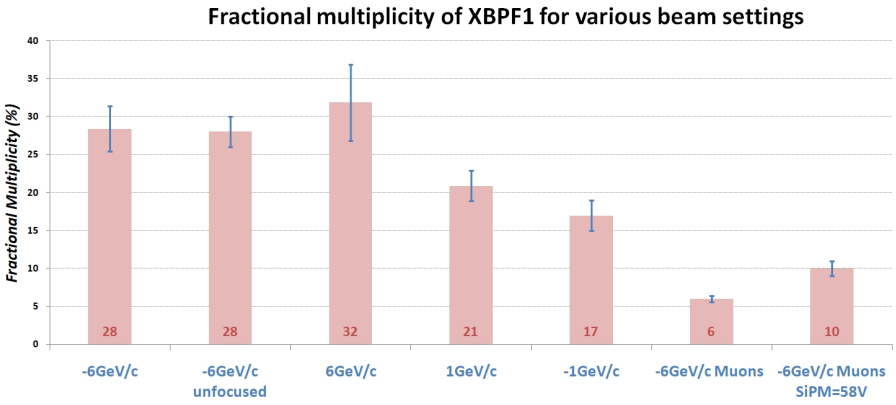

Figure 9.13: *Fractional multiplicity of XBPF1 for various settings of the T10 beam.*

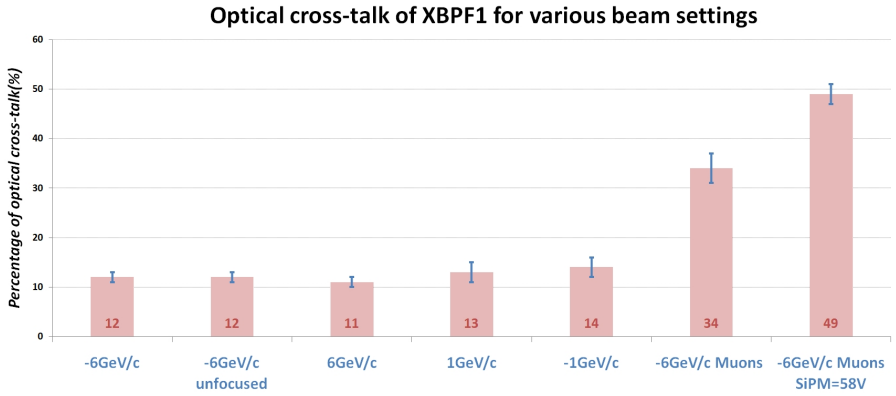

Figure 9.14: *Optical cross - talk of XBPF1 for various settings of the T10 beam.*

the module to a ± 1 GeV/c beam. As would be expected, the response of the scintillator should not depend on the polarity of the impinging beam, and in particular has been measured $\epsilon = 95.4 \pm 0.5\%$ for both polarities. Additionally, all other parameters are

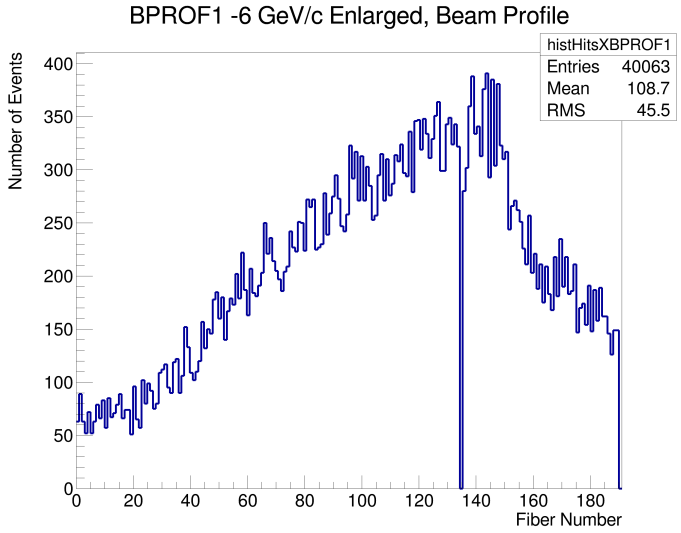

Figure 9.15: *Measured beam profile at XBPF1 for an enlarged beam of -6 GeV/c. Fiber 135 has been excluded in the analysis.*

within the statistical error.

Finally, a relatively pure low intensity muon beam of -6 GeV/c maximum momentum reached the setup, the profile of which is shown in Fig. 9.16 . In contrast to all

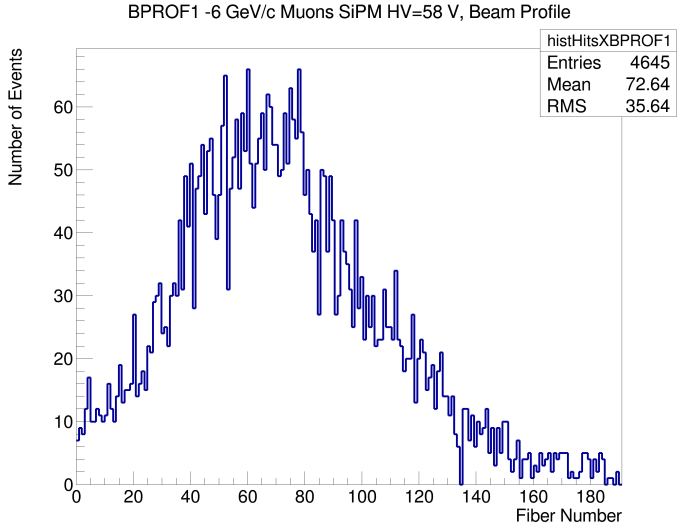

Figure 9.16: *Measured beam profile at XBPF1 for an muon beam of -6 GeV/c maximum momentum. Fiber 135 has been excluded in the analysis.*

previous cases, due to the low event rate, the entire spill has been recorded. Fig. 9.12 shows that the efficiency of XBPF1 is systematically reduced to $\sim 89.3 \pm 0.6\%$ ("-6 GeV/c muons"), and does not increase by fine-tuning the SiPM high voltage ("-6 GeV/c muons SiPM=58V"). As would be expected, the fractional multiplicity is considerably reduced,

since the probability of simultaneous particles becomes even smaller. For the same reason, the percentage of optical cross - talk events increases. This is also shown in Fig. 9.17, in contrast with the Fiber span obtained in high intensity runs, as in Fig. 9.11.

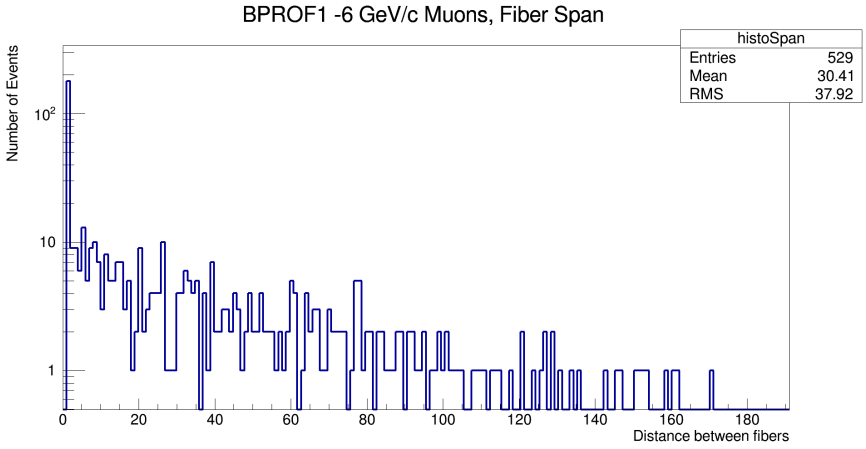

Figure 9.17: *Measured fiber span at XBPF1 for a low intensity muon beam of -6 GeV/c maximum momentum. The percentage of neighboring signals is significantly higher than in the high intensity runs.*

9.4.3 Comparison with DWC profile

In Fig. 9.18 the profiles provided by the DWC (up) and XBPF1 (down) are shown for the same beam settings. The two detectors are only $\sim$1 m apart and therefore a qualitative comparison can be performed. Since the DWC covers an area of 100x100 mm^2, only the central part of the XBPF1 profile is shown, corresponding to fibers 48-144.

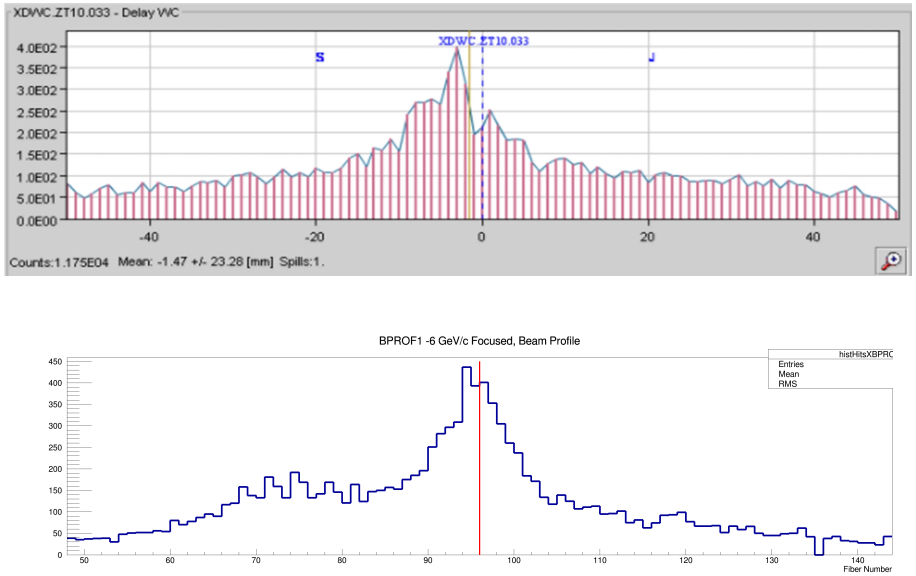

Figure 9.18: *Comparison between the profiles provided by the DWC (up) and XBPF1 (down).*

9.4.4 Timestamp issues

Since the trigger signal is common for both XBPFs, each recorded trigger signal in XBPF1 is also recorded in XBPF2. In other words, for a particular spill, the first line of data of XBPF1 (or the first trigger signal) corresponds to the first line of data of XBPF2. Therefore a direct comparison of the trigger signals recorded in each XBPF is possible, the time differences of which are plotted at the top of Fig. 9.19, showing a $\sim$80 ns constant delay. It should be reminded that the WR time resolution is 8 ns and therefore some time differences can be 72 ns or 88 ns as well. This constant delay is due to the electronics and can be rejected in the analysis. At the bottom of the same figure, the timestamp differences between XBPF1 and the trigger signal, as well as XBPF2 and the trigger signal have been plotted. As was expected, there is a 100 ns spread between each event and the corresponding trigger.

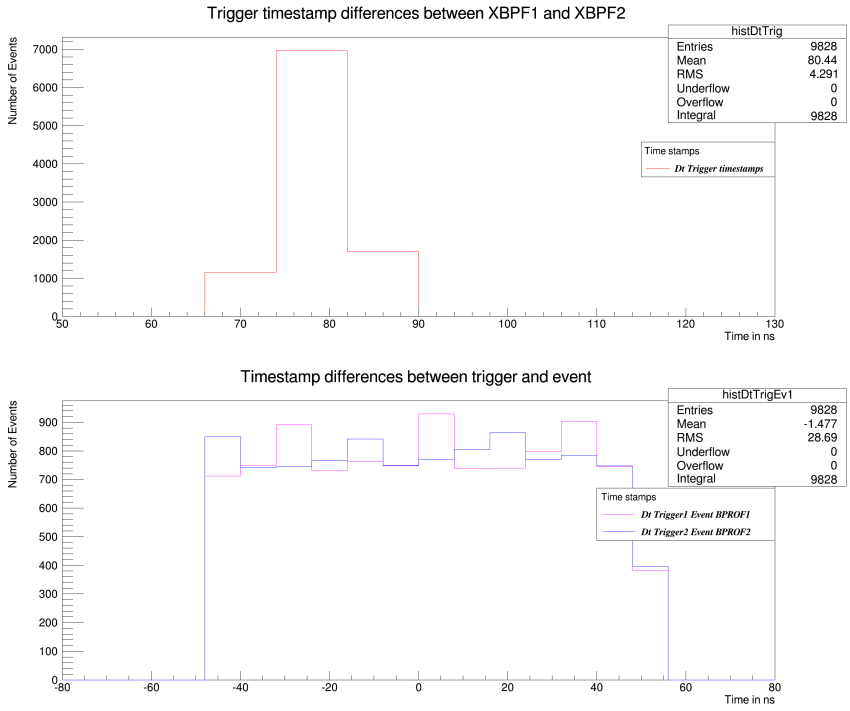

Figure 9.19: *Expected time differences between the trigger timestamps recorded in the two XBPFs, and between the event timestamp and the trigger timestamp for each XBPF.*

However, in some files either the time difference between two trigger timestamps, or the time difference between a trigger timestamp and the corresponding event can be as high as 10^6 ns, which indicates a malfunction of the buffer. These events have been excluded in the previous analysis.

This problematic behavior has been linked with the density of the recorded events, and specifically, if this density is high enough, the buffer seems to crash. This is illustrated in Fig. 9.20, where a high intensity -6 GeV/c hadron beam has been recorded for 12 subsequent bursts. The histogram binning is 0.1 ms. Whenever the density of events

exceeds a value of around 50 events/0.1 ms, either the trigger timestamps recorded in XBPF1 and XBPF2 have large time differences of $\sim 10^6$ ns, or similar time differences are observed between the XBPF event timestamp and the recorded trigger timestamp.

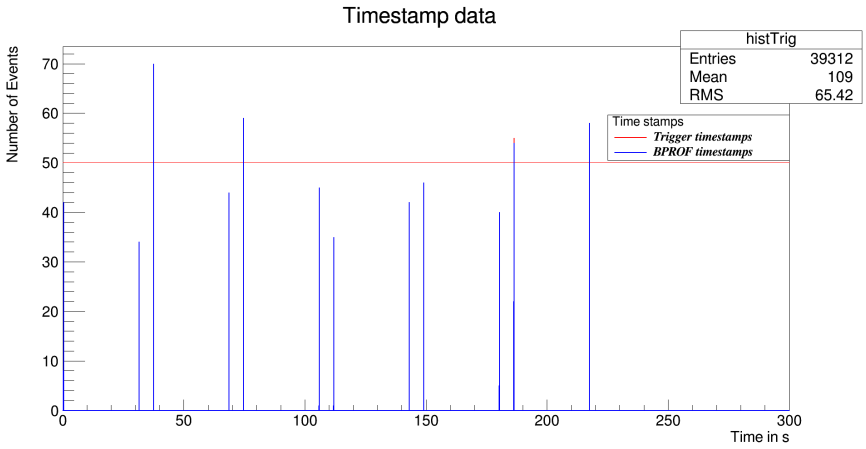

Figure 9.20: *Recorded spills for a high intensity -6 GeV/c hadron beam. Spills n. 3, 5, 11 and 12 are corrupt, after reaching a density of more than ∼50 events/0.1 ms.*

Fig. 9.21a shows the first spill of Fig. 9.20. The density of events is relatively low, and therefore the timestamps are consistent with the expected of Fig. 9.19. However, in Fig. 9.21b the third spill of Fig. 9.20 is shown, where the aforementioned maximum density of events is exceeded. After this density reaches a certain value, there is an immediate drop in the rate of the recorded events (as shown in the "tail" of the figure) which is completely non-physical. Additionally, the data recorded after this point show significant timestamp differences between trigger and event, of the order of 10^6 ns.

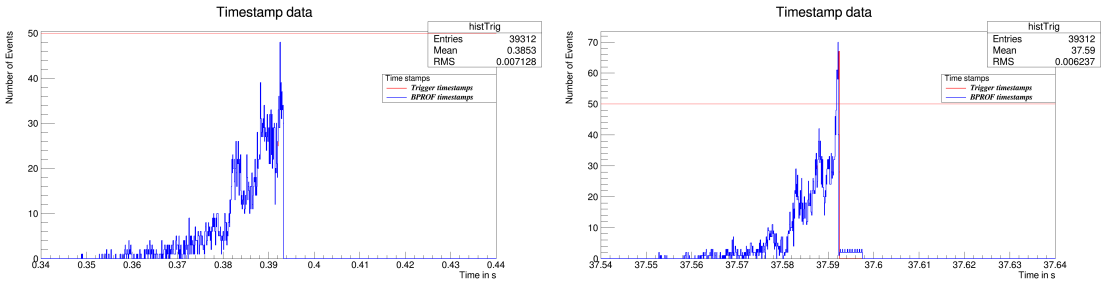

(a) *Timestamps of the first spill of Fig. 9.20.* **(b)** *Timestamps of the third spill of Fig. 9.20.*

Figure 9.21

9.4.5 Conclusions and outlook

It has been shown that the XBPF module can perform excellently in terms of efficiency in hadron beams of high intensity of ± 6 GeV/c and ± 1 GeV/c, irrespective of the beam focusing. The drop in the efficiency for the -6 GeV/c measurement can be with relative safety assigned to a buffer issue.

Quite alarming is the systematic efficiency drop of the XBPF for muon beams. This drop cannot be explained physics - wise, since all muons (as well as hadrons) in this energy range are Minimum Ionizing Particles. This response of the XBPF is not a result of the rather unfocused muon profile either, since the efficiency has been proved to be independent of the beam focusing. It could however be a result of the low intensity of the muon beam. A low-intensity hadron beam was tuned in one of the runs, and the efficiency was measured to be $88.4 \pm 0.5\%$ but, due to the low statistics acquired, it was not possible to safely infer that the efficiency decrease is linked to the low beam intensity. Further tests should be performed to clarify this issue.

The multiplicity/fiber cross talk measurement should further be investigated as well. Specifically, the percentage of events where at least two fibers scintillated seems very high, taking into account the very low probability of simultaneous particles. In particular, during the muon run $\sim$2000 events were recorded per spill duration of $\sim$0.5 s. Assuming a homogeneous spill (a relatively valid assumption for low intensity runs, see Fig. 9.8), the probability that a particle will pass from the detector in a 100 ns time window is 0.4%. Assuming a Poisson distribution, the probability that two particles will reach the detector during the 100 ns time window is less than 0.02%, which cannot account for the observed multiplicity percentage of 6% .

The maximum buffer size of 3276 events/spill is not of course related to the XBPF performance and can be improved in the future. Nonetheless, taking into account the very low intensity of the VLE beamlines, this limitation will not be an issue.

The timestamp differences between the recorded trigger timestamp and the event timestamp, or those between the recorded trigger timestamps of both detectors have been linked to a high density of events, pointing towards a electronics and buffer problem. Similarly, this will not be an issue in the VLE beamlines due to the low data acquisition rate.

Finally, the impact of the fiber coating could not be conclusive due to the slightly asymmetric beam conditions. Such impact could be successfully tested by constructing two separate detectors, one with all fibers coated and the other with no treatment. A conclusive test could be performed, if the two planes are placed inside the same tank, and therefore the beam "seen" by the coated XBPF would be almost identical to the beam "seen" by the non-coated XBPF.

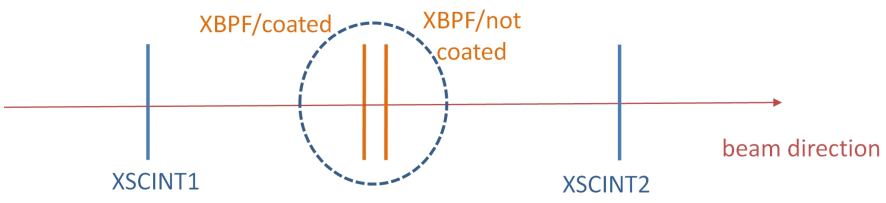

Figure 9.22: *Proposed setup for successfully measuring the effect of the aluminum coating on the fiber cross - talk.*

9.5 Time of Flight measurement

A ToF measurement was attempted over a distance of ∼13.5 m, using the modules XSCINT1 and XSCINT2. Since no coincidence is used to select the data, noise events are recorded as well which are non-negligible. In the independent analysis, all events in between the spills have been rejected. Therefore, for each event reaching XSCINT2 in the burst time interval, the event of XSCINT1 having the closest timestamp within 150 ns was chosen.

Table 9.1 shows the theoretically calculated time of flight for the different particle species over a 13.5 m distance from XSCINT1 to XSCINT2.

Calculated time of flight (ns)				
Momentum (GeV/c)	p	π	K	e
0.5	95.8	46.8	63.3	45.0
1	61.7	45.5	50.2	45.0
2	49.7	45.1	46.4	45.0
3	47.2	45.1	45.6	45.0

Table 9.1: *Time of flight for various particle species and momenta over a 13.5 m distance*

Fig. 9.23 shows the measured time of flight for a beam momentum of 0.5 GeV/c. The first peak corresponds to pions and possibly positrons, while the second one to protons. No kaons are expected to reach XSCINT2, taking into account its ∼47 m distance from the Multitarget, therefore no peak at around 63 ns is visible. The protons (second peak) are only a fraction of ∼6% of the composition.

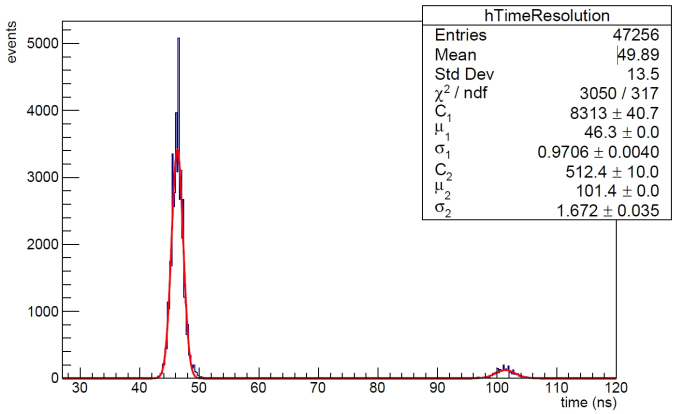

Figure 9.23: *Measured time of flight for a beam momentum of 0.5 GeV/c. The $\pi - e^+$ (left) and p (right) peaks are visible.*

By fitting a Gaussian distribution in both peaks, the time resolution can be determined by calculating the RMS. Specifically, for the pion-positron peak the time resolution is 0.97 ns, while for the proton peak it is 1.7 ns.

In Fig. 9.24 the results obtained for 1 GeV/c beam momentum are shown. Two peaks are visible, again corresponding to the pion-positron peak and the proton peak respec-

tively. As in the 0.5 GeV/c case, no kaons are expected to reach XSCINT2. The time resolutions in the 1 GeV/c beam momentum are 0.96 ns and 1.1 ns respectively.

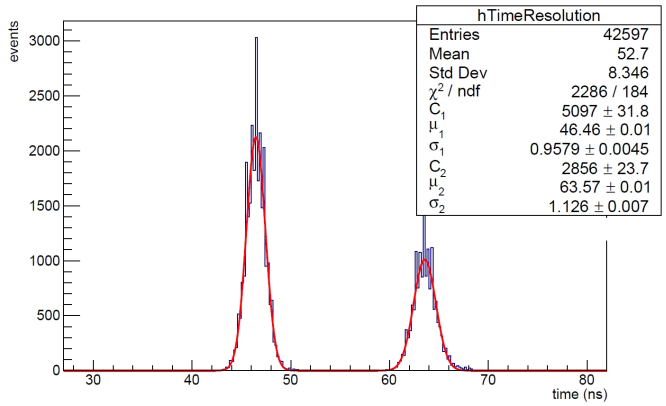

Figure 9.24: *Measured time of flight for a beam momentum of 1 GeV/c. The $\pi - e^+$ (left) and p (right) peaks are visible.*

The results for 2 GeV/c beam momentum are illustrated in Fig. 9.25. The two curves begin to overlap, but separation is still possible, although only at two sigmas. A fraction of $\sim$4% of the generated kaons are expected to reach XSCINT2, but, due to their very close time of flight compared to pions, any detected K contribute to the first peak. The mild peak visible at 63 ns has been assigned to deuterons.

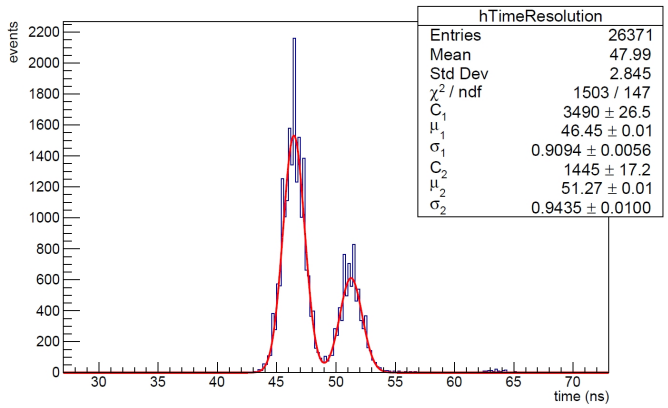

Figure 9.25: *Measured time of flight for a beam momentum of 2 GeV/c. The $\pi - e^+$ (and possibly K) as well as the p peaks are visible. The particles with an $\sim$63 ns are most likely deuterons.*

For 3 GeV/c beam momentum, the results are shown in Fig. 9.26. It is impossible to separate the different particle species, due to their very close time of flight (Table 9.1).

Table 9.2 summarizes the time resolution obtained in the various beam momenta.

The difference in the time resolution between the two peaks, as well as its dependence on the beam momentum can be explained by the inherent time of flight spread, due to the momentum dispersion of the T10 beam. The exact dp/p distribution of the

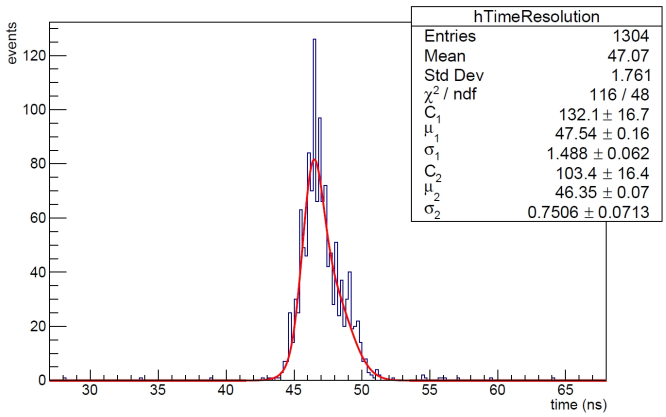

Figure 9.26: *Measured time of flight for a beam momentum of 3 GeV/c.*

Measured time resolution (ns)		
Momentum (GeV/c)	Peak 1	Peak 2
0.5	0.971 ±0.004	1.67 ±0.04
1	0.958 ±0.005	1.126 ±0.007
2	0.909 ±0.006	0.94 ±0.01

Table 9.2: *Measured time resolution for both peaks, for 0.5, 1 and 2 GeV/c beam momenta.*

T10 beam is unknown, but a normal distribution with a 2% spread is a good approximation.

The time of flight for a distribution of 10^5 p having 0.5 GeV/c has been calculated, assuming a 2% dp/p RMS, and has been compared with the corresponding π time of flight. The resulting time of flight distributions, to be compared with Fig. 9.23, are illustrated in Fig. 9.27.

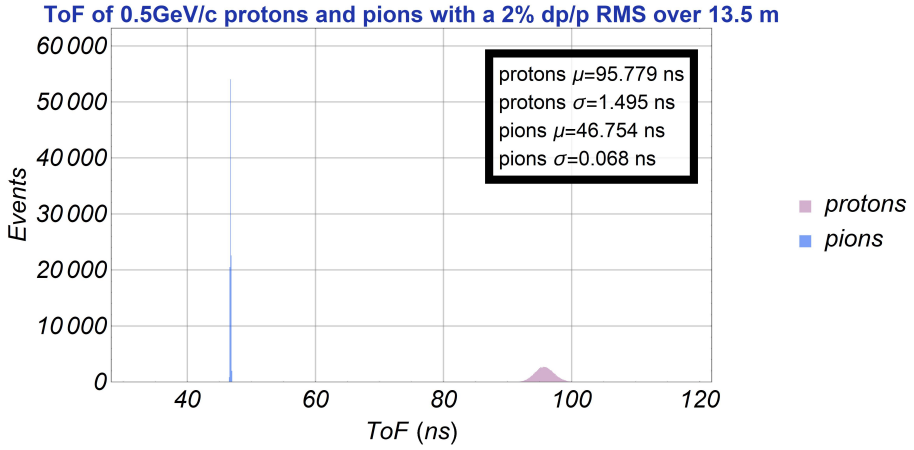

Figure 9.27: *Expected π and p time of flight distributions for a 0.5 GeV/c beam with 2% dp/p RMS.*

It can be seen that, due to the inevitable momentum dispersion an inherent time

of flight spread exists, not associated with the SciFi - TDC time resolution. This time spread is negligible for pions, but for protons, due to their considerable mass, it is of the same order of magnitude with the measured time resolution. Even if 1% dp/p RMS is assumed, which is an extremely optimistic case, the proton time spread is $\sigma_p = 0.75$ ns, while for 2 GeV/c $\pm$2%, the proton spread is reduced to only 0.2 ns.

For 1 GeV/c and 2% dp/p RMS, the same calculation yields $\sigma_p = 0.581$ ns and $\sigma_\pi = 0.017$ ns, as shown in Fig. 9.28, therefore the proton spread is still significant. Assuming a 1% dp/p momentum spread, the latter is reduced to 0.29 ns.

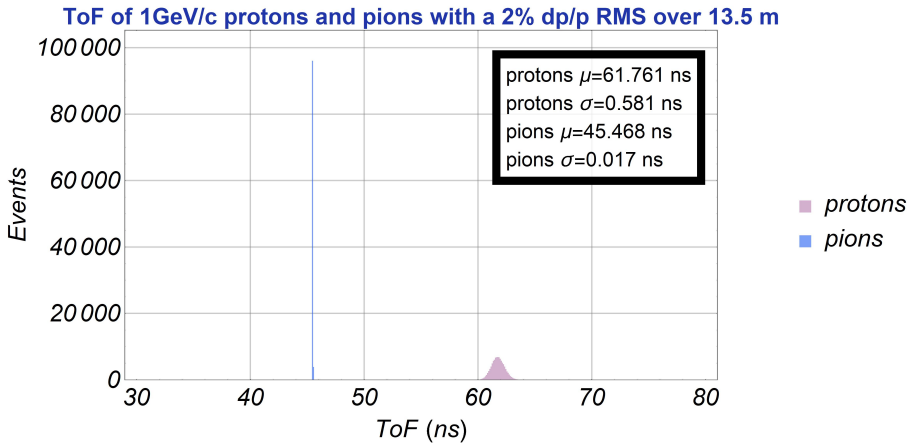

Figure 9.28: *Expected π and p time of flight distributions for a 1 GeV/c beam with 2% dp/p RMS.*

To conclude, since the exact momentum spread of the T10 beam is unknown, the time resolution should be determined in configurations where the inherent time spread is negligible, that is preferably for the pion peak and momenta above 1 GeV/c. It is therefore safe to deduce that the time resolution of the SciFi - TDC is below 1000ps, and for the 2 GeV/c π peak, where the inherent spread is minimum, it has been measured as $\sigma_t = 909 \pm 6$ ps.

This excellent time resolution can provide a precise ToF measurement in the VLE beamlines, over a distance of $\sim$32 m in H2-VLE, and $\sim$29 m in H4-VLE.

Figs. 9.29 and 9.30 show the theoretically expected π/p and K/p separations in H2-VLE for various time resolutions of the setup, neglecting any intrinsic spread due to dispersion. Assuming a time resolution of 900 ps, for momenta up to 3.5 GeV/c, pions can be separated from protons, while kaons from protons can be separated up to 3 GeV/c, both with a 4-sigma separation.

For very low energies of 1 GeV/c, the intrinsic spread in the proton time of flight due to a 5% dp/p RMS (expected in the VLE beamlines when the collimator is fully open) is large (3.5 ns) however due to the large time of flight difference compared to kaons and protons ($\sim$26 ns), it does not interfere with the separation of different species. For 3 GeV/c however, it is theoretically possible to separate K from p with exactly 4 sigmas, as shown in 9.30. The proton time of flight spread for 5% dp/p is 500ps, compromising

the separation certainty.

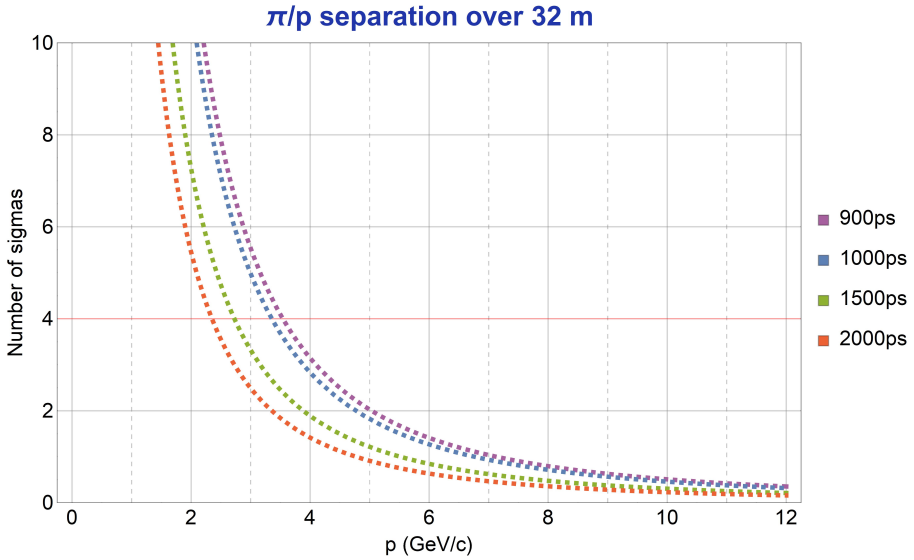

Figure 9.29: *Theoretical time of flight separation between π and p for H2-VLE, measured in number of sigmas.*

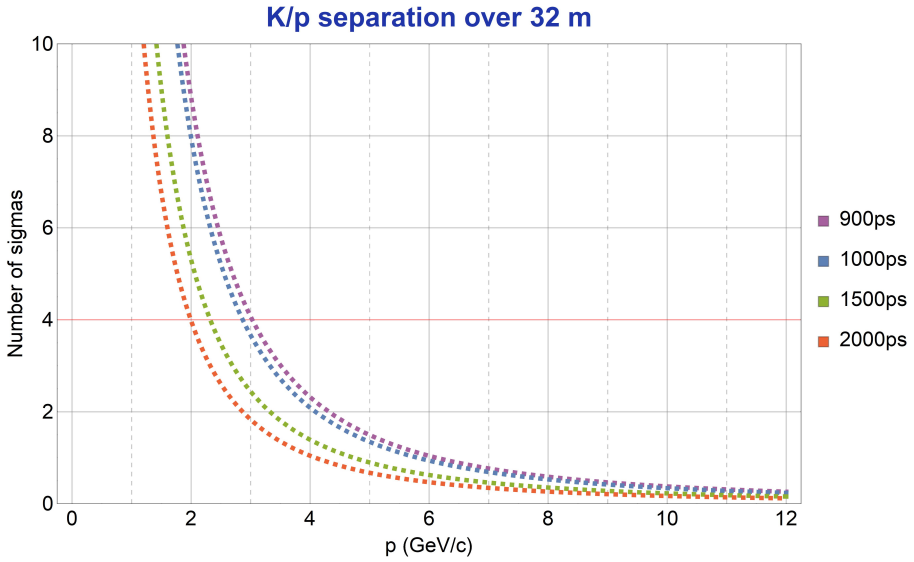

Figure 9.30: *Theoretical time of flight separation between K and p for H2-VLE, measured in number of sigmas.*

Appendices

APPENDIX A

Derivation of Hill's Equation

As explained in Chapter 1, to describe the motion of charged particles, we use the Frenet-Serret coordinate system, shown in Fig A.1 which follows the reference orbit.

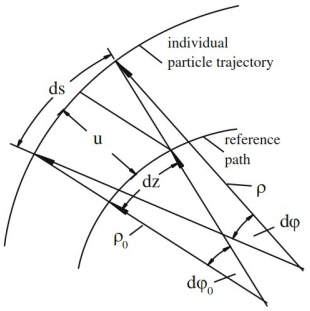

Figure A.1: *Frenet-Serret local reference system, following the central trajectory[13].*

This discussion will consider the horizontal plane, x, but a generalization for the vertical plane will then easily be derived. For an infinitesimal segment of a bending magnet, the deflection angle of the ideal path is $d\phi_0 = dz/\rho_0 \equiv \kappa_0 dz$. For an arbitrary particle the deflection angle is then given by $d\phi = ds/\rho \equiv \kappa ds$. In linear approximation, the path length element for an arbitrary particle is found geometrically

$$ds = (1 + \kappa_0 x)dz \tag{A.1}$$

In order to obtain the equation of motion with respect to the ideal path, we subtract from the arbitrary curvature κ, the reference curvature κ_0, $x'' = -(d\phi/dz - d\phi_0/dz)$

$$x'' = -(1 + \kappa_0 x)\kappa + \kappa_0 \tag{A.2}$$

For the horizontal plane, the curvature κ_x can be expressed, up to second order, by its components:

$$\kappa_x = \frac{1}{1+\delta}(\kappa_0 x + kx + \frac{1}{2}mx^2) \tag{A.3}$$

where δ is the momentum offset, $p = p_0(1 + \delta)$, and all terms κ_0, k, m are momentum

independent, and a function of the independent coordinate z. Combining (A.2) and (A.3) yields:

$$x'' + (k + \kappa_{0x}^2)x = \kappa_{0x}(\delta - \delta^2) + (k + \kappa_{0x}^2)x\delta - \frac{1}{2}mx^2 - \kappa_{0x}kx^2 \tag{A.4}$$

where we have included terms up to second order, where the terms:

- kx describes the focusing effect of a quadrupole magnet
- κ_{0x}^2 the focusing of a sector bending magnet, that is purely geometrical in nature
- $\kappa_{0x}(\delta - \delta^2)$ the deflection offset for particles with momentum different from the design
- $(k + \kappa_{0x}^2)x\delta$ results in chromatic aberrations
- $\kappa_{0x}kx^2$ is included only if there is both focusing and bending present in the same magnetic element
- $\frac{1}{2}mx^2$ is the sextupole term

Similarly, in the vertical plane, where we can assume immediately for simplicity that we have no bending in the vertical plane, therefore $\kappa_{0y} = 0$.

$$y'' - ky = -ky\delta - +mxy \tag{A.5}$$

In real transport systems, extra care is given to establish magnetic fields with almost ideal properties, so terms such as m do not exist in dipoles and quadrupoles, but only in sextupoles. Furthermore, usually the momentum offsets are quite small- typically less than 5%. In this formulation, all the terms in the right-hand side of (A.4) can be treated as small perturbations.

Moving on to solve the homogenous part of (A.4), we arrive to Hill's Equation (A.5):

$$u''(s) + K(s)\,u(s) = 0 \tag{A.6}$$

where u stands for either x or y, and$K = k + \kappa_x^2$ for the horizontal or $K = -k$ for the vertical plane.

Suppressing higher multipole terms in dipoles and quadrupoles is therefore very important.

APPENDIX B

Spot sizes with respect to the floor of EHN1

Spot sizes at BPROF4 and NP-02 middle for H2-VLE, 12 GeV/c with respect to EHN1 floor			
	v0 Optics	High Transmission Optics	High Resolution Optics
	BPROF4 profile		
μ_x (mm)	1.05	0.33	-0.41
σ_x (mm)	31.51	32.29	29.70
μ_y (mm)	2.43	1.91	1.10
σ_y (mm)	24.97	25.73	23.30
	NP-02 middle profile		
μ_x (mm)	0.35	0.78	0.38
σ_x (mm)	19.42	22.55	17.23
μ_y (mm)	1.77	1.55	1.50
σ_y (mm)	17.93	21.23	15.43

Spot sizes at BPROF4 and NP-04 entrance for H4-VLE, 7 GeV/c with respect to EHN1 floor			
	v0 Optics	High Transmission Optics	High Resolution Optics
	BPROF4 profile		
μ_x (mm)	5.41	4.50	-3.79
σ_x (mm)	31.90	26.15	28.86
μ_y (mm)	-0.79	-1.03	-0.63
σ_y (mm)	31.14	21.71	16.69
	NP-04 entrance profile		
μ_x (mm)	6.59	5.45	-4.35
σ_x (mm)	31.96	28.11	29.79
μ_y (mm)	-1.81	-1.87	-0.80
σ_y (mm)	31.30	24.97	17.12

Bibliography

[1] CERN Document Server, OPEN-PHO-ACCEL-2016-009

[2] G. Brianti,*SPS North Experimental Area – General Layout*, CERN/LAB II/EA/Note 73-4, 1973

[3] R. Acciarri *et al.* (DUNE Collaboration), *Long-Baseline Neutrino Facility (LBNF) and Deep Underground Neutrino Experiment (DUNE)*- Conceptual Design Report, Volume 1, arXiv:1601.05471v1, 20 Jan 2016

[4] C. Rubbia, *The Liquid-Argon Time Projection Chamber: A new concept for Neutrino Detectors*, EP Internal Report 77-8

[5] The ICARUS collaboration (M. Antonelo et.al.), *Precision Measurement of the Neutrino Velocity with the ICARUS detector in the CNGS beam*, JHEP11 (2011) 049

[6] The DUNE Collaboration, *The Single-Phase ProtoDUNE, Technical Design Report*, arXiv:1706.07081v2 [physics.ins-det] 27 Jul 2017

[7] G. Balik *et al.* (The WA105 Collaboration), *Progress report on LBNO-DEMO/WA105*, CERN-SPSC-2015-013/SPSC-SR-158

[8] A. Rubbia *et al.* (DUNE Collaboration), Report No. CERN-SPSC-2014-013.

[9] T. Kutter *et al.* (DUNE Collaboration), Report No. CERNSPSC-2015-020.

[10] N. Charitonidis, I. Efthymiopoulos, *Low energy tertiary beam line design for the CERN neutrino platform project*, Physical Review Accelerators and Beams 20, 111001 (2017)

[11] N. Charitonidis, Y. Karyotakis, I. Efthymiopoulos, *Beam performance and instrumentation studies for the ProtoDUNE-DP experiment of CENF*, CERN-ACC-NOTE-2016-0052

[12] L. Gautignon, *Magnets Kit*, CERN-OPEN-2004-003

[13] H. Wiedemann, *Particle Accelerator Physics, 4th ed.*, Springer.

[14] K.Brown, *A First-and Second-Order Matrix Theory for the Design of Beam Transport Systems and Charged Particle Spectrometers*, SLAC-75.

[15] B. de Raad, A. Minten, E. Keil *Lectures on beam optics*, CERN Academic Training Lecture, CERN 66-21.

[16] C. Brown, F.Rothacker, Ch.Iselin, *TRANSPORT: A Computer Program for Designing Charged Particle Beam Trasnport Systems*.

[17] H. Goldstein, *Classical Mechanics*, Addison-Wesley, Reading (1980)

[18] J. Rees, *Symplecticity in Beam Dynamics: An Introduction*, SLAC-PUB-9939

[19] H. Grote, F. Schmidt, L. Deniau, G. Roy *The MAD-X Program (Methodical Accelerator Design*, Version 5.03.07

[20] B. Holtzer, *Introduction to Transverse Beam Dynamics*, CERN-2014-005.

[21] M. Reiser, *Theory and Design of Charged Particle Beams*, WILEY-VCH

[22] P. Coet, N. Doble, S. Reucroft, *Beam Possibilities for the European Hybrid Spectrometer*, European Hybrid Spectrometer Workshop on Holography and High-Resolution Techniques, 1982

[23] N. Charitonidis, M. Rosenthal, Private Communication, 2017

[24] T. Zickler et al., Private Communication, 2017

[25] D. Carey, K. Brown, Ch. Isein, *Decay TURTLE (Trace Unlimited Rays Through Lumped Elements)*, SLAC-246

[26] E. Forrest, F. Schmidt, E. McIntosh, *Introduction to the Polymorphic Tracking Code*

[27] T. Roberts et al, *G4BeamLine Simulation Program for Matter Dominated Beamlines*, Proceedings of PAC07, Albuquerque, New Mexico, USA, ref: THPAN103

[28] Aboubakr Ebn Rahmoun, Private Communication, 2017

[29] J. Spanggaard, *Delay wire chambers: a users guide*, SL-Note-98-023 (BI)

[30] I. Ortega, A. Bay, G. Haefeli, J. Spanggaard, G. Tranquille, *A scintillating fibre beam profile monitor for the experimental areas of the SPS at CERN*

[31] I. Ortega Ruiz, *Accurate Profile Measurement of the low Intensity Secondary Beams in the CERN Experimental Areas*, EPFL Thesis No. 8278 (2018)

[32] G. Knoll, *Radiation Detection and Measurement*, John Willey & Sons, Inc.

[33] Hamamatsu Photomultiplier tube, model H11934, https://www.hamamatsu.com/resources/pdf/etd/R11265U_H11934_TPMH1336E.pdf.

[34] B. Aull, H. Loomis et al., *Geiger-Mode Avalanche Photodiodes for Three- Dimensional Imaging*, Lincoln Laboratory Journal, Vol. 13, No.2, 2002

[35] S. Piatek, *A technical guide to silicon photomultipliers (SiPM)*, Hamamatsu Corporation & New Jersey Institute of Technology. URL: https://www.hamamatsu.com/us/en/community/optical_sensors/articles/technical_guide_to_silicon_photomultipliers_sipm/index.html

[36] East Area Layout 2014, URL: http://sba.web.cern.ch/sba/BeamsAndAreas/East/EALayout2014-final.pdf

[37] J. Fleury, S. Callier et al., *Petiroc and citiroc: front-end asics for sipm read-out and tof applications*, J. Instrum., 9, 2014